Title
Fundamental Study on Nanoparticle Incorporation, Dispersion, and Effects in Fe-based Nanocomposites

Author
Zheng, Shiqi

Publication Date
2021

Peer reviewed|Thesis/dissertation

UNIVERSITY OF CALIFORNIA

LOS ANGELES

Fundamental Study on Nanoparticle Incorporation, Dispersion, and Effects in Fe-based Nanocomposites

A dissertation submitted in partial satisfaction of the requirements for the

Degree of Philosophy in Materials Science and Engineering

by

Shiqi Zheng

2021

ABSTRACT OF THE DISSERTATION

Fundamental Study on Nanoparticle Incorporation, Dispersion, and Effects in Fe-based Nanocomposites

by

Shiqi Zheng

Doctor of Philosophy in Materials Science and Engineering

University of California, Los Angeles, 2021

Professor Xiaochun Li, Chair

Steels and other iron-based alloys hold great importance in human society, because they are abundant, cost-effective, and have versatile properties, which can be used to fulfill a wide range of roles. As such, increasing the performance and properties of steels is of both technological and commercial interest. Fe-based nanocomposites are often not economically viable due to the high production cost and low production volume, since they are mostly manufactured in solid-state processes that circumvent the reaction issue between liquid steel and its reinforcing phase. To enable a wide application for Fe-based nanocomposites, cost-effective liquid metallurgy processes

need to be developed, as liquid metallurgy is the most widely adopted and cost-effective method of manufacture metals and alloys at scale.

The overall goal of this work is to study the nanoparticle incorporation, dispersion, and effects in Fe-based nanocomposites by economical processes, especially liquid metallurgy. First, Invar 36 (Fe36Ni) alloy was reinforced by WC nanoparticles. The reactivity in Invar-WC system was suppressed by temperature control method. It was found that only when the processing temperature was significantly below the melting point of Invar, the reactivity can be reasonably managed. However, the Invar-WC nanocomposite had high strength and favorable thermal expansion properties. Second, TiB_2 reinforced Fe-Ti-B high modulus steel (HMS) was studied. The dissolution of TiB_2 in liquid Fe was suppressed by the combination of solute (elemental Ti and B) saturation and TiB_2 nanoparticle addition (nano-treating). When adding TiB_2 nanoparticles into a melt that is already saturated in dissolved Ti and B, the dissolution of TiB_2 nanoparticles was reduced. The nano-treating process gave rise to an unexpected solidification phenomenon. The nano-treated HMS had significant higher strength and similar ductility comparing with conventional HMS. Finally, theoretical modeling was conducted to examine the interactions between liquid Fe alloys and oxides for a stable dispersion of oxide nanoparticles. Experiments were conducted to validate the theoretical predictions.

The dissertation of Shiqi Zheng is approved.

Jenn-ming Yang

Jaime Marian

Lihua Jin

Xiaochun Li, Committee Chair

University of California, Los Angeles

2021

To my parents for their love and support.

Table of Contents

Acknowledgements

There is a great beauty in metals; it calls to me. I am glad that I answered the call and embarked on an arduous Ph.D. journey devoted to study metals. Looking back, the four years of my Ph.D. journey was often filled with challenge and hardship, sometimes even confusion. But I have no regrets.

I want to express my gratitude to my Ph.D. supervisor Professor Xiaochun Li, for his guidance and support throughout my study. Prof. Li is a scientist with many wonderous ideas. It is fortunate of me to have him as my supervisor.

I am thankful to my Ph.D. committee members: Prof. Jenn-ming Yang, Prof. Jaime Marian, and Prof. Lihua Jin, for their insights and critical evaluation of my research works.

I want to thank my colleagues in this research group, in particular, Jie Yuan, Nar Murali, and Tianqi Zheng, for their assistance in different aspects of my research work. I wish them good fortune in their own research and Ph.D. journey.

Lastly, I want to thank my family members. My parents provided me with a stable family when I was growing up and resources that enabled me to pursue science. My grandfather is a loving man and a skillful engineer. He inspired my father to become a professional engineer, and myself to become a Ph.D. in the field of materials science and engineering. For this, I will always be grateful.

Vita

2014, B.S., Materials Science and Engineering, University of Illinois at Urbana-Champaign, USA

2016, M.S., Materials Science and Engineering , McMaster University, Canada

Publications

- S. Zheng, J. Vanderstelt, J.R. McDermid, J.R. Kish, “Non-destructive investigation of aluminum alloy hemmed joints using neutron radiography and X-ray computed tomography”, NDT & E International, 91 (2017), 32-35
- S. Zheng, M. Sokoluk, G. Yao, I.D. Rosa, X. Li, “Fe–Ni Invar alloy reinforced by WC nanoparticles with high strength and low thermal expansion”, SN Applied Sciences (2019) 1:172
- X. Xie, Y. Deng, J. Peng, S. Zheng, C. Cao, W. Xie, X. Li. “Nanoparticle‐Reinforced Silica Gels with Enhanced Mechanical Properties and Excellent pH‐Sensing Performance”, Particle and Particle Systems Characterization (2020), 1900404
- M. Zuo, M. sokoluk, C. Cao, J. Yuan, S. Zheng, X. Li, “Microstructure Control and Performance Evolution of Aluminum Alloy 7075 by Nano-Treating”, Scientific Reports (2019) 9:10671

Chapter 1. Introduction

1.1. Research motivation

1.1.1. Historical background of steel-based composites

Iron and its alloys, most commonly, steels, have been one of the cornerstones of human civilization. Upon the discovery of iron ore smelting and, subsequently, steel making, the usage of steel in weaponry and armour quickly eclipsed that of bronze owing to the vastly superior mechanical properties of steels when properly formed and heat treated [1]. Since industrial age, steel became a vital monolithic structural material in architecture and transportation sectors due to its combination of strength and ductility, which can be controlled over a wide range by alloying and heat treatment [2].

The widespread usage of iron and steel throughout history is the driving force of the continuous pursue over better mechanical properties. In cases when the requirement of mechanical properties cannot be fulfilled by steels of a singular composition, the need for steel-based composites rises.

The earliest steel-based composite material was created by a process of forge welding steels rods or plates of different compositions, primarily of varying carbon concentrations due to the lack of precise control over other alloying elements. The resulting product is often functionally superior and aesthetically pleasing, commonly referred to as Damascus steel, owing to the alternating pattern created by different composition of steel resembling that of a damask, a type of woven fabric with ornate pattern. Damascus steel embodies the concept of composite material in which the overall property of an ideal composite material is the favourable combination of the properties of its constituent materials. For example, ancient swordsmith would encase a steel with very low carbon content within a steel with high carbon content, the resulting Damascus steel when used to

construct cutting weapons will exhibit excellent cutting ability due to the high hardness of high carbon steel of the outer layer whilst retaining the ductility and fracture toughness due to the soft low carbon steel of the inner layer, as illustrated in Figure 1.1[1]–[4].

In the past few decades, ceramic particles became the choice of material for reinforcing metals, the resulting composite is commonly known as metal matrix composites (MMCs). Comparing to the historical steel composites, the modern steel composites offer a wider range of properties due to large dissimilarity between ceramic reinforcing phase and the steel matrix. Consequently, a large body of scholarly work has been invested into steel-based MMCs. The reinforcing ceramic particles in steel-based MMCs are typically carbides, e.g. TiC, NbC, nitrides, e.g. AlN, TiN, borides, e.g. TiB_2, and oxides, e.g. Y_2O_3, Al_2O_3, ZrO_2 [5].

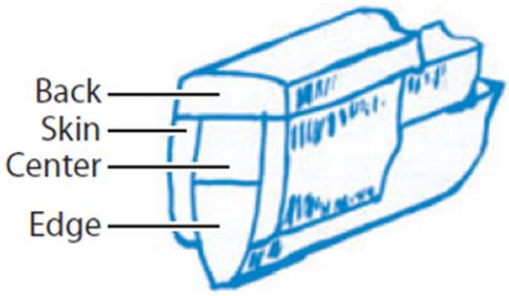

Figure 1.1: Schematic of the cross-section of a blade utilizing different composition of steels in its construction [2].

Although MMCs can offer improved mechanical properties with respect to the unreinforced alloys, they are typically limited by the severe loss of ductility and fracture toughness due to the presence of brittle ceramic phase in the micron length scale, which, in turn, can overshadow the gain of strength and hinder the engineering application of MMCs [6].

1.1.2. Metal matrix nanocomposites (MMNCs) and challenges

Metal matrix nanocomposites (MMNCs) share similarities with traditional MMCs due their utilization of hard ceramic particles as the reinforcing phase. While the traditional MMCs are typically reinforced by micro-sized ceramic particles, MMNCs emphasize the reinforcement by nano-sized ceramic particles. In comparison with micro-sized ceramic particles, nano-sized ceramic particles further improve the strength and hardness of the metal matrix, while largely reduce the embrittlement effect. For this reason, the research into MMNCs gained significant popularities in recent years [6], [7].

The manufacturing of MMNCs can be divided into two main categories: *ex situ*, in which the reinforcing ceramic nanoparticles are directly added into powdered or molten metal matrix, and *in situ*, in which the reinforcing ceramic nanoparticles are generated in the metal matrix (solid or molten) by chemical reactions between the constituent alloying elements [6], [7]. Both manufacturing methods have been successfully demonstrated in various metal matrix, e.g., Mg, Al, Cu, Fe, etc.

The *in situ* manufacturing of MMNCs faces the dilemma between achieving strong mechanical properties and reducing the manufacturing cost. When *in situ* reaction occurs in molten metal, the reaction product, such as nitrides, borides, and carbides, tends to form continuously until reaching a stable size, ranging between around 1 μm to tens of microns. As such, in order to preserve the nano-sized features and the benefits, it is of importance that the *in situ* reaction is terminated when the reaction product is still small sized (<100 nm), by rapidly removing the primary driving force for the reaction---temperature. While rapid solidification (or rapid cooling) is readily achievable in an experimental and small-scale setting, it becomes significantly more costly in large-scale production, such as in an industrial setting [8], [9]. On the other hand, when

in situ reaction occurs in solid metal, the reaction product is naturally small, due to the lack of driving force for them to continuously grow. However, the lack of reaction driving force also means that the reaction itself can only occur at extremely low rate, typically during ball milling over the course of hours or even days. As a result, the MMNCs manufactured by solid state *in situ* reaction are mostly commonly in powder form and in limited quantity due to the restriction of the reaction condition. This also significantly increases the cost of the MMNCs similar to the combination of liquid state *in situ* reaction and rapid solidification. In either case, the MMNCs become cost prohibitive for large-scale application.

The *ex situ* manufacturing of MMNCs encounters the challenge between achieving uniform dispersion of nanoparticles in the matrix and preventing their reaction. In molten metals, the uniform dispersion of nanoparticles hinges upon the delicate energy balance between the van der Waals (vdW) attraction potential of nanoparticles, which causes the nanoparticles to agglomerate, and the energy barrier by wetting in the molten metal, which seeks to prevent the nanoparticles from touching through a thin liquid film, meanwhile the balance of these two potentials must simultaneously combat the random thermal motion of the nanoparticles, which causes the nanoparticles to collide occasionally [10]. As such, it is of importance that the selected nanoparticles should have a low vdW between them in molten steels to enable nanoparticle dispersion and a good wettability (low wetting angle, θ) with the molten metal matrix to mitigate sintering. However, excellent wetting between the nanoparticles and the molten metal often entails the chemical reaction between the two, called reactive wetting [11]. In solid metals, the uniform dispersion of nanoparticles can be achieved through rigorous mechanical alloying processes which bypass the tradeoff between wettability and reactivity due to the low temperature. However, this method faces the similar issue as the solid state *in situ* reaction route, due to the long processing

time and low volume of production, which makes the MMNCs cost prohibitive for large-scale application.

1.1.3. Fe-based MMNCs and challenges

Compared to Al, Mg, or Zn-based MMNCs, there are less development in the space of Fe-based MMNCs. In order to satisfy the large societal demand for steels, steels are developed and produced with very thin price margin and is sensitive to the additional cost of any new steel product. As such, the development of Fe-based MMNCs is often hindered by the stringent cost requirement and reserved to several niche areas that the high cost could be justified.

In Fe-based MMNCs, the reinforcement phase can be carbides (such as TiC), borides (such as CrB_2, TiB_2) and oxides (such as Y_2O_3), while the Fe matrix can have different composition, ranging from lean systems like carbon steel to alloy rich systems like stainless steel [8], [12]–[14].

The manufacturing of Fe-based MMNCs inherits the difficulties mentioned in section 1.1.2. , albeit exacerbated further by the high temperature involved in the steel-making process. Due to the high melting point (1450 – 1540 °C), molten steel exhibit strong reactivity with carbides, borides, and nitrides, and large solubility with other metallic elements. As such, the *ex situ* addition of nanoparticles into molten steel will result in the reaction or dissolution of the majority of these nanoparticles, making the process unfeasible. While the formation of these nanoparticles through liquid state *in situ* reaction is possible, very high solidification rate is necessary to control their size.

Noticeably, oxides particles, such as Y_2O_3, Al_2O_3, MgO, etc., are more stable in molten steel, comparing to their carbide, boride, and nitride counterparts, owing to the inherent high thermodynamic stability of metal oxides. Therefore, strengthening Fe matrix using stable oxide particles has garnered significant research interest in the past decades, especially in the field of

nuclear material, where the material cost can be justified due to the hazardous and demanding environment [15]. The Fe-based MMNCs using oxides as the reinforcing phase is known as oxide-dispersion strengthened steel (ODS steel). However, the high stability of oxides also brings about its poor wettability with molten steels, which prevents ODS steel being manufactured in a conventional liquid metallurgy setting. Instead, the costly solid state processing route must be employed to make ODS steel, hence hindering its application aside from in the most demanding environment due to cost concerns. Therefore, the development of cost efficient manufacturing method for ODS steel and other types of Fe-based MMNCs has the potential to propel their application into the broader consumer market.

1.2. **Research Objectives**

This research seeks to develop novel manufacturing methods for Fe-based MMNCs with an overall emphasis on using liquid metallurgy. In detail, the objectives of this research include:

1. Investigating the incorporation and dispersion of WC nanoparticles in Fe-Ni (Invar 36) matrix, and their effect on mechanical and thermal properties.
2. Investigating the effect of TiB_2 nanoparticles on the solidification behavior of a Fe-Ti-B high modulus steel melt, specifically, on the fundamental mechanisms of the changes in the solidification behavior. This investigation also studies the mechanical properties of the nanoparticle-enabled Fe-Ti-B high modulus steel product.
3. Using theoretical and experimental approach to identify the alloying element, such as Nb, Si, and Cr, that enable the oxide nanoparticle dispersion in molten steel.
4. Investigating the use of liquid metallurgy to incorporate oxide nanoparticles into steel matrix in scalable methods, a task that is not previously demonstrated in literature.

Specifically, the influence of different alloying elements, such as Nb and Cr, on the dispersion of oxide nanoparticles, microstructures and properties is studied.

1.3. **Work Summary**

This dissertation will be organized, from Chapter 2 onwards, as follows:

- Chapter 2 is the literature review on the highly relevant work of Fe-based MMNCs, including their manufacturing and effect of nanoparticles, etc.
- Chapter 3 presents the effect of WC nanoparticles on the mechanical properties and thermal expansion of the Fe-Ni (Invar 36) matrix.
- Chapter 4 investigates the effect of TiB2 nanoparticles on the solidification behavior of a Fe-Ti-B high modulus steel melt, including the detailed study on the microstructure, mechanical properties, solidification theory, and CALPHAD simulations.
- Chapter 5 presents the theoretical study on alloying element effect on oxide nanoparticle dispersion in molten steels and the experimental results of incorporation of oxide nanoparticles into some of the identified systems.
- Chapter 6 presents the experimental results on scalable manufacturing of ODS steel via liquid metallurgy, including studies on microstructure, mechanical properties, and the dispersion mechanism.
- Chapter 7 draws conclusions.
- Chapter 8 recommends areas of interest for future exploration.

Chapter 2. Literature review

2.1. The effects of nanoparticles in MMNCs

2.1.1. The general effects of nanoparticles

The addition of nanoparticles into a metal matrix gives rises to a multitude changes to the matrix, including changes on mechanical properties, solidification behaviour, microstructure, and potentially other functional properties. Some of the general effects of nanoparticles in MMNCs are expected to be applicable in Fe-based MMNCs. Therefore, this section of the literature review will focus on these general effects.

2.1.1.1. Effects of nanoparticles on mechanical strength

In many alloy systems, such as aluminum alloy 6000 and 7000 series, the aging heat treatment can be utilized to generate fine intermetallic precipitates in the matrix, through the manipulation of the change of solubility of certain alloying elements in the matrix at different temperatures. These fine intermetallic precipitates will drastically increase the material's mechanical strength through various mechanisms. The addition of hard ceramic nanoparticles into a metal matrix shares similarities to this situation. Relevant strengthening effect of nanoparticles in MMNCs include: Orowan strengthening, load transfer effect, coefficient of thermal expansion (CTE) mismatch strengthening, elastic modulus (EM) mismatch strengthening.

1) Orowan strengthening

When a moving dislocation encounters a small obstacle, it can either move pass the obstacle by shearing through it or by bowing around the obstacle and leaving a closed loop behind. These two interactions between dislocation and obstacle are known as Friedel cutting, which typically happens when the obstacle is small and coherent, with the matrix and Orowan looping, which

happens when the obstacle is large and incoherent with the matrix [16]. In the case of intermetallic precipitates serving as dislocation obstacles in regular alloys, the mechanism could be Friedel cutting, Orowan looping, or a mixture of both, depending on the size and coherency of the precipitate. In the case of MMNCs, the ceramic nanoparticles around 20 to 200 nm are the obstacles for dislocation. These nanoparticles are typically incoherent with the matrix and too strong to be sheared by the dislocations. As such, Orowan looping becomes the dominant interaction between dislocations and the nanoparticles in MMNCs. The strengthening effect cause by the Orowan looping is given by Eqn. 1 [7].

$$\Delta\sigma_{OR} = \frac{0.13bG}{d_p\left(\frac{1}{2V_p}^{1/3} - 1\right)} \ln\left(\frac{d_p}{2b}\right) \qquad \text{Eqn. 1}$$

where b is the Burger's vector, G is the shear modulus of the matrix, d_p is the particle diameter, and V_p is the uniformly dispersed particle volume fraction.

Observing Eqn. 1, it can be seen that particle diameter, d_p, and particle volume fraction, V_p, are the controlling factors for the Orowan strengthening mechanism. Smaller particle size and higher volume fraction will result in higher strengthening effect. Using the shear modulus, 78 GPa, and Burger's vector, 0.25 nm, of BCC-Fe, the theoretical Orowan strengthening effect of nanoparticles at varying sizes and volume fractions is shown in Figure 2.1. The Orowan strengthening effect drastically drops off as the particle size increases.

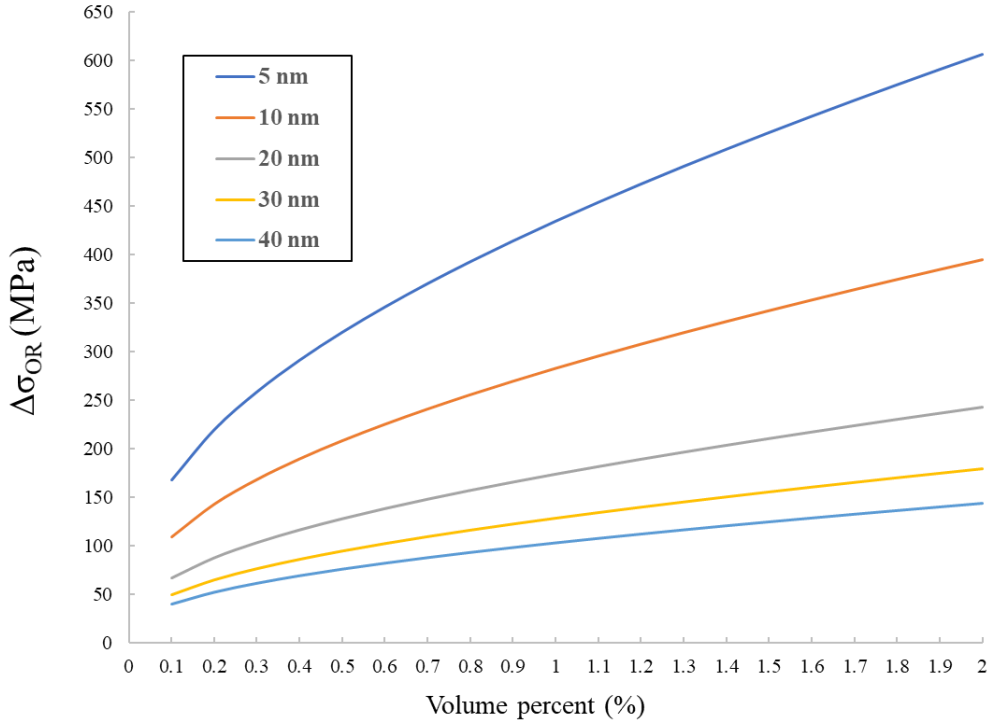

Figure 2.1: Theoretical Orowan strengthening effect of nanoparticles in Fe matrix.

2) Load-bearing effect

Comparing with the metal matrix, the reinforcing nanoparticles typically have significantly higher hardness and can carry more load. The strengthening effect due to the load transfer from metal matrix to the reinforcing nanoparticles is called load-bearing effect, and is given by Eqn. 2 [10].

$$\Delta\sigma_{LT} = 1.5 v_p \sigma_i \qquad \text{Eqn. 2}$$

where v_p is the volume fraction of the particles, σ_i is the interfacial bonding strength between nanoparticle and matrix.

In MMNCs, the volume fraction of nanoparticles is relatively low, typically about 1–5% [17]. If a moderate volume fraction of 2% and a bonding strength of 1250 MPa is considered, the

resulting load-bearing effect will be 37.5 MPa, which is a smaller enhancement comparing to the effect of Orowan strengthening under the same condition.

3) CTE mismatch and EM mismatch strengthening

The mismatch in CTE and EM between the nanoparticles and the metal matrix gives rise to the formation of geometrically necessary dislocations (GNDs) in order to accommodate the strain along the particle-matrix interface during temperature change and deformation. The relation between the strengthening effect and GND density due to CTE mismatch, ρ^{CTE}, and EM mismatch, ρ^{EM}, is given by Eqn. 3 to Eqn. 5 [7], [18].

$$\Delta\sigma_{CTE+EM} = \sqrt{3}\beta Gb\,(\sqrt{\rho^{CTE}} + \sqrt{\rho^{EM}}) \quad \text{Eqn. 3}$$

$$\rho^{CTE} = \frac{A\Delta\alpha\Delta T V_p}{b d_p (1 - V_p)} \quad \text{Eqn. 4}$$

$$\rho^{EM} = \frac{6V_p}{\pi d_P^3}\varepsilon \quad \text{Eqn. 5}$$

where A is a geometric constant, $\Delta\alpha$ is the difference in CTE, ΔT is the difference in testing and processing temperature, ε is the macroscopic deformation strain caused by work-hardening.

It is worth noting that both of these strengthening effects are very prominent in conventional MMCs, where high volume fraction of micro-sized reinforcing phase is present, that allows the formation of GNDs on the interface. In MMNCs, while these effects are still present, they are significantly less prominent, due to the low volume fraction and small particles size [7], [17].

2.1.1.2. Effects of nanoparticles on ductility

In conventional metallic alloys, the attainment of strength is often at the expense of losing ductility, such as in artificially aged aluminum alloys or quenched steels, where the materials become stronger but more brittle than in their state prior to heat treatment. This phenomenon is commonly

referred to as the strength–ductility trade-off [19], [20]. This trade-off is also generally maintained in MMNCs.

Stress concentration is an important factor influencing the development of cracks, which eventually leads to fracture, in metal matrix. A solid solution alloy, that has almost no precipitates, often exhibit much higher ductility than its precipitation strengthened counterpart, due to the homogenous microstructure that has low stress concentration. The reinforcing nanoparticles, due to being mostly ceramics, tend to have sharp corners and edges, which give rise to areas with high stress concentration, which, in turn, can cause the early development of cracks, hence reducing the ductility [21].However, due to the small size of nanoparticles, this effect is much less pronounced in MMNCs comparing to MMCs.

During plastic deformation, larger ductility is often found in situations where the hard phase (reinforcing phase) can be deformed along with the soft phase (matrix). This process is known as co-deformation. When the hard phase cannot be deformed along with the soft phase, it is called mechanical incompatibility, which typically leads to lower ductility [22]. In MMNCs, the reinforcing nanoparticles are typically significantly harder than the matrix and can not be plastically deformed. This discrepancy of the deformation between the nanoparticles and the matrix leads to high strain gradients in localized zones, while the macroscopic strain of the entire material is still low [23]. The strain gradients can be further aggravated over a large range by the presence of particle clusters, as illustrated in Figure 2.2 [21]. The particle clusters have higher particle volume fraction (V_2) than the nominal particle volume fraction of the matrix (V_1), and therefore possess higher local strength and lower local ductility.

The manufacturing process of MMNCs could introduce additional defects associated with nanoparticles, e.g. porosity, salt entrapment, weak interfacial bonding, impurity, etc. These defects

contribute to the loss of ductility in metal matrix. It is worth mentioning that as the nanoparticle size becomes smaller, and the distribution more uniform, the ductility of metal matrix becomes analogous to that of traditional precipitation hardened alloys. For this reason, the general design philosophy for improving the MMNCs ductility is to reduce the particle size and better particle dispersion, while suppressing the defects due to production process [24].

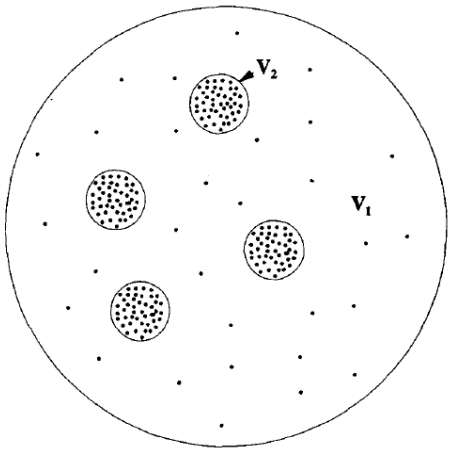

Figure 2.2: Schematic of a clustered particle structure represented by regions of high volume fraction (V_2) and a cluster-free region represented by low volume fraction (V_1) [21].

Special cases of the beneficial effect of nanoparticle on ductility

While the ductility loss is commonly expected and widely documented in MMCs and MMNCs, there are special cases where the addition of nanoparticles results in ductility gain of the material. This happens when the addition of nanoparticles can overcome certain brittle mechanism that is intrinsic to the metal matrix itself.

In molybdenum (Mo) alloys and some other bcc alloys, the ductility is typically limited due to the unavoidable impurity solutes, such as O and N, segregated at grain boundaries and the high ductile to brittle transition temperature (DBTT), which makes the alloy brittle even at room

temperature. Uniformly distributed intragranular rare earth oxides (La_2O_3) nanoparticles are shown to have significant beneficial effect on the ductility of Mo alloys. The commercially pure Mo alloy has a UTS of 534 MPa and elongation to failure of 13%. Comparatively, Mo alloy containing 0.6 wt.% La_2O_3 has much higher UTS of 865 MPa and elongation of 37.5%. This is attributed to the strong rare-earth–oxygen interactions, in which the La_2O_3 was able to gather detrimental impurity solutes (O and N) from the lattice. Additionally, the uniformly distributed intragranular La_2O_3 was shown to pin down and accumulate dislocations inside the grain, hence promoting more deformation before failure [25].

In Mg alloys and some other hcp alloys, their low symmetry and limited number of slip systems result in poor ductility when compared to the fcc structure of Al. In these alloys, thermo-mechanical processing such as extrusion and rolling result in the alignment of basal planes, which lead to the weak ductility if the load is applied parallel to the basal plane aligned direction [6]. Upon the addition of nanoparticles, it was reported the deformation mechanism of Mg matrix is altered, where the non-basal slip systems are activated, which contributed to the improvement of ductility [26]. Work by Goh et al. reported that the ductility of pure Mg is increased by 70 ~ 100% by adding carbon nanotubes [27]. Cao et al. reported that the room temperature ductility is increased by more than 100% in Mg-4Zn by adding 1.5 vol.% of SiC nanoparticles [28].

2.1.1.3. Effects of nanoparticles on secondary phases and grains

1) Secondary phase control

The ceramic nanoparticles and microparticles are known to have strong attractive interactions with certain impurity elements. In the case aforementioned Mo alloys, La_2O_3 nanoparticles attracted N and O solute atoms, and prevented their segregation on grain boundaries

[25]. In conventional steelmaking process, limestone, $CaCO_3$, and dolomite, $CaMg(CO_3)_2$, are added into molten steel to prevent the formation of impurity phases containing Si, S, P, etc., by reacting with these impurity elements and forming slag, which can be later removed [29].

It is worth noticing that in MMNCs the addition of ceramic nanoparticles typically is not for the purpose of impurity gettering compared to that of in traditional steelmaking or in the special case of Mo alloy. In 7075 Al alloy, it was reported that TiC nanoparticles can effectively control the growth of $Mg(Zn,Cu,Al)_2$ intermetallic phase due to the formation of a semi-coherent interface , as shown in Figure 2.3. As a result, these intermetallic phase are finer and more randomly orientated than its counterparts in pure alloy [30], [31]. In a high zinc Al-Zn-Mg-Cu alloy, the presence of TiC nanoparticles modified the as cast intermetallic phases such as $MgZn_2$ and Al_7Cu_2Fe, and promoted their re-dissolution into the matrix upon solutionizing treatment [32].

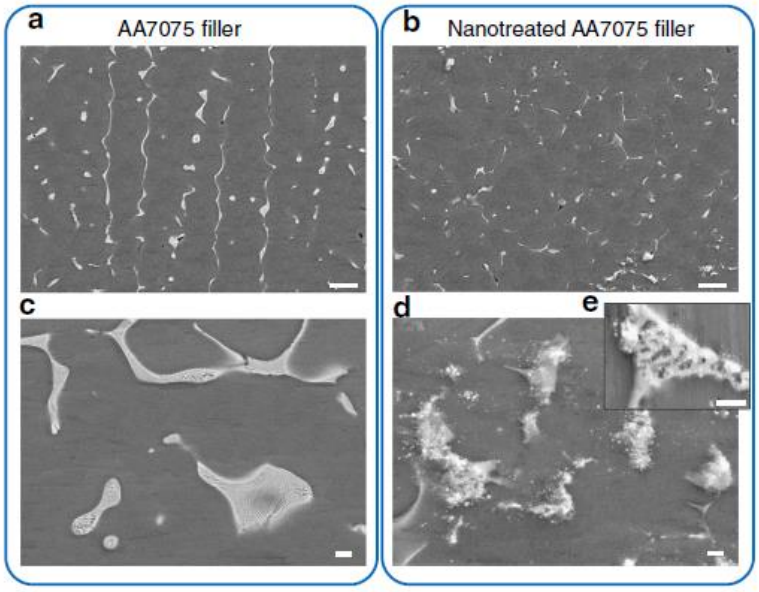

Figure 2.3: SEM micrographs of secondary phase morphology in AA7075 (a and c), and in AA7075-TiC (b and d)[31].

2) Grain refinement

Grain refinement is a long-standing goal in metallurgy, as it can simultaneous improve the strength and ductility of an alloy [25]. Therefore, the grain refinement effect of nanoparticle is of importance.

During solidification, heterogenous microstructural features, such as impurities and inclusions, can promote heterogenous nucleation. In the case of MMNCs, intentionally added nanoparticles serve the role of heterogenous microstructural features. T.E. Quested reported that Ti and B are effective grain refiner in Al alloys due to the formation of fine TiB_2 particles. During nucleation, an initial layer of Al_3Ti forms first on the TiB_2 particle surface to further nucleate Al and produce a significantly refined microstructure [33]. Similar grain refining effect was reported in various Mg based MMNCs, such as Mg-SiC [28], [34], and Mg-Al_2O_3 [35]. In the as-cast Mg–Al_2O_3 alloys, the grain refining effect of Al_2O_3 manifested in breaking up the columnar grains, that is common in as-cast alloys, into equiaxed grains, which is normally found in wrought alloys, as shown in Figure 2.4 [35].

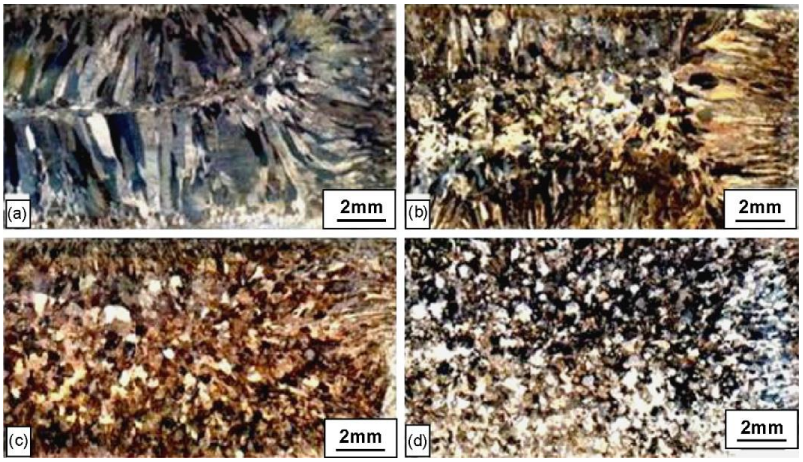

Figure 2.4: Macro-etched as-cast samples: (a) pure Mg, (b) Mg – 0.5% Al_2O_3, (c) Mg – 1% Al_2O_3, and (d) Mg – 2% Al_2O_3. As transition from columnar grains to equiaxed grains is observed [35].

Aside from being effective in promoting heterogeneous nucleation during solidification, nanoparticles can serve as anchor points that hinder the movement of liquid-solid front during solidification or solid-solid front during grain growth. In the case of grain growth in a solid metal, this effect is known as Zener pinning [36]. The grain refinement due to the nanoparticle pinning was reported in a Cu-WC MMNC, in which the addition of 5 vol.% WC nanoparticles resulted in the grain size around 400 nm, in contrast to the ~100 μm in pure WC under the same condition. As the volume fraction of WC nanoparticle increases (between 5 to 30%), the grain size of Cu decreases due to smaller interparticle spacing (d), which is given by Eqn. 6 [37].

$$d = r(\frac{4\pi}{3f_v})^{\frac{1}{3}} \quad \text{Eqn. 6}$$

Where d is the theoretical center-to-center interparticle spacing, r is the radius of the particles, and f_v is the volume fraction of the particles. The decrease of grain size with increase of particle volume fraction is shown in Figure 2.5.

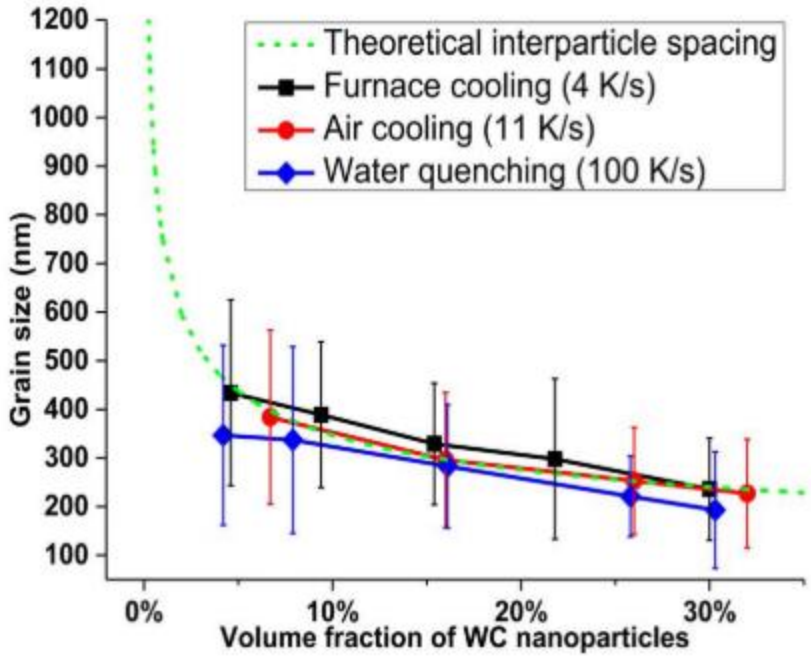

Figure 2.5: Average Cu grain sizes for different volume fraction of nanoparticles under different cooling rates [37].

This phenomenon is due to the pinning effect of the WC nanoparticles during the solidification. The Cu solid-liquid front was unable to engulf the WC nanoparticle, therefore being pinned down as they come into contact. As a result, the grain can only grow within the free space between the particles, and the final grain size is roughly equal to the theoretical interparticle spacing. This mechanism is illustrated in Figure 2.6 [37].

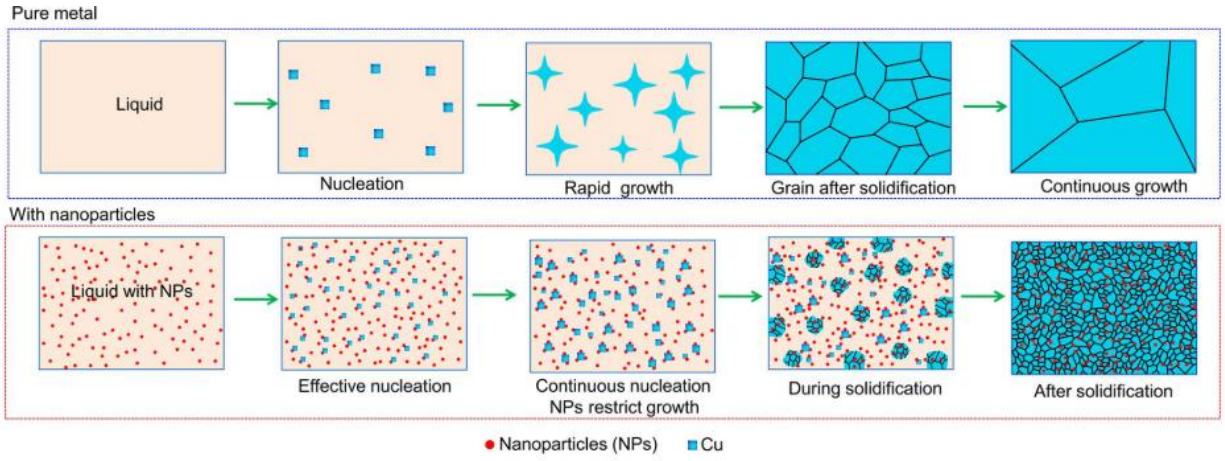

Figure 2.6: Schematic illustrations of phase evolution during solidification of pure metal and metal with nanoparticles [37].

As a consequence of grain refinement, the strengthen of the metal matrix also increases due to the Hall-Petch effect. The influence of grain size on the strength of metal matrix stems from the difficulty for dislocation to traverse through grain boundary, due to the different crystallographic orientation of adjacent grains, which impede the dislocations from moving in a continuous slip plane. Consequently, a metal matrix with finer grains will have higher strength comparing to one with coarser grains. The strengthening effect, $\Delta\sigma_{H\text{-}P}$, due to grain size, d, is given by Eqn. 7 [16].

$$\Delta\sigma_{H-P} = \frac{k_y}{\sqrt{d}} \qquad \text{Eqn. 7}$$

where k_y is the strengthening coefficient.

The strength gain due to the Hall-Petch effect can be significant, on the same magnitude compared to that of the Orowan strengthening (per section 2.1.1.1.). For example, in mild steel (k_y=0.74 MPa·$m^{0.5}$), the Hall-Petch strengthening effect is 74, 234, and 740 MPa for grain size of 100, 10, and 1 μm, respectively. In this case, the Hall-Petch effect becomes significant when the grain size

reaches 10 μm, and dominant when the grain size is down to 1 μm. This is the reason that grain refinement is a long-standing goal of steel metallurgy.

2.1.2. The effect of nanoparticles in Fe-based MMNCs

Fe-based MMNCs fulfill certain applications that cannot be fulfilled by light metal based (Al, Mg, etc.) MMNCs, such as in high temperature and high irradiation environment, or application with high demand on stiffness. To this end, certain effects of nanoparticles are sought after in Fe-based MMNCs, while not being emphasized in systems reviewed in section 2.1.1. .

2.1.2.1. The effect of nanoparticles on creep resistance

Alloys that can operate in harsh service environments, with different combination of high temperature, high stress, high irradiation, and aggressive chemicals, are in demand. For example, alloys in turbine blades experience the combination of high temperature, high stress, and highly oxidative atmosphere, while cladding tubes in nuclear reaction face the combination of high temperature, high stress, high irradiation, and corrosive chemicals. Stainless steels (ferritic, austenitic, or martensitic) are considered as one of the candidates for nuclear cladding application. However, without reinforcement, stainless steels do not have sufficient creep resistance, hence ODS stainless steels are developed to meet such demand [15][38].

The presence of well dispersed oxide nanoparticles has significantly beneficial effect on the creep resistance of the matrix, which are governed by two mechanisms: namely, Orowan bypassing, for low temperature, and interfacial pinning, for high temperature [39].

The Orowan bypassing mechanism is similar in nature to the Orowan strengthening effect, which was reviewed in section 2.1.1.1. . When dislocation encounters hard, non-shearable nanoparticles with incoherent (or semi-coherent) interface, the dislocation can bypass the

nanoparticle by either climbing over (or under) the nanoparticle entirely or forming a closed loop around the nanoparticle. Both processes consume extra deformation energy, therefore either delaying or preventing the movement of the dislocation. As a result, the creep resistance, which is determined by the resistance to dislocation movement at elevated temperature, of the matrix is improved [39].

At higher temperature, the interfacial pinning mechanism takes over Orowan bypassing. This mechanism is due to the attractive interaction between matrix dislocations and the incoherent interface of the nanoparticles. The attraction causes the dislocation segment near the particle to maximize its length in the particle interface. Even dislocations whose slip plane lies above or below the particle are attracted and may end up attaching to the interface after some climb and glide motion. When dislocations are attached to the interface, it takes extra deformation energy for the dislocation to detach and break free from the nanoparticle. As such, the creep resistance is improved. The temperature dependent effect of Orowan bypassing and interfacial pinning mechanism is shown in Figure 2.7[39]. The exceptional creep resistance of ODS stainless steel is shown in Figure 2.8 [15], where the non-reinforced conventional Fe-18Cr stainless steel failed due to creep deformation under 10 min at 650˚C-180MPa condition, while the Fe-18Cr-ODS stainless steel lasted over few thousands of hours.

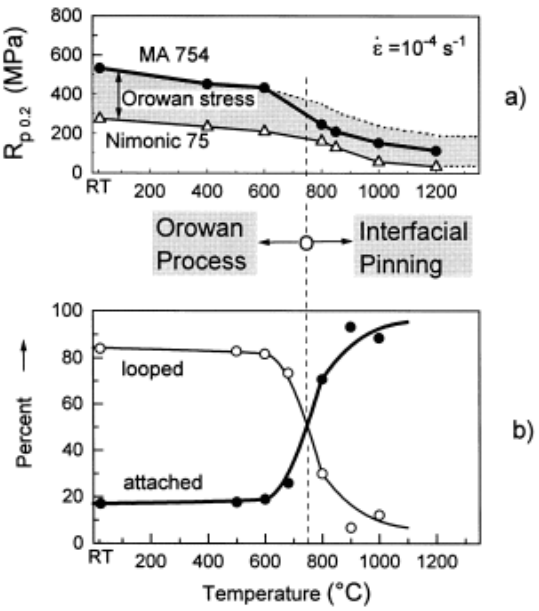

Figure 2.7: Strength and dislocation configuration of the ODS superalloy MA 754 between room temperature and 1200°C. (a) Compressive 0.2% yield stress. Shaded: Orowan stress given as low-temperature yield stress-increment due to oxide dispersoids. (b) Percentage of dislocations looped (Orowan) vs percentage attached (interfacial pinning) to particles; strain rate 10^{-3} s^{-1} [39].

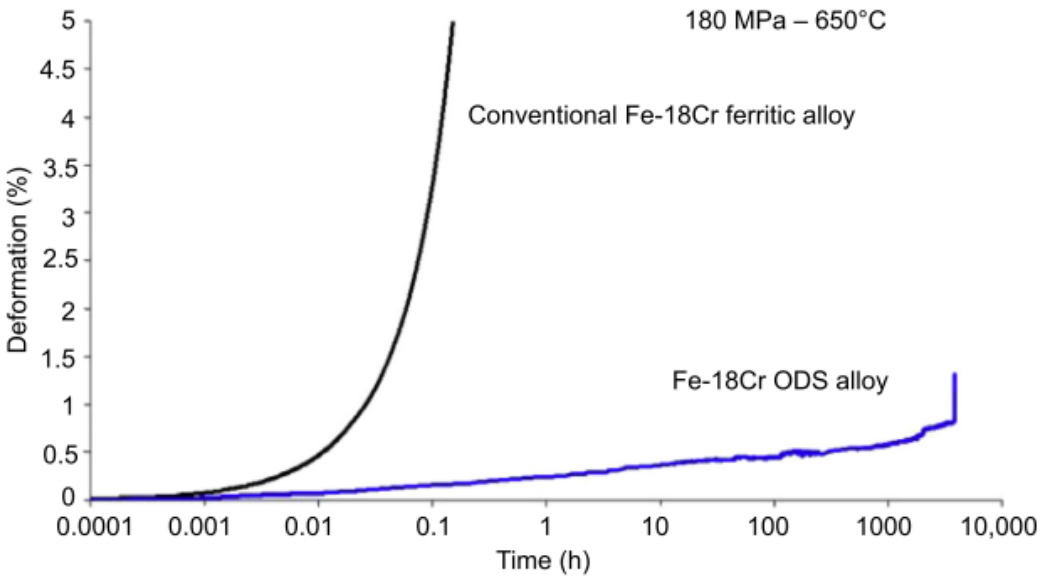

Figure 2.8: Comparison between a Fe-18Cr conventional alloy and a Fe-18Cr ODS alloy during a creep test at 650C-180 MPa. The rupture time is below 10 min for the non- reinforced Fe-18CR against few thousands of hours for the Fe-18Cr-ODS [15].

2.1.2.2. The effect of nanoparticles on irradiation resistance

In nuclear applications, the material is often subject to neutron irradiation, which leads to the displacement of atoms from their lattice positions. The accumulation of these displaced atoms causes buildup of dislocations and formation of vacancies. At high temperature, these vacancies are more mobile and prone to form voids when combined. This phenomenon in which the material expands in volume due to exposure to intense neutron irradiation is referred to as void swelling [40].

The presence of finely dispersed nanoparticles (primarily Y_2O_3) in Fe matrix significantly improves the irradiation resistance of the steel. As the irradiation damage accumulates, the microstructure of the steel needs to evolve in order to accommodate. In a regular non-ODS steel, the voids formed during neutron irradiation will migrate to weak points in the microstructure, such

as grain boundaries. They could also combine with gas atoms, such as He and H, which were diffused into the steel from the surrounding chemical environment, and cause embrittlement to the steel. Under the combination of these microstructural changes, the regular non-ODS steel does not possess sufficient resistance towards long term irradiation damage [15], [40].

In an ODS steel, the oxide nanoparticles serve as very strong traps for helium and other irradiation induced defects. When helium atoms are trapped onto the nanoparticle interface, they form tiny and high-pressure gas bubbles at the interface with the matrix. The presence of these tiny bubbles adds to the irradiation resistance because they act as stable sink-recombination centers that recombines excess vacancy and self-interstitial displacement damage defects [41]. The bubbles also act as deep traps for additional helium, reducing their accumulation on the grain boundaries, which lead to degradation of the mechanical properties. The complex interactions between an oxide nanoparticle and helium atoms are shown in Figure 2.9.

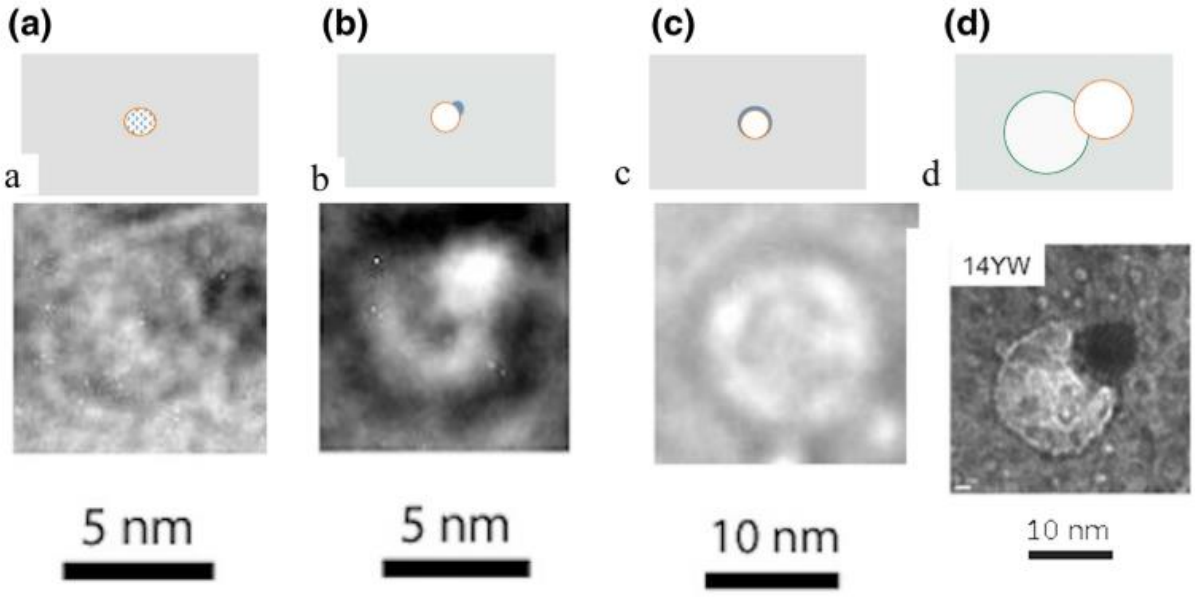

Figure 2.9: (a) Illustrations of an oxide containing helium. (b) An oxide with an attached helium bubble. (c) An oxide surrounded by a helium bubble or bubbles. (d) A larger oxide that nucleates

a growing void. Schematic illustrations are on the top and TEM examples of these oxide-cavity arrangements are shown on the bottom [41].

In addition, oxide nanoparticles are also able to accommodate other defects simultaneously. Unlike grain boundaries, free surfaces and other microstructure sinks, the oxide nanoparticles are unaffected by the flow of defects, in which incoming defects, such as vacancies, do not trigger the outward diffusion of Y or O atoms into the steel matrix. As such, these nanoparticles can absorb defects without contributing to other microstructural changes, such as void swelling, hardening, creep, etc. Instead, they only facilitate the recombination of defect pairs (vacancies and self-interstitial atoms), hence significantly improving the irradiation resistance of the steel [42].

2.2. **The manufacturing and processing of MMNCs and Fe-based MMNCs**

MMNCs have the potential to deliver improved mechanical properties than their conventional alloy counterparts by a favourable combination of the properties of the metal matrix and the nanoparticles. In some cases, such as in ODS steels, the required properties (creep and irradiation resistance) can be delivered only by the reinforcement of nanoparticles, in which the traditional metallurgical methods such as heat treatment and alloying are proven to be insufficient. However, the realization of these improved properties relies heavily on the uniform dispersion of nanoparticles in the metal matrix, as well as the ability to control the particle size and volume fraction. Due to their high surface area, nanoparticles are more reactive than their bulk counterparts; they also tend to agglomerate and form clusters, since the van der Waals forces between identical materials are attractive and the formation of clusters reduces overall surface energy [43]. As such, the incorporation and dispersion of nanoparticles are challenging and need to be addressed during the manufacturing. The manufacturing and processing of MMNCs can be divide into two main

categories, *in situ* and *ex situ* processes, in which the main difference is whether the nanoparticles are chemically generated during the process (*in situ*) or directly added from external source (*ex situ*).

2.2.1. *in situ* MMNCs

The *in situ* generation of reinforcing nanoparticles in metal matrix can take place by a solid-solid, solid-liquid, or liquid-liquid reaction between the constituent elements.

1) Solid-solid reaction process

When the matrix element and the ceramic forming elements are in close contact, the exothermic *in situ* reaction can occur with applied heat or, in some cases, without additional heat. Due to the limited diffusion in solid state, the matrix element needs to be mixed with the ceramic forming elements uniformly before the reaction can take place to ensure a uniform dispersion of nanoparticles after reaction. Mechanical alloying (MA) is a solid state powder processing method which involves repeated cold drawing and fracture of particles as a result of the high energy collisions between the milling balls and the powders. This method is widely used to create homogeneous composite powders with uniformly dispersed constituent elements [44].

The solid-solid reaction process involving MA largely follows a general motif as shown in Figure 2.10, regardless of the type of matrix or reinforcing phase. The metallic element A is first mixed with ceramic forming elements X and Y in a MA process to create the multi-element powder that contains uniformly mixed A-X-Y. The multiple-element powders are subsequently heated to initiate the reaction to produce XY. The size and distribution of the XY product is dependent upon the parameters during heating such as temperature, duration, pressure, atmospheric composition,

etc. XY nanoparticles could be generated during the process when these parameters are carefully controlled.

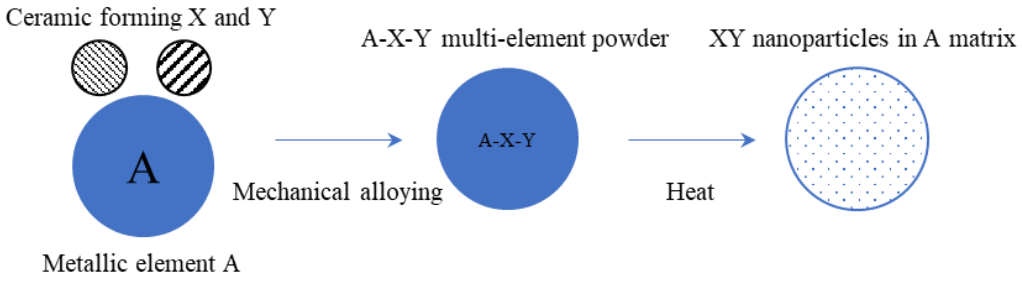

Figure 2.10: Schematic of process for making XY nanoparticle reinforced A-composite with a solid-solid *in situ* reaction.

Bi et al. fabricated Al_4C_3 nanoparticle reinforced Al using MA and annealing. The Al_4C_3 nanoparticles are formed via MA of Al with C and subsequent annealing of as-milled mixture powders. After annealing of as-milled powder mixtures at 873 K, Al_4C_3 nanoparticles with a length of 100-300 nm and a diameter of 2-3 nm were formed *in situ* [45].

With similar method, TiB_2, SiC, TiC, etc. can be generated *in situ* through the MA of Ti, B, Si, or C element powders with Al powders, followed by annealing or sintering of the milled powder. When the *in situ* reaction temperature and time are optimally controlled, these reinforcing particles can reach size as low as ~100 nm [46].

Hsu et al. demonstrated friction stir processing (FSP) as an alternative mixing method to MA [47]. In this work, Al and Ti powders are blended without using MA and sintered at 823 K for 20 min, during which coarse and inhomogeneous Al_3Ti intermetallic particles are formed. The sintered compacts are then subject to multiple pass of FSP with a tool pin at 700-1400 rpm. The FSP can provide severe deformation to promote the mixing of Al and Ti to allow further reaction. The processing time of the material subjected to thermomechanical treatment in FSP is very short,

of the order of seconds. Thus, the exothermic reaction can proceed very fast at the Al-Ti interface, thereby retarding the growth of Al_3Ti particles and leading to the dispersion of very fine Al_3Ti nanoparticles in Al matrix, as shown in Figure 2.11 [47].

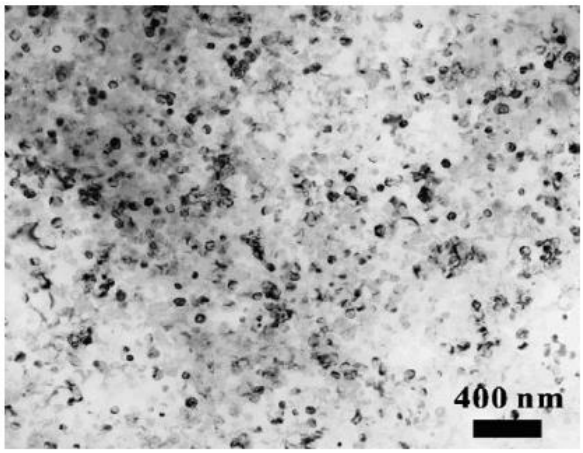

Figure 2.11: TEM image showing the Al_3Ti nanoparticles uniformly distributed in the Al matrix of an Al-10Ti MMNC by FSP method [47].

The solid-solid route to produce *in situ* MMNCs has the inherent advantage of good control in particle size, low requirement on the experiment equipment, high uniformity of nanoparticles in the final product. It is also significantly hampered by the high cost of the powdered metals and the low production volume due to the size limitation of MA. Therefore, this route is not the preferred route for industry when large production volume is required.

2) Solid-liquid and liquid-liquid *in situ* reaction

Liquid metallurgy is an integral part of metal and alloy manufacturing due to its low cost and high production volume. As such, solid-liquid and liquid-liquid *in situ* reaction for MMNC production, in which the metal matrix is in molten state while the ceramic forming elements are either in solid state or dissolved liquid state, has great potential scalability.

Flux-assisted synthesis (FAS) (also known as molten salt assisted synthesis) is a widely used method to incorporate nanoparticles into molten metal (mostly Al and Cu). Lakshmi et al. demonstrated the manufacturing of TiB_2 reinforced Al using FAS method. In this process a mixture of salts, K_2TiF_6 and KBF_4, are introduced into a stirred Al melt. Exothermal reactions between the salts and the molten aluminum take place according to the following sequences [48]:

$$3K_2TiF_6 + 13Al \rightarrow 3TiAl_3 + 3KAlF_4 + K_3AlF_6 \quad (1)$$

$$2KBF_4 + 3Al \rightarrow AlB_2 + 2KAlF_4 \quad (2)$$

$$AlB_2 + TiAl_3 \rightarrow TiB_2 + 4Al \quad (3)$$

The experimental setup is shown in Figure 2.12.

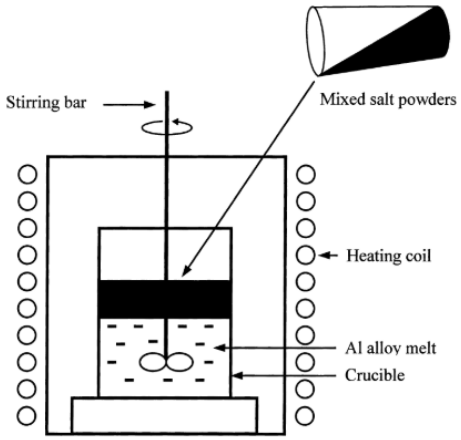

Figure 2.12: Schematic diagram of the experimental setup for manufacturing *in situ* MMNCs by FAS [48].

The TiB_2 particles produced in this process are mostly submicron sized. In recently years, this process has been significantly improved to achieve TiB_2 particle size below a few hundred nanometers. Chen et al. combined a gas atomization process with the FAS process to produce nano-TiB_2 reinforced Al-Cu-Mg alloy powder for 3D printing. The TiB_2 particle size are mostly below 200 nm [49]. Li et al. used similar gas atomization combined with FAS to produce nano-

TiB_2 reinforced AlSi10Mg alloy powder [50]. The *in situ* reaction product can be changed from TiB_2 to TiC, when the source of B, KBF_4, is replaced with carbon source, such as carbon black or charcoal powder [32], [51].

A liquid-liquid reaction process, called the Mixalloy Process, was developed by Sutek Corporation [46]. This process involves the reaction between two molten metal streams to form refractory particles. Two or more high-speed, turbulent, molten metal streams containing ceramic forming elements, for example Cu-Ti and Cu-B, are made to impinge upon one another in a mixing chamber, resulting in intimate mixing and reaction to produce the second phase. The resulting mixture can then be cast in a mold or rapidly solidified via melt spinning or atomization. This technology is effective in producing copper matrix composites reinforced with TiB_2 nanoparticles (50 nm) for the electrical applications [46].

2.2.2. *ex situ* MMNCs

1) Solid state process

The manufacturing of *ex situ* MMNCs using a solid state process shares similarity with that of *in situ* MMNCs reviewed in previous section. Instead of using ceramic forming element X and Y to produce XY nanoparticles in metal A, the XY nanoparticles are directly used. As such, the MA process serves only to uniformly disperse XY nanoparticles in metal A powders. The subsequent heating and consolidation no longer seek to promote additional reaction, but only to create a bulk product with low residual porosity. The general motif for manufacturing of *ex situ* MMNCs using a solid state process is shown in Figure 2.13.

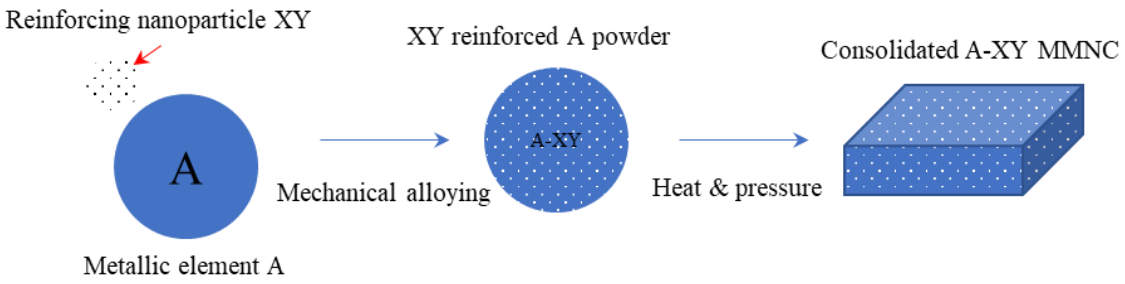

Figure 2.13: Schematic of process for making XY nanoparticle reinforced A-composite with a solid state *ex situ* process.

Tang et al. used hot isostatic pressing (HIP) and rolling to consolidate cryomilled AA5083 powders and SiC nanoparticles (25 nm) for forming the MMNC [52]. The blended powders were cryomilled in liquid nitrogen for 8 h. The SiC nanoparticles are uniformly dispersed in the AA5083 powders as shown in Figure 2.14 [52].

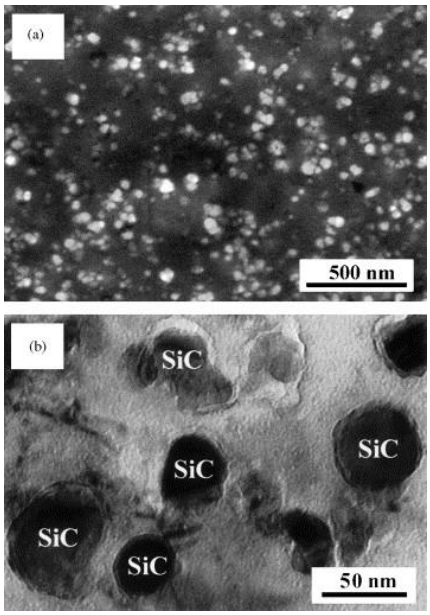

Figure 2.14: (a) SEM and (b) TEM images showing the distribution and the shape of SiC particles in the cryomilled Al-5083/SiC composite powder [52].

Other reinforcing particles such as Al_2O_3, TiC, TiB_2, etc. can also be incorporated into various metallic powders such as Al and Mg using similar process. The mixing and consolidation parameters such as mixing RPM and duration, consolidation temperature, pressure, and duration, will determine the size and distribution (agglomeration behavior) of the nanoparticles, and the porosity, grain size, and mechanical properties of the final MMNC[53].

2) Liquid state process

The production of *ex situ* MMNCs using a liquid state process is more scalable than the solid state route due to its similarity with the conventional alloy casting method. The liquid state process requires the incorporation of reinforcing nanoparticles into a metal melt followed by casting. This is a challenging process during both the incorporation stage and the casting stage. During incorporation stage, the metal melt surface is often covered with a thin layer of metal oxide that serves as a blockade to the nanoparticle entry. Even after the nanoparticles are successfully incorporated into the metal melt, the nanoparticles are still subject to dissolution or reaction with the metal matrix, and agglomeration due to the van der Waals attraction force between the nanoparticles, which need to be mitigated during casting stage [43][54].

Cao et al. reported the production of Mg–SiC MMNCs by ultrasonic cavitation based casting process [28][34]. In his works, high intensity ultrasonic waves were applied to disperse the SiC nanoparticles in molten Mg, as shown in Figure 2.15. The ultrasonic source produces acoustic transient cavitation effect, which induces a violent collapse of micro gas bubbles around the nanoparticle clusters, thus overcoming the van der Waals attraction force between the nanoparticles, breaking the clusters, and dispersing them into individual nanoparticles into the matrix [53]. While most of the SiC nanoparticles were uniformly dispersed in Mg matrix, SiC

clusters were still observed in selected areas. It is noted that the ultrasonic dispersion method also faces the issue of scalability, since the ultrasonic device cannot be easily scaled up like the size of the melt can [54].

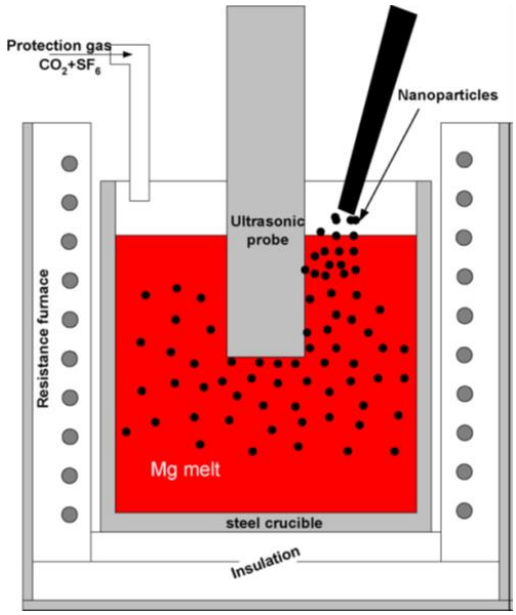

Figure 2.15: Experimental setup for ultrasonic dispersion of SiC in Mg melt [28].

Liu et al. demonstrated the production of Al–TiC MMNCs using molten salt assisted casting process [54]. In this work, molten fluoride salt, KAlF4, is utilized to dissolve the oxide film covering the Al melt, thereby allowing the TiC nanoparticles to enter, as shown in Figure 2.16. It is reported that the incorporated TiC nanoparticles are mostly found in micro-sized pseudo clusters, and some fluoride salts are entrapped in the solidified metal matrix. This method enables the incorporation of high volume fraction of nanoparticles (up to 9%) in the Al melt before the viscosity becomes too high. The MMNC product with high nanoparticle loading can be subsequently diluted with Al and other alloying element to create TiC reinforced aluminum alloy at desired chemical composition and nanoparticle volume fraction. Sokoluk et al. first manufactured Al-8 vol.% TiC MMNC master using Liu's molten salt assisted casting process, then

diluted the MMNC master to create AA7075 welding filler wire containing 1.7 vol.% TiC [31]. Zuo et al. first manufactured Al-6 vol.% TiC MMNC master using the same process, then diluted the MMNC master to create AA7075 with 1 vol.% TiC to tackle hot cracking issue during casting [30].

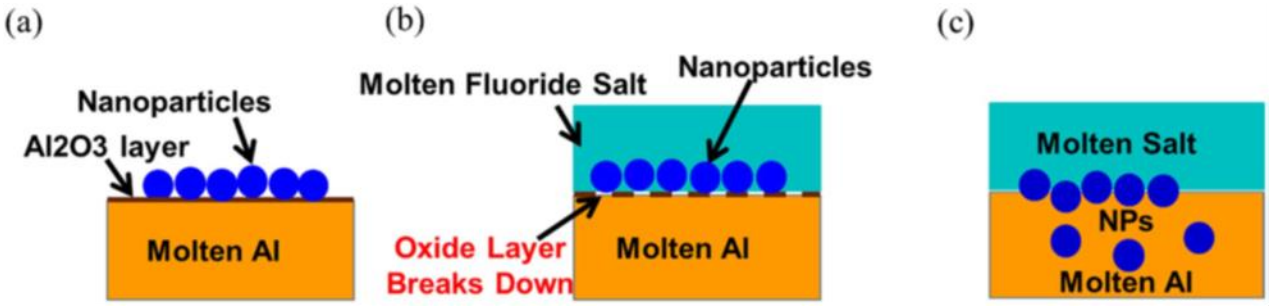

Figure 2.16: Schematic mechanism of nanoparticle incorporation assisted by molten salt; (a) non-wetting between the nanoparticles and the melt due to oxide layer ; (b) dissolution of oxide layer by molten salt; and (c) nanoparticle incorporation [54].

2.2.3. Fe-based MMNCs

2.2.3.1. *ex situ* process

The manufacturing of Fe-based *ex situ* MMNCs is more challenging than Mg- or Al-based MMNCs reviewed in section 2.2.2. One important criterion for *ex situ* MMNCs is that the reinforcing nanoparticles need to be relatively stable within the matrix at elevated temperatures such as during high temperature sintering or molten state casting. Unstable nanoparticles are subject to dissolution in or reacting with the matrix during these processes, thereby losing their small sizes. For metal matrices like Mg and Al, particles like TiB_2, TiC, Al_2O_3, SiC, etc. are all relatively stable, which allows the liquid state incorporation to be carried out. However, steels have significantly higher melting point (1450~1540 ˚C) than the aforementioned metals (Tm<660˚C),

which results in the strong reactivity of the steel melt that can dissolve most of the reinforcing nanoparticle candidates, such as borides, carbides, and nitrides, except several oxides with high stability. To this end, the manufacturing of Fe-based *ex situ* MMNCs using a liquid state process remains a challenging task. Instead, a solid state process involving MA has been demonstrated with much more success.

During MA process, the high energy collisions between hard balls, metal powders, and oxide particles for extended duration cause very large strain. Oxides generally have very low solubility limit in metals, making them difficult to dissolve in molten metals. However, large mechanical energy during the MA process can gradually fracture and eventually decompose the oxides. Kimura et al. studied the decomposition of Y_2O_3 in Fe-24Cr stainless steel powder during super-heavy deformation [55]. The decomposition of Y_2O_3 was characterized by XRD analysis, as shown in Figure 2.17. The diffraction peaks for Y_2O_3 and the bcc matrix are clearly visible for the as-mixed powder, indicating the separation of the two phases. After 36 ks of ball milling, the peaks for Y_2O_3 are no longer detectable, indicating the full decomposition of Y_2O_3 in the matrix.

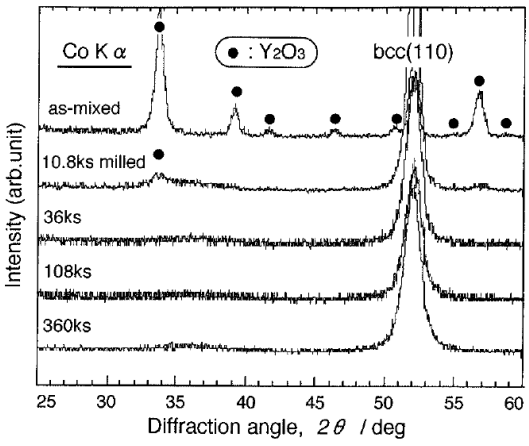

Figure 2.17: XRD patterns of a Fe-24Cr-15Y_2O_3 powder mixtures at various ball milling duration [55].

During hot consolidation of the milled powders, the decomposed Y_2O_3 can reprecipitate as nanoparticles [55]. Ohtsuka et al. used MA to produce Fe-9Cr-0.36Y_2O_3-xTi powders with varying Ti concentration. The as-milled powders were hot extruded at 1423 K to form rods [56]. Ghayoor et al. used MA to produce 304L stainless steel powders with 5 wt.% Y_2O_3 nanoparticles. In this work, a short milling time of 4 hours were used so that Y_2O_3 nanoparticles did not fully decompose in the matrix. The consolidation was done through selective laser melting (SLM)[57], [58]. AlMangour et al. used the combination of MA and SLM to produce TiC reinforced 316L [59] as well as TiB_2 reinforced 316L nanocomposites [60]. Due to the reactive nature of TiB_2 and TiC in Fe matrix, these *ex situ* nanocomposites cannot be made using conventional method such as casting. However, during SLM, the heating and cooling rate are sufficiently fast, that the reaction is very limited. Only a thin reaction layer exists between the nanoparticle and the matrix [60].

2.2.3.2. *in situ* process

Fe-based MMNCs, both in powder form and in bulk form, can be manufactured with *in situ* process. Qin et al. demonstrated the production of *in situ* NbC nanoparticle reinforced Fe powder using MA [61]. In this work, pure Nb powder (APS<10 μm) was ball milled with pure graphite powder (APS <40 μm) with a Nb:C molar ratio of 1:1 in argon atmosphere for 8 hr. The same amount of Fe powder (APS <140 μm) was added to the mixture and ball milled for extra 4 hr. The final mixture was het treated at 750 ˚C for 0.5 hr. The resulting powder contains an Fe matrix reinforced with NbC nanoparticles (APS<50 nm). The NbC nanoparticle reinforced Fe powder was then added into molten low-carbon steel to produce Fe-based nanocomposite. The microstructure of the as-milled nano-NbC/Fe powder and the low-C steel after 0.25 wt.% NbC

addition is shown in Figure 2.18 [61]. After dilution into molten steel, the NbC particles remained at small sizes around 10-30 nm, indicating limited dissolution or reaction with the matrix.

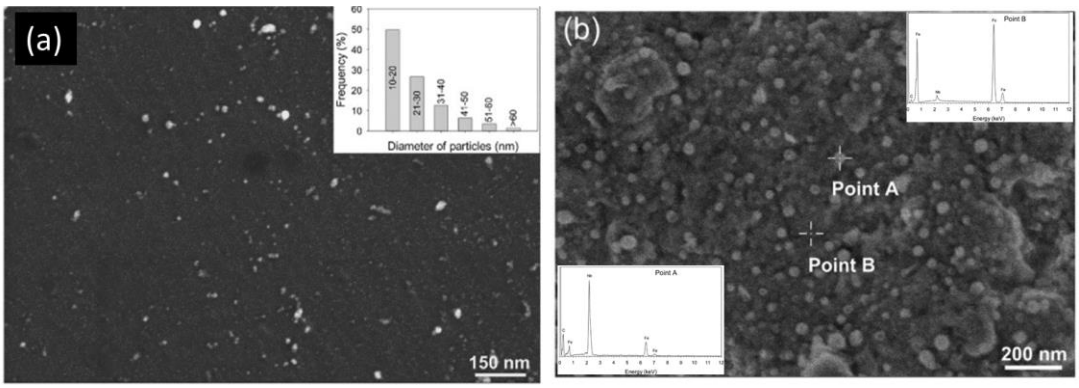

Figure 2.18: (a) Particles and their size distribution in the ferrite of the cast steels with 0.25 wt.% NbC addition. (b) SEM observation of the nano-NbC/Fe powder with EDS point analysis. Figure rearranged based on Qin's data [61].

The Fe-Ti-B system is a notable alloy system in Fe-based composites due to the formation of TiB_2 particles in Fe matrix during solidification. TiB_2 as a reinforcing phase in Fe matrix also offers increased strength, Young's modulus, and reduced density. The calculated Fe-Ti-B phase diagrams are shown in Figure 2.19 [62]. There exists a eutectic point at ~6.5 mol.% TiB_2 in Fe matrix with a low melting point of ~1580K (Figure 2.19c). Due the stability of TiB_2 in Fe matrix, the TiB_2 solubility is very low, indicating that the system cannot be solutionized. Zhang et al. reported the *in situ* formation of fine TiB_2 particles in Fe matrix using casting method. In this work, an alloy with nominal composition of Fe–10.1 Ti–3.86 B (wt.%) was melted in vacuum arc furnace [9]. The cooling rate of the melted sample was controlled by casting into water-cooled copper moulds from 40 mm to 1 mm internal thickness (smaller mould internal thickness permits more rapid cooling). Higher cooling rate (~10^5 K/s) was also achieved by using melting spinning. As the cooling rate increases, the TiB_2 particle size and the matrix grain size both decreases. At low

cooling rate, 40 mm thick ingot, the TiB_2 particle size is on the order of 40 to 100 μm, and at high cooling rate, melt spun strip, the particle size is around 100 nm [33].

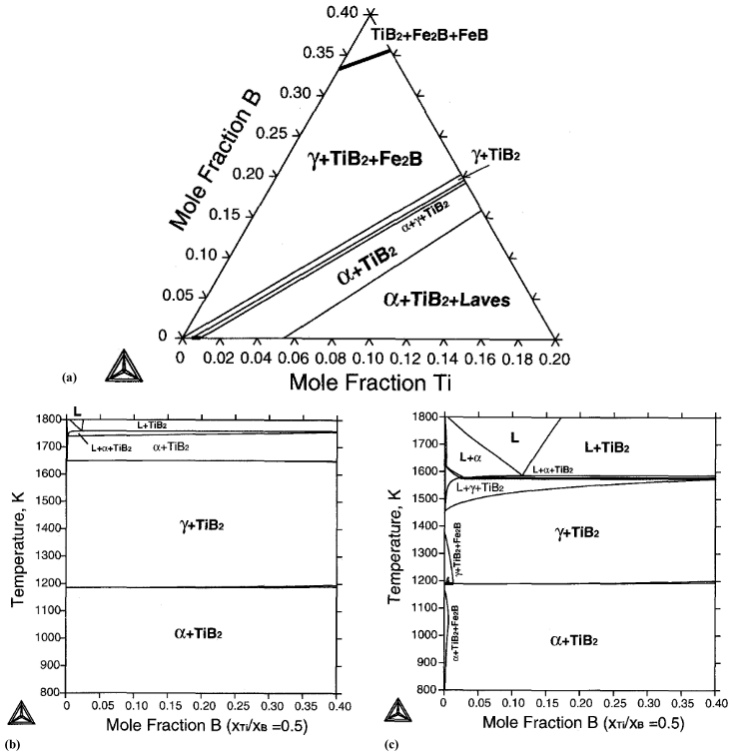

Figure 2.19: Calculated Fe-Ti-B phase diagrams. (a) Isothermal section at 1273 K. (b) Fe-TiB_2 pseudobinary phase diagram. (c) Fe-TiB_2 pseudobinary phase diagram with modified TiB_2 parameter [62].

Springer et al. demonstrated the production of bulk nano-structured Fe-Ti-B high modulus steel by spray-forming a Fe-Ti-B melt onto a steel substrate [8]. Similar to Zhang's work, this method also uses high cooling rate to control the growth of TiB_2 particles during solidification. The spray-forming process is reported to achieve cooling rate in the order of 10^4 K/s [8]. The resulting Fe-matrix has grain size around 400 nm and the TiB_2 particles around 100 nm.

Using fast cooling rate to control the particle size of the reinforcing phase during solidification can also be used to produce *in situ* ODS steel. Moghadasi et al. a method of

producing *in situ* ODS steel via liquid state reaction [63]. In this work, Fe powder (APS~40 μm) were ball milled with TiO_2 nanoparticles (APS~30 nm) for 5 hr to produce Fe-10 wt.% TiO_2 composite powders. The composite powders were sintered at 1393K for 5 hr. Subsequently, the sintered composite powders were melted with a Fe-10Ni-7Mn-1.6Y ingot using vacuum arc melting. The resulting composition is Fe-10Ni-7Mn-1.6Y-1.8TiO_2. The high temperature reaction between Y and TiO_2 produced two products in the matrix, Y_2O_3 and Y_2TiO_5, as shown in Figure 2.20 [63]. The Y_2O_3 and Y_2TiO_5 have an average size of 626 nm and 11 nm respectively. The small size is due to TiO_2 nanoparticles serving as reaction template and oxygen carrier. The fast cooling during arc melting also prevented the continuous growth of the particles during solidification.

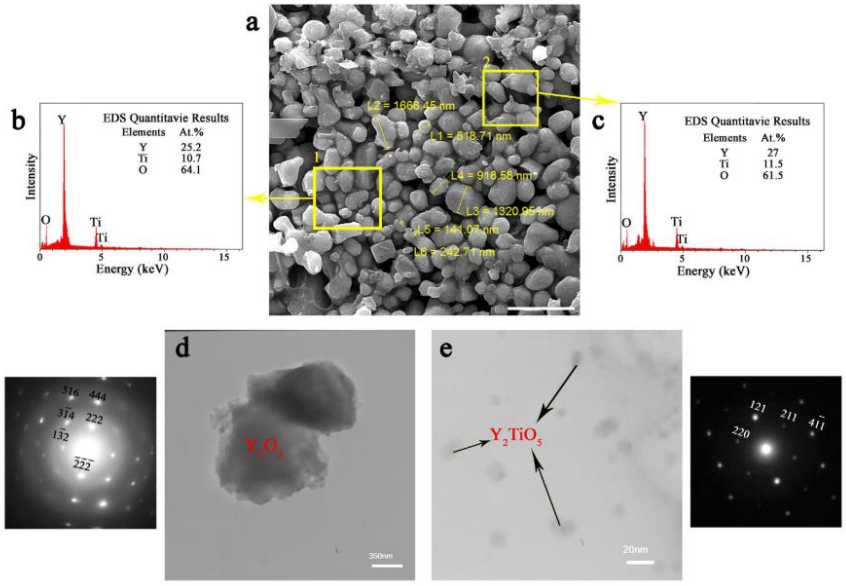

Figure 2.20: (a) FE-SEM image of extracted particles of the FeNiMn-1.6Y-1.8TiO_2 as-cast specimen (scale bars, 3 μ m). (b,c) Chemical composition of extracted precipitates measured by EDS spectrum corresponding to yellow rectangles in the FE-SEM image. (d) TEM image of the extracted particles with its SADP which confirms the formation of Y_2O_3 precipitates. (e) High

magnification TEM image of extracted particles and its corresponding SADP which shows the formation of nanometric Y_2TiO_5 precipitates [63].

2.3. **Effect of minor alloying element on the wettability between molten metal and oxides**

Common engineering alloys such as steels, Al alloys, and Mg alloys typically contain one or more alloying elements. The interaction between multiple alloying elements and nanoparticles becomes highly complicated. Li et al. laid groundwork for understanding and predicting the influence of alloying element on the wetting behavior of oxide particles in a binary alloy system (A-B system) [64]. To understand the effect of adding B solute into A on the oxide wettability, the surface tension between the melt and the oxide (σ_{SL}) needs to be calculated. When the molar fraction of B (x_B) is small, the change of the surface tension (σ_{SL}) is also small and can be approximated with a linear relation. The slope of this linear relation is given by Eqn. 8 [64]:

$$(\frac{d\sigma_{SL}}{dx_B})_{x_B\to 0} = \frac{RT}{\Omega_M}[1 - e^{-\frac{E_{SL}(B)_A}{RT}}] \quad \text{Eqn. 8}$$

$$\Omega_M = N\omega = 1.091N(\frac{V_M}{N})^{\frac{2}{3}} \quad \text{Eqn. 9}$$

The term $(\frac{d\sigma_{SL}}{dx_B})_{x_B\to 0}$ is the slope of surface tension change when solute B is infinitely diluted in A. R is gas constant and T is temperature. Ω_M is the molar interfacial area given by Eqn. 9, in which N is Avogadro's number and ω is the average area of a metallic atom at the interface, V_M is the molar volume of the metal. The term $E_{SL}(B)_A$ is the energy of adsorption of atom B at the metal A-oxide interface in AB alloy with infinitely diluted B, and is given by Eqn. 10:

$$E_{SL}(B)_A = (\sigma_{LV}^B - \sigma_{LV}^A)\Omega_M - (W^B - W^A)\Omega_M - m\lambda \quad \text{Eqn. 10}$$

$$\lambda = zN[\varepsilon_{AB} - \frac{\varepsilon_{AA} + \varepsilon_{BB}}{2}] \quad \text{Eqn. 11}$$

$$E_{LV}(B)_A = (\sigma_{LV}^B - \sigma_{LV}^A)\Omega_M - m\lambda \quad \text{Eqn. 12}$$

$$\left(\frac{y_B}{x_B}\right)_{x_B \to 0}^{SL} = e^{-\frac{E_{SL}(B)_A}{RT}} \quad \text{Eqn. 13}$$

where σ_{LV}^A and σ_{LV}^B are the liquid surface tension of pure A and pure B, W^A and W^B are the work of adhesion of pure A and pure B on the oxide, m is a structure parameter equal to 0.25 for liquid metals, λ is the molar exchange energy of the liquid AB alloy, given by Eqn. 11, in which ε_{AB}, ε_{AA}, ε_{BB} are the interaction energy of the AB, AA, BB atom pair, and z is the coordination number in the liquid (number of nearest neighbors). The term $E_{SL}(B)_A$ describes the tendency of atom B to adsorb onto the surface of the oxide in liquid AB, creating an interfacial layer with enriched B composition (y_B). The ratio between interfacial liquid layer composition (y_B) and bulk liquid composition (x_B) is given by Eqn. 13. Eqn. 12 is the energy of adsorption of atom B at the surface of the metal A from AB alloy infinitely diluted in B, which is used to calculate the variation in surface tension σ_{LV} due to the addition of metal B, as given by Eqn. 14.

$$\left(\frac{d\sigma_{LV}}{dx_B}\right)_{x_B \to 0} = \frac{RT}{\Omega_M}[1 - e^{-\frac{E_{LV}(B)_A}{RT}}] \quad \text{Eqn. 14}$$

Finally, the variation of work of adhesion between the oxide and the metal A with infinitely diluted metal B is given by Eqn. 15, and the variation of contact angle (θ) in Eqn. 16.

$$\left(\frac{dW}{dx_B}\right)_{x_B \to 0} = \left(\frac{d\sigma_{LV}}{dx_B}\right)_{x_B \to 0} - \left(\frac{d\sigma_{SL}}{dx_B}\right)_{x_B \to 0} = \frac{RT}{\Omega_M}\left[e^{-\frac{E_{SL}(B)_A}{RT}} - e^{-\frac{E_{LV}(B)_A}{RT}}\right] \quad \text{Eqn. 15}$$

$$\left(\frac{dcos\theta}{dx_B}\right)_{x_B \to 0} = -\frac{1}{\sigma^A{}_{LV}}\left[\left(\frac{d\sigma_{SL}}{dx_B}\right)_{x_B \to 0} + \left(\frac{d\sigma_{LV}}{dx_B}\right)_{x_B \to 0} cos\theta^A\right] \quad \text{Eqn. 16}$$

$$= -\frac{RT}{\sigma^A{}_{LV}\Omega_M}\left\{\left[1 - e^{-\frac{E_{SL}(B)_A}{RT}}\right] + \left[1 - e^{-\frac{E_{LV}(B)_A}{RT}}\right] cos\theta^A\right\}$$

Where θ^A is the contact angle between the oxide and pure metal A. Based on this set of equation, the change of the work of adhesion ($W(x_B)$)and wetting angle ($\theta(x_B)$) between AB alloy and oxide is summarized in Figure 2.21.

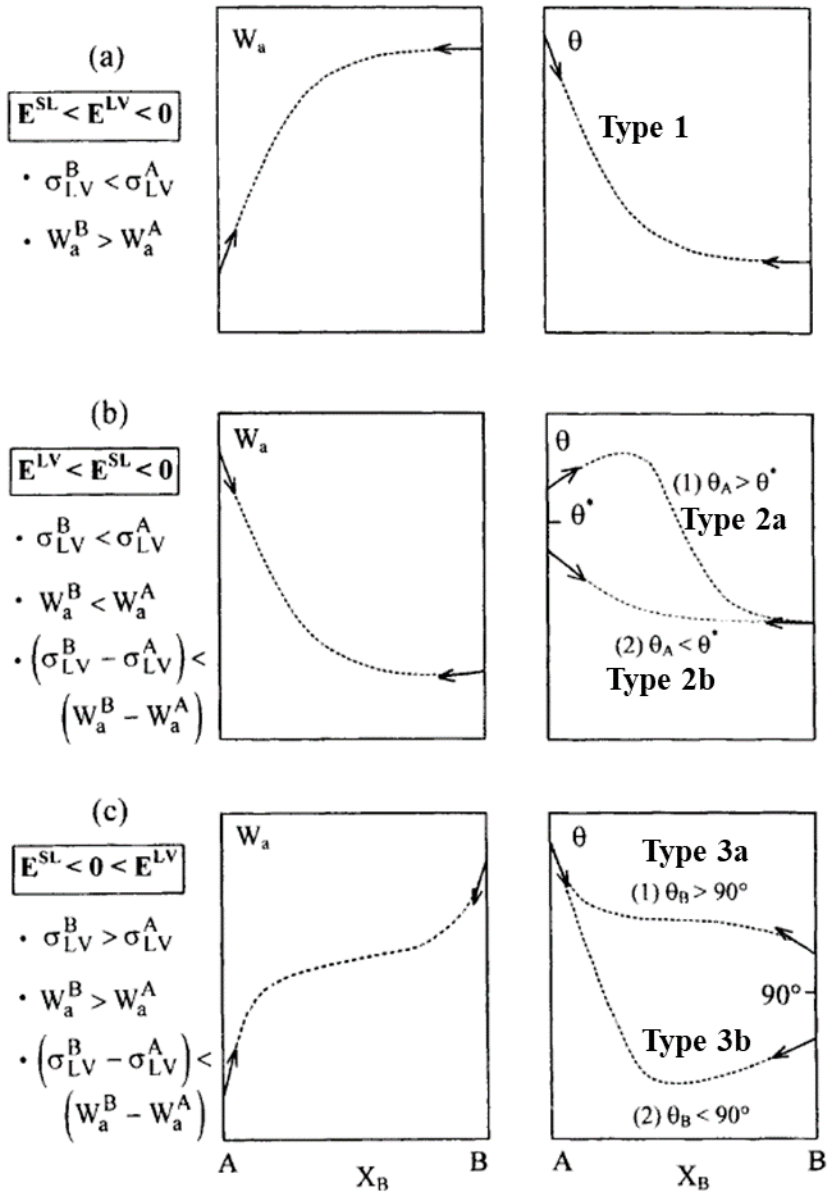

Figure 2.21: Main forms of work of adhesion and contact angle variation for non-reactive A-B liquid alloy and oxide systems, and the corresponding criteria of determination (a-c) [11].

2.4. **Thermally activated dispersion theory for nanoparticles in molten metal**

For *ex situ* produced via solidification method, the prevention of nanoparticle sintering within the molten metal becomes a vital aspect of ensuring the mechanical properties of the final product, as sintered particles are significantly less effective. To this end, understanding of the wetting behaviour of nanoparticles in a high temperature molten metal environment provides important guidelines to the selection of nanoparticle-metal pair and the incorporation/dispersion process.

Chen et al. demonstrated a nanoparticle self-dispersion mechanism in a Mg melt [10]. In this work, a Mg6Zn-1 vol.%SiC nanocomposite was manufactured using ultrasonic processing at 700 ˚C. The ultrasonic processing is effective in uniformly dispersing low volume fraction of nanoparticles, but not for dense nanoparticles. The Mg6Zn-1SiC was then melted and held at 6 torr pressure to evaporate Mg and Zn. The final nanocomposite contained 14 vol.% well-dispersed nanoparticles, as shown in Figure 2.22 a and b. The lack of particle agglomeration and sintering is an indication that the SiC nanoparticles are self-stabilized and dispersed in the melt, because the evaporation of the matrix causes the interparticle distance to shrink making the particles easier to collide. The self-stabilization and dispersion of nanoparticles at high temperature is achieved due to the good wetting between the particles and the melt and low van der Waal attraction between nanoparticles. Figure 2.22 c indicates interaction potential W for two SiC nanoparticles in the melt. Segment 1 is dominated by vdW interaction, in which the particles attract to each other to local energy minimum point, indicated by $W_{vdW\ (min)}$, which is given by Eqn. 17:

$$W_{vdW}(D) = -\frac{\left(\sqrt{A_S} - \sqrt{A_L}\right)^2}{6D}\left(\frac{R_1 R_2}{R_1 + R_2}\right) \qquad \text{Eqn. 17}$$

$$= -\frac{\left(\sqrt{A_{SiC}} - \sqrt{A_{Mg}}\right)^2}{6D}\left(\frac{R_1 R_2}{R_1 + R_2}\right)$$

where D is the distance between two nanoparticles in nanometres, A_{SiC} and A_{Mg} are the Hamaker constants for the van der Waals interaction and are 248 zJ and 206 zJ for SiC and molten magnesium, respectively. R1 and R2 are the radii of two nanoparticles. The $W_{vdW\ (min)}$=-12.17 zJ occurs when D=0.4 nm, where two liquid atomic layers separate two SiC nanoparticles [10].

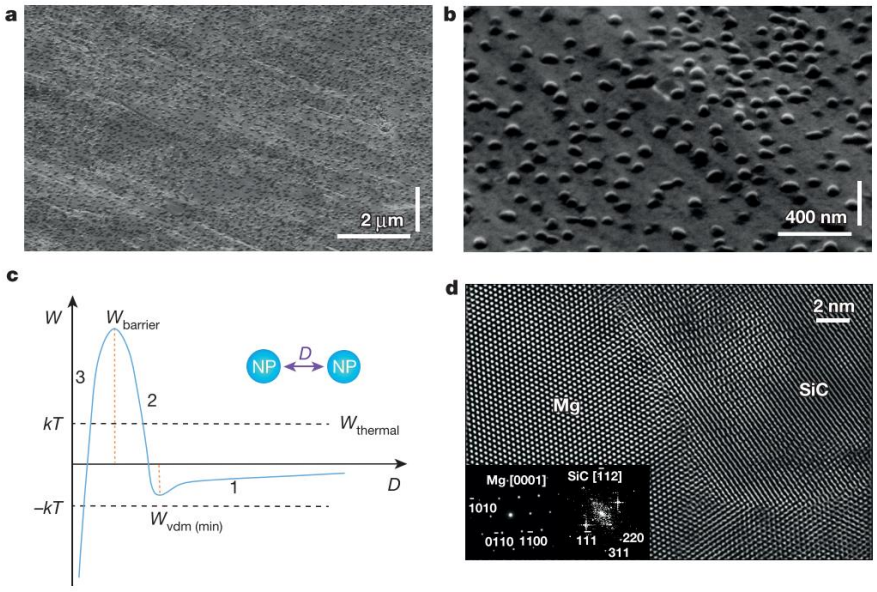

Figure 2.22: Uniform dispersion of SiC nanoparticles in as-solidified magnesium alloy matrix. a, b, SEM images of the Mg2Zn (14 vol% SiC) sample. c, The principle of thermally activated dispersion and stabilization. d, Fourier filtered atomic resolution TEM image showing a characteristic interface between a SiC nanoparticle and the magnesium matrix [10].

Segment 2 shows the increase in interfacial energy when the Mg-SiC interface is replaced by SiC interface. The maximum energy point, $W_{barrier}$, is posed by the wetting between nanoparticles and melt, given by Eqn. 18.,

$$W_{barrier} = S(\sigma_{SiC} - \sigma_{SiC-Mg}) = S\sigma_{Mg}cos\theta \quad \text{Eqn. 18}$$

where where S is the effective area, σ_{SiC} is the surface energy of SiC, $\sigma_{SiC–Mg}$ is the interfacial energy between SiC and magnesium melt, σ_{Mg} is the surface tension of magnesium melt, and θ is the contact angle of magnesium melt on SiC surface (83˚). In this case, $W_{barrier}$ is calculated to be $3.87*10^4$ zJ [10].

Segment 3 of Figure 2.22c is the interfacial energy drop due to SiC nanoparticles contacting and sintering. $W_{thermal}$ =kT is the thermal energy (13.8 zJ) for the Brownian motion of the particles. In this case, the thermal energy (13.8 zJ) is larger than the local minimum vdW potential (-12.17 zJ), allowing the nanoparticles to break free from their attraction, but significantly smaller than the energy barrier imposed by wetting ($3.87*10^4$ zJ), preventing sintering from happening. As such, the SiC nanoparticles were able to self-stabilize and disperse in the melt [10] within a reasonable period of time.

Chapter 3. Invar alloy reinforced by WC nanoparticles

The idea choice of nanoparticle for *ex situ* incorporation into molten steel would be a nanoparticle that has high wettability with the molten steel, which allows a uniform dispersion, and high thermodynamic stability, which prevents it from dissolving or reacting with the molten steel. However, in reality, the wettability and the thermodynamic stability of the nanoparticle is often at a trade-off. Refractory ceramics, such as carbides and borides, have aspects of metallic properties such as high electrical and thermal conductivity, due the nature of their chemical bonding being partly metallic [11]. In low melting point metals, such as Al, Mg, and Zn, these metal-like ceramics are both stable and wettable. But in steels, which have much higher melting point, these metal-like ceramics lack sufficient stability, and are subject to dissolving or reacting with molten steels. On the other hand, ionocovalent ceramics, mostly metal oxides, are significantly more stable than the metal-like ceramics, but they have very poor wettability with molten steels. Therefore, the dilemma of the *ex situ* nanoparticle incorporation into molten steel lies upon adequately addressing the trade-off between wettability and stability. To address this trade-off, there are two possible solutions: 1) suppress the reactivity between the metal-like nanoparticles and the molten metal, or 2) improve the wettability between the non-reacting nanoparticles and the molten metal.

In this study, we attempt to incorporate WC nanoparticles, a metal-like ceramic, into Fe-Ni Invar alloy, a specialty steel that has relatively low melting point (1427 ˚C). The purpose is to try to overcome the wettability and stability trade-off by having a low processing temperature, which suppresses the reaction.

3.1. **Introduction to Invar 36**

Invar is a binary solid solution alloy of Fe and Ni with a Ni content of around 36 wt.%. Invar possesses a uniquely low coefficient of thermal expansion (CTE, $\alpha_{25\sim100\ ^\circ C} \approx 1.5\times10^{-6}/^\circ C$) below its Curie temperature (T_c ~ 277 °C) [65]. For this reason, Invar alloys are frequently used in a wide range of applications that require high dimensional stability, such as large telescopes, precision instruments, and core wires of long-distance power cable [66]. The strengthening of Invar alloy can be achieved primarily through three methods: grain refinement [67], plastic deformation (and severe plastic deformation, SPD) [68], and precipitation hardening [69]–[72]. It is notable that each of the aforementioned strengthening method has its own drawback. As ultrafine-grained and nano-grained Invar alloys are typically prepared by either deposition [73] or SPD[67], they typically exhibit relative low stability against grain growth [74] and have high equipment cost due to the use of process like ECAP. While precipitation strengthening by MC-type carbides or intermetallics are proven to be highly effective, these methods typically result in an undesirable increase of the alloy's CTE value, up to 3 - $4\times10^{-6}/^\circ C$ [75][76]. To this end, it is of interest to develop a simple method of strengthening Invar alloy effectively while preventing a significant increase of the CTE value.

Compared with conventional strengthening methods, the reinforcement of Invar alloy through nano-sized low thermal expansion ceramic particulates is not well studied. In the present work, tungsten carbide (WC) nanoparticles were used to reinforce Invar alloy, due to the combination of high hardness, low CTE, and commercial availability of WC nanoparticles. Two methods of incorporating WC into Invar were attempted here, one was molten salt-assisted incorporation, the other one was powder metallurgy. After incorporation, the Invar/WC was hot and cold worked. The mechanical strength of the WC/Invar was measured with and without cold

working. The CTE values of WC/Invar and regular Invar, manufactured by the same process were measured for comparison.

3.2. **Experimental procedure**

WC nanoparticles (APS 150 nm, US Research Nanomaterials) were used in this work. Its CTE is approximately 5.5 $\times 10^{-6}$/°C. In the molten salt-assisted incorporation method, WC nanoparticles were first milled with borax ($Na_2B_4O_7$) and CaF_2 in a mortar and pestle set. The weight ratio between WC, borax ($Na_2B_4O_7$), and CaF_2 was 2:20:1. The resulting mixture consisted of roughly 5 vol.% TiB_2 nanoparticles and 95 vol.% salt. An Invar 36 ingot, nominal composition Fe36.56Ni0.34Si0.016C0.03Mn (in wt.%), was placed in an alumina crucible and melted at 1430 ˚C in an induction furnace, while the salt mixture was gradually fed onto the melt surface, as shown in Figure 3.1. The volume percentage of WC nanoparticle in the Invar alloy was designed to be 5%, referred to as Invar-5WC herein. After incorporation, the melt was furnace cooled. The solidified Invar/WC ingot was examined with SEM.

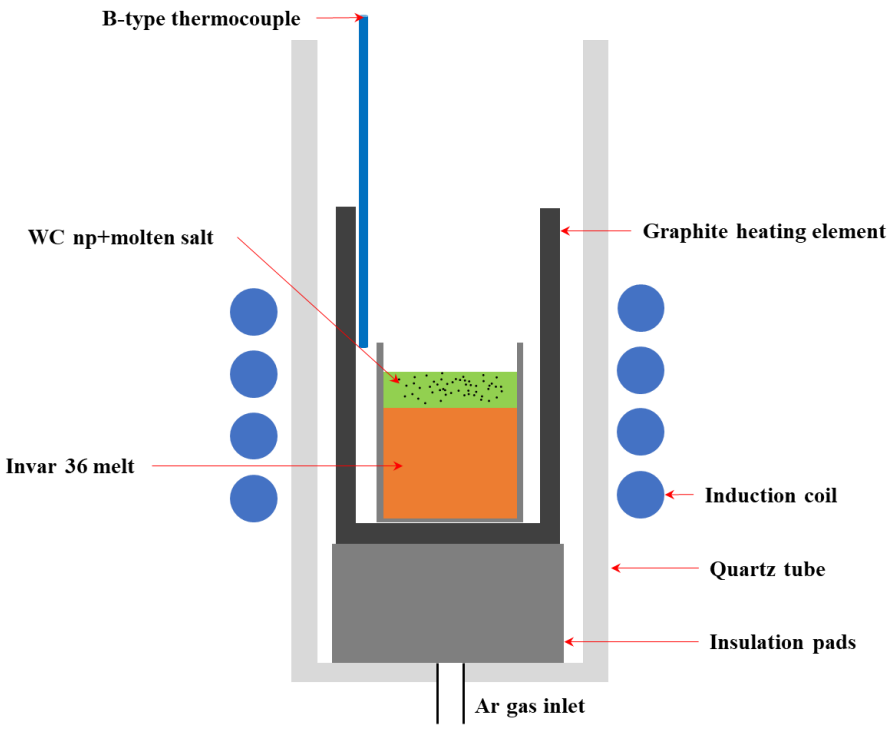

Figure 3.1: Schematic of the molten salt assisted WC incorporation.

In the powder metallurgy method, Invar powder (325 mesh) was first blended with 10 vol.% WC nanoparticles, later referred to as “Invar-10WC”. A small quantity of acetone was then introduced to the powder mixture to create a slurry. The slurry was treated in an ultrasonic bath for 10 minutes in order to break apart the WC clusters. The acetone was subsequently evaporated at 60 °C. The dried powder was cold compacted in a 2.5 cm diameter stainless steel mold at 400 MPa of pressure and was subjected to a pressureless sintering for 20 minutes at 1300 °C, under 1 atm argon protection, in an induction furnace. The sintered ingots were hot forged at 1200 °C into about 2 mm thick sheets and then cold rolled by 25% thickness reduction to 1.5 mm thick sheets.

Tensile bars were cut using electrical discharge machining (EDM). The tensile bars had a 10 mm × 4 mm × 1.5 mm (L × W × T) gage section. Prior to testing, a portion of the tensile bars were annealed at 1000 °C for 1 hour and the rest were left as-rolled. The tensile tests were

conducted on an Instron universal testing system equipped with a 10 kN load cell and a standard video extensometer. The tensile strain rate was 1×10^{-3}/s. CTE measurement was conducted using ASTM E228 method in helium atmosphere from room temperature to 370 °C. Prior to the measurement, the CTE samples were annealed at 1000 °C for 1 hour. For comparison purpose, the CTE of unreinforced Invar alloy, prepared using the same method, was also measured.

3.3. Results

3.3.1. Microstructure of Invar-5WC produced by molten salt-assisted incorporation

The microstructure of as cast Invar-5WC produced by molten salt-assisted incorporation is shown in Figure 3.2. Invar 36 is a solid solution alloy that does not naturally contain any secondary phase. The as cast microstructure is consisted of a distinct phase with light contrast within the matrix with dark contrast. The light phase has a rod-like morphology (Figure 3.2 inset) and is significantly enriched in W by EDS analysis, which is a clear indication that WC nanoparticles were dissolved in the molten Invar and then precipitated out during solidification due to the poor solubility of W in solid Fe-Ni. Despite the incorporation being carried out at a temperature (1430 ˚C) only slightly above the melting point (1427 ˚C), the WC nanoparticles fully dissolved. To this end, the Invar-5WC sample has no further value for hot and cold working, as it already lost the initially intended features from WC nanoparticles.

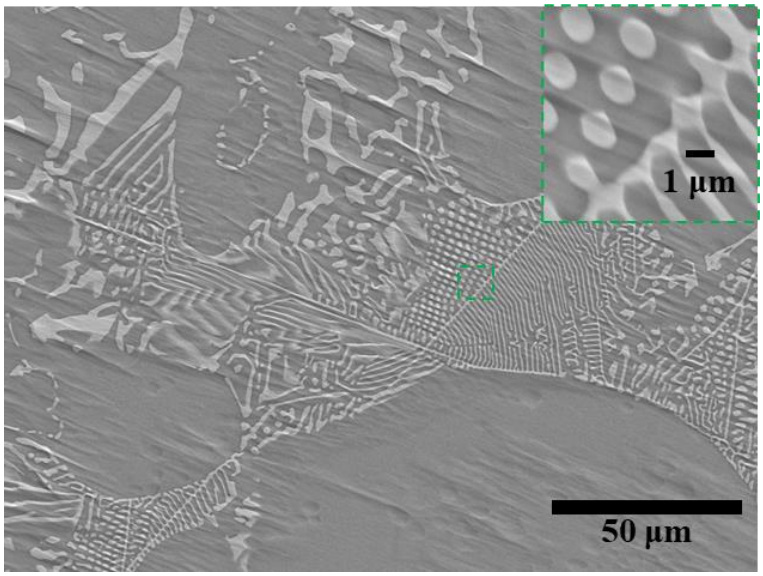

Figure 3.2: SEM micrograph of as cast Invar-5WC produced by molten salt-assisted incorporation. Inset: high magnification view on selected area.

3.3.2. Microstructure of Invar-10WC produced by powder metallurgy

The microstructure of as-sintered Invar-10WC sample is shown in Figure 3.3 (a). In the Invar matrix, WC nanoparticles are distributed in pseudo-clusters, due to the lack of ball milling during powder preparation. However, within the pseudo-clusters, the WC nanoparticles are not sintered with each other (Figure 3.3 (a) inset). The as-sintered sample also has numerous large pores and a region of poor sintering quality. The microstructure of an as-forged Invar-10WC sample is shown in Figure 3.3 (b). Compared to the as-sintered sample, the forging process is not able to alter the WC nanoparticle distribution in the Invar matrix. However, the forging process is effective in removing residual pores and breaking large WC nanoparticle pseudo-clusters into smaller ones. The relative density of the as-forged samples is around 99.3%, as determined by the Archimedes method, indicating the significant densification effect brought by the forging process.

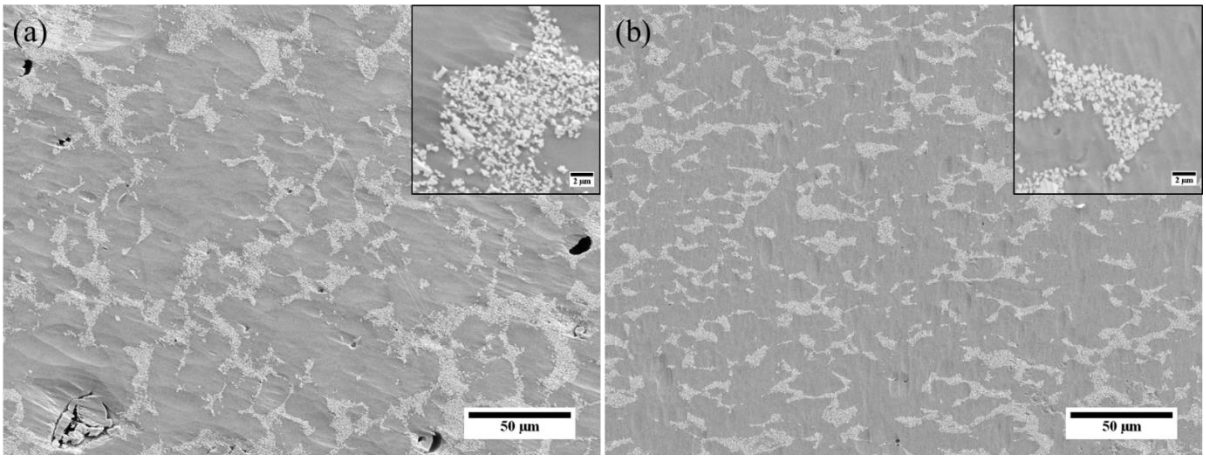

Figure 3.3: SEM micrograph of Invar-10WC sample sintered at 1300 °C. (a) as-sintered; (b)as-forged. The scale bar on the insets is 2 µm.

3.3.3. Mechanical properties and CTE of Invar-10WC samples

Figure 3.4(a) shows the typical stress-strain curves of annealed and cold rolled Invar-10WC samples. The annealed sample has a tensile strength of 800 MPa and an elongation of 22.7%. After cold rolling of 25% thickness reduction, a tensile strength of 1050 MPa is obtained, 31% higher than that of the annealed sample. The cold rolled sample has an elongation of 4.5%. Figure 3.4 (b) shows the CTE vs. temperature curves of the Invar-10WC sample and the pure Invar sample as a control, herein named "Invar-0WC". The CTE, α_{mean}, at any given temperature is given by Eqn. 19,

$$\alpha_{mean} = \frac{\frac{L_T - L_0}{L_0}}{T - T_0} \qquad \text{Eqn. 19}$$

where L_T is the length at temperature T, L_0 is the length at the starting temperature, and T_0 is the starting temperature. The CTE value is 2.61×10^{-6}/°C for the Invar-10WC sample and 1.65×10^{-6}/°C for the Invar-0WC sample, in the temperature range of 20 to 100 °C.

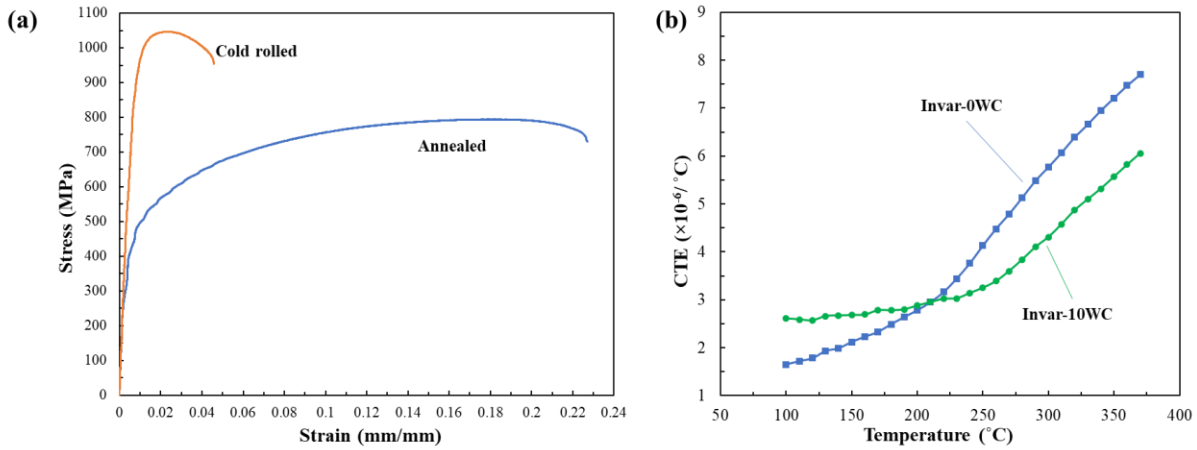

Figure 3.4: (a) Typical stress-strain curves of annealed and cold rolled (25% thickness reduction) Invar-10WC samples. (b) CTE vs. temperature curves of Invar-10WC (●) sample and control sample (■).

The property combination of UTS and CTE of the Invar-10WC sample is plotted in an Ashby chart in comparison with other engineering alloys and high strength Invar from literature (Figure 3.5). While the mechanical strength of the Invar-10WC is slightly lower than that of Fe-Ni-Co-Ti and Fe-Ni-Co-Al type high strength Invar alloys, the CTE of the Invar-10WC is significantly lower. The outstandingly low CTE allows the Invar-10WC nanocomposite to occupy a unique property space on the Ashby chart.

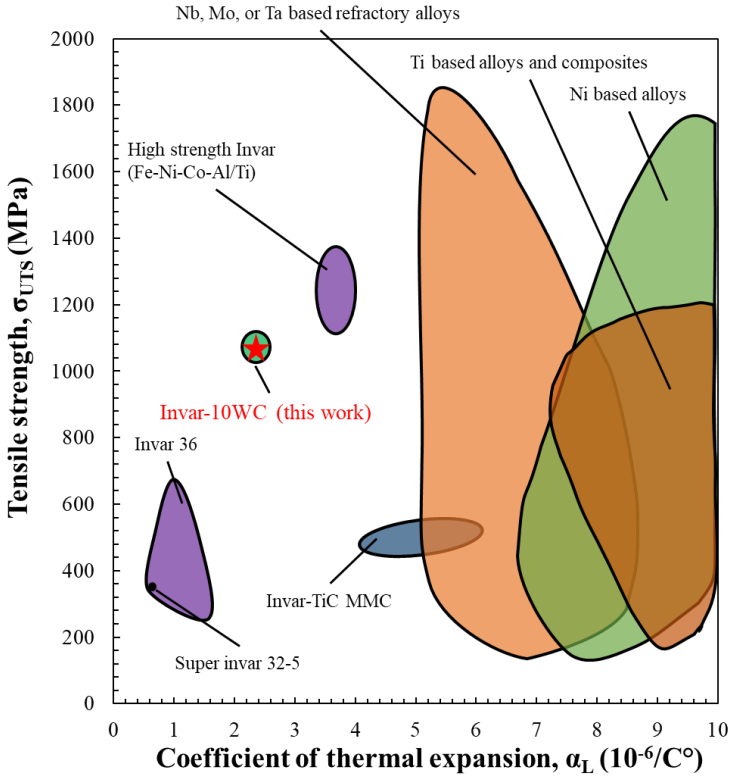

Figure 3.5: Ashby plot displaying the property combination of UTS vs. CTE of Invar-10WC sample.

3.4. **Discussion**

3.4.1. Microstructure of Invar-10WC

Based on the SEM micrographs (Figure 3.3), the forged Invar-10WC sample consists of a dual phase-like microstructure, in which densely packed, WC-rich clusters are randomly distributed throughout the matrix. The insets in Figure 3.3 indicate that the WC-rich clusters are well infiltrated by the matrix. This microstructure is likely the result of lack of ball milling during the powder preparation, as well as the drastic size difference between WC nanoparticles (APS 150 nm) and Invar powder (325 mesh). Literature has demonstrated that extensive ball milling processing will promote the dispersion of nanoparticles in the interior of metal powder, which, in

turn, gives rise to a uniform dispersion of nanoparticles in the matrix after sintering [14], [77]. Without ball milling, the WC nanoparticles remained at the surface of Invar powder after mixing. During sintering and forging, the WC nanoparticles had very limited mobility, hence were unable to travel into the Invar grains. In this work, forging was shown to be effective in densification, removing the sintering defects, and mechanically breaking apart large WC-rich clusters to smaller ones. A thermodynamic study in literature has demonstrated that WC has around 2 at.% solubility in Fe and Ni matrix at 1200 ˚C and will react with molten Ni and Fe to form a M_6C type alloy carbide[78]. For these reasons, upon experimentation of different sintering times and temperatures, sintering was carried out at 1300 ˚C for a relatively short duration of 20 minutes, in which no obvious growth or reaction of WC nanoparticles was observed.

3.4.2. Mechanical properties of Invar-10WC

The mechanical properties of Invar-10WC in comparison with a commercial Invar 36 alloy are summarized in Table 1. The Young's modulus of the Invar-10WC sample is in close accordance with the volumetric rule of mixture when using E_{WC}=550 GPa and E_{Invar}=140 GPa. The yield strength and tensile strength of the annealed Invar-10WC are increased by 60% and 77%, respectively, compared with the commercial alloy, while for cold rolled Invar-10WC, the values increased by 40% and 46%, respectively.

Table 1: Mechanical properties of Invar-10WC comparing with a commercial Invar 36 alloy

.	Young's modulus (GPa)	σ_y (MPa)	σ_{UTS} (MPa)	Elongation, ε
Annealed				
Invar-10WC	180	440	795	22.7%
Commercial Invar 36 [21]	140	276	448	35%
Cold rolled				
Invar-10WC	185	950	1050	4.5%
Commercial Invar 36 [21]	145	679	717	5.5%

3.4.3. Thermal expansion behavior of Invar-10WC

The CTE values of the Invar-10WC and the Invar-0WC, as a control, samples at selected temperatures are compared with a commercial Invar 36 alloy in Table 2. The Invar-0WC sample in this work exhibits slightly higher CTE value than that of the commercial alloy after the same heat treatment. This is likely the result of contamination and oxidation issues of powder metallurgical processing compared to the casting process in commercial production scale. The CTE value of the Invar-10WC sample is found to deviate slightly from the volumetric rule of mixture in the temperature range of 20-100 °C. This is likely due to the presence of some contaminants on the commercial WC nanoparticles as well as minor dissolution of WC into the Invar matrix during sintering and forging, which was not directly observed in the SEM analysis [78]. While the CTE of Invar-10WC is higher than that of unreinforced Invar-0WC from room temperature to 210 °C, a noticeable crossover between the two CTE vs. temperature curves occurs around 210 °C, above which the CTE of the composite sample is lower than that of the unreinforced sample.

Table 2: CTE of Invar-10WC, Invar-0WC, and a commercial Invar 36 alloy at selected temperature.

Temperature (°C)	**CTE, α (×10^{-6}/°C)**		
	Invar-10WC	Invar-0WC	Commercial Invar 36 [3]
100	2.61	1.65	1.50
150	2.68	2.12	2.11
260	3.39	4.48	4.18
370	6.06	7.70	7.60

Due to its hexagonal crystal structure, α-WC has two distinctive linear CTE values on its a-axis (α_a) and c-axis (α_c). The α_a, α_c, and mean linear CTE values of WC at elevated temperature are not reported in literature. The volumetric CTE, α_V, of WC at elevated temperature was reported by Reeber *et al*. It was reported that the volumetric CTE vs. temperature curve follows a logarithmic pattern, in which the CTE value grows fast from 0 to 230 °C and slows down after 230 °C, eventually reaching a plateau above 800 °C [79]. The CTE of the Invar-0WC sample follows that of commercial Invar 36, which show an increase of CTE when above its Curie temperature. The Invar-10WC sample only suffers a higher CTE value below 210 °C, but benefits from the lack of Curie point and the slow growing CTE of WC above 230 °C, which results in the overall lower CTE value of the nanocomposite sample, when compared to that of regular Invar 36 alloy.

3.5. **Conclusions**

In this work, two methods of WC nanoparticle incorporation in Invar 36 matrix were studied, intending to suppress the reaction by reducing the temperature. The molten salt assisted incorporation, which incorporates WC nanoparticles into the Invar matrix in liquid state, resulted

in the full dissolution of the WC. The second method, which incorporates WC nanoparticles into the Invar matrix through a combination of sintering and hot deformation, took place at 1300 °C, roughly 130 °C below the melting point of Invar. At this temperature, the dissolution of WC can be reasonably managed. The solid-state processed Invar-10WC sample has significantly higher tensile strength than the un-reinforced Invar. The CTE of Invar-10WC sample also benefits from the unique thermal expansion behavior of the WC phase, which results in the Invar-10WC sample having lower CTE value than the un-reinforced Invar above 210 °C.

Chapter 4. Effect of TiB2 nanoparticle addition on the solidification, microstructure, and property of Fe-Ti-B high modulus steel

In Chapter 3, the main focus of the experiment was to suppress the reactivity between WC nanoparticles and molten Fe-36Ni Invar alloy, which has a low melting point of 1427 ˚C. The reaction was reasonably managed when the processing temperature dropped to 1300 ˚C, at which point the matrix was solid. Therefore, attempting to manage the reactivity between nanoparticle and a reactive melt solely by reducing the temperature is not effective, unless the processing temperature is much lower than melting point, at which the diffusion is limited in solid.

In this chapter, a different method of suppressing the reactivity between nanoparticles and a reactive melt is studied. As reviewed in section 2.2.3.2. , Fe and TiB_2 form a pseudo-binary system with a eutectic point near 6.3 at.% TiB_2 at 1310 ˚C. Therefore, if TiB_2 nanoparticles are to be added into molten pure Fe, they will be quickly dissolved. However, if a small amount of TiB_2 nanoparticles are added to a Fe-6.5% TiB_2 eutectic melt, then the extra TiB_2 will push the overall composition into the liquid+TiB_2 zone as shown in Figure 2.19. These extra nanoparticles could survive in the melt for a short time before solidification. In this method, the reactivity is suppressed chemically, by the existence of dissolved TiB_2 in the melt.

4.1. Introduction to Fe-Ti-B high modulus steel and manufacturing challenges

Materials lightweighting is a longstanding goal for material design to improve the performance of machines and the energy efficiency of transportation systems. Steel is the most important structural alloy for human society. It provides the widest range of strength and ductility combinations due to its versatile alloying strategy as well as its highly tunable microstructure by

thermomechanical processing. However, due to the relatively high density (ρ) of iron (Fe), the specific strength (YS/ρ and UTS/ρ) and specific stiffness (E/ρ) of steel are often at a disadvantage when compared with other light alloys such as Al, Ti, and Mg [65]. Through advanced alloying and microstructure engineering, the specific strength of steels can be increased significantly[80],[81],[82], which have the specific strength comparable to or exceeding that of advanced Al[83], Ti[84], or Mg[10], [85] alloys. However, the Young's modulus of steels remains at about 190 to 210 GPa[8], [86], [87], thus a specific stiffness roughly 24-26 $GPa \cdot cm^3 \cdot g^{-1}$, consequently lacking sufficient stiffness against bending, buckling, and deflection in lightweight thin-walled components[8], [62], [88]. Increasing the specific strength and specific stiffness of steels simultaneously can be achieved through incorporating stiff and light ceramic phases, such as titanium diboride (TiB_2) with a high specific stiffness (82-122 $GPa \cdot cm^3 \cdot g^{-1}$)[89]. Unfortunately, the promise of Fe-TiB_2 based composites, known as High Modulus Steels (HMS), faces a fundamental dilemma between achieving enhanced mechanical properties and manufacturing for mainstream applications. During conventional molten metal processing (near-equilibrium solidification), the brittle TiB_2 particles tend to grow large in size out of the Fe-Ti-B melts, which degrades its strengthening effect and ductility. Rapid solidification techniques, such as spray forming, have shown to produce TiB_2 submicron/nano-particles with good strengthening while maintaining ductility[8]. However, these non-equilibrium solidification methods are not conducive to high-volume production of steels.

In this study, a small amount of *ex situ* TiB_2 nanoparticles was added via a molten salt mixture to the Fe-Ti-B melt of an eutectic Fe-6.3 at.% TiB_2 composition, in which the process is referred to as "nano-treat (NT)" herein, and then solidified slowly at a cooling rate less than 5 K/s (near equilibrium solidification) to enable potential mass production. The as cast Fe-TiB_2 HMS

(High Modulus Steels) by this novel nano-treating method has higher strength and similar stiffness compared to the HMS produced by rapid solidification (non-equilibrium solidification). The nano-treated alloy has a significantly finer TiB_2 particle size, which is unusual when considering its production under such a slow solidification rate (less than 5 K/s). More surprisingly, ultrafine Fe_2B lamellas appear in the ferrite matrix. The Fe_2B phase is often considered to be a detrimental phase and avoided in HMS, due to its embrittlement effect and a comparatively low specific stiffness (34.6 $GPa \cdot cm^3 \cdot g^{-1}$) as well as weak strengthening effect [90], [91]. Hence, in our initial experimental design, we followed the traditional wisdom to suppress the formation of Fe_2B by adding an excessive amount of Ti [9], [92]–[94]. However, after nano-treating, we discovered that an ultrafine Fe_2B phase persists to exist despite the excess Ti. It even serves as the main strengthening phase for the new Fe-Ti-B based HMS, while the TiB_2 phase contributes to the stiffness enhancement. Detailed microstructural, thermal analysis, and phase diagram simulation studies reveal that the *ex situ* TiB_2 nanoparticles induced unexpected solidification pathways for unusual phase formation that results in fine TiB_2 particles with embedded nanoscale Fe_2Ti, which serves like a sponge to absorb excess Ti in the melt, leaving Ti-poor regions between the primary TiB_2 clusters to allow the ultrafine Fe_2B lamellas to form. Upon simple hot working, the ultrafine Fe_2B lamellas evolve to nano-sized Fe_2B particles to provide good strengthening in the HMS.

4.2. Experimental procedure

4.2.1. Ingot preparation

The starting material of this work was Fe-5.53 Ti-2.29 wt.%B, herein named “reference HMS” (RHMS), which is corresponding to the near-eutectic composition of 7.35 wt.%TiB_2, ~ 12 vol.%, in Fe matrix at a relatively low liquidus temperature of 1400˚C[62], [88]. The Ti content is 0.51 wt.% in excess, in order to suppress the formation of Fe_2B during initial casting. The ingot

was made by melting high purity Fe granules, Ti rods, and Fe-20 wt.%B master alloy granules in an induction furnace under argon (Ar) atmosphere. The slag at the top of the ingot was trimmed off and the ingot was remelted, placed upside down, under the same melting conditions to ensure homogeneous distribution of the charge.

The naming convention and abbreviation of the samples in this work are summarized in Table 3.

Table 3: Sample names and corresponding abbreviations.

Sample Name	Name abbreviation	Sample design
Main samples		
Reference high modulus steel	RHMS	As cast Fe-5.87 Ti-2.53 wt.%B
Hot worked reference high modulus steel	Hot worked RHMS	Hot worked Fe-5.87 Ti-2.53 wt.%B
Nano-treated high modulus steel	NT HMS	Nano-treated Fe-5.87 Ti-2.53 wt.%B with 1.5 wt.% TiB_2 nanoparticles added
Hot worked nano-treated high modulus steel	Hot worked NT HMS	Hot worked NT HMS
Control samples		
"Micro-treated" high modulus steel	Micro-treated HMS	RHMS with 1.5 wt.% micro-TiB_2 particles incorporated
"Ribbon-treated" high modulus steel	Ribbon-treated HMS	RHMS with 25 wt.% of Fe-9.22 Ti-3.79 wt.%B melt spun ribbons incorporated

4.2.2. Nano-treating (NT) of RHMS

TiB_2 nanoparticles were synthesized in-house using previously established magnesiothermic reduction method[95], [96]. Two parts (by weight) of the synthesized TiB_2 nanoparticles were milled in a mortar with twenty parts of anhydrous borax ($Na_2B_4O_7$) and one part of calcium fluoride (CaF_2). The resulting mixture consisted of roughly 5 vol.% TiB_2 nanoparticles and 95 vol.% salt.

The RHMS sample was placed in an alumina crucible and melted at 1410 ˚C in an induction furnace, while the salt mixture was gradually fed onto the melt surface. The experimental setup is similar to that of in section 3.3.1. , as shown in Figure 3.1. By design, roughly 1.5 wt.% of the TiB_2 nanoparticles would be incorporated into the RHMS. The actual percentage of incorporated TiB_2 nanoparticles was later determined by inductively coupled plasma atomic emission spectroscopy (ICP-AES). After nanoparticle feeding, the melt was held at the same temperature for an additional 5 minutes, and furnace cooled to 1100 ˚C, with cooling rate less than 5 K/s (near equilibrium solidification), followed by air cooling to room temperature. This sample is named "NT HMS".

Two control experiments were designed to confirm the effect of nano-treating. In the first control experiment, the same procedure was used to incorporate TiB_2 microparticles (325 mesh) into RHMS. This sample is named micro-treated HMS. In the second control experiment, we first cast an ingot of Fe-9.22 Ti-3.79 wt.%B, which is corresponding to ~ 19.5 vol.% TiB_2 in Fe matrix, using the same ingredient for each element. The ingot was then remelted in a melt spinning equipment and spun into thin ribbons. The resulting TiB_2 particle size was less than 50 nm, as shown in Figure 4.1. The ribbons were added back into the melt of RHMS at 1410 ˚C by a one to three weight ratio, then cooled down using the same cooling profile. This procedure was designed to introduce roughly 1 wt.% of TiB_2 nanoparticles into RHMS without the influence of molten salt. This sample was named ribbon-treated HMS.

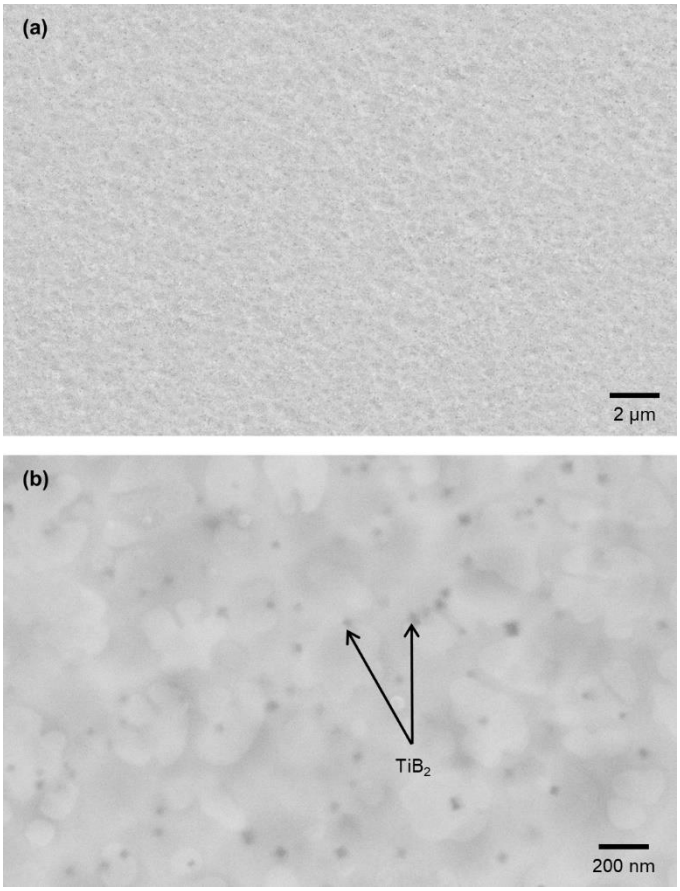

Figure 4.1: (a)SEM micrograph of Fe-9.22Ti-3.79B melt spun ribbon, (b)High magnification micrograph.

4.2.3. Hot working of nano-treated HMS

The residual salt on the as-cast nano-treated HMS was mechanically removed by a belt sander. The ingot was then forged at 1050 ˚C to a rectangular bar using a hydraulic forge press. The forged sample was furnace cooled to relieve residual stress, and then polished to remove scale. The hot worked sample was named “hot worked NT HMS”. As a comparison, the RHMS was processed using the same procedure, which was named “hot worked RHMS”.

4.2.4. Vickers hardness and tensile tests

Vickers hardness was measured on metallurgically polished samples using 0.5 kg force and 10 s dwell time. Hot worked RHMS and hot worked NT HMS sample bars were cut to tensile specimen using a wire EDM machine and were further polished to remove scale. The tensile specimen had a gage section of 10 × 4 × 1.5 mm (L × W × T). The tensile tests were conducted on an Instron universal testing system equipped with a 10 kN load cell and a Standard Video Extensometer (SVE). The nominal tensile strain rate was 1 × 10−3/s.

4.2.5. Microstructure characterization, chemical analysis and thermal analysis

Microstructure characterization was carried out by scanning electron microscopy (SEM; Zeiss Supra 40-VP), electron backscatter diffraction (EBSD; Zeiss ULTRA Plus), and scanning transmission electron microscope (STEM; Jeol JEM-ARM300F). EBSD analyses were performed on the NT HMS and hot worked NT HMS samples. STEM analyses were performed on the NT HMS and RHMS samples. The chemical composition of each sample was measured by ICP-AES and summarized in Table 4.

The solid-state phase transformation temperatures were determined using an NETZSCH DSC 404 C differential scanning calorimeter (DSC). The DSC was calibrated (temperature correction) by melting high-purity Ag, Cu and Ni. The DSC samples were cut by wire electrical discharge machining (WEDM) to obtain cylindrical specimens (Φ3 mm × 3 mm) for DSC. The heating rate of the DSC tests are 4 ˚C/min.

Table 4: Sample chemical composition measured by ICP-AES.

Sample name	Designed composition (wt.%)	Designed TiB_2 content (wt.%)	Designed weight percentage of Ti in excess	Actual composition (wt.%)	Actual weight percentage of Ti in excess	Actual TiB_2 content (wt.%)
RHMS	Fe-5.87Ti-2.53B	8.12%	0.29%	Fe-5.53Ti-2.29B	0.51%	7.35%
NT HMS	Fe-6.90Ti-3.00B	9.63%	0.28%	Fe-5.91Ti-2.54B	0.31%	8.15%
Micro-treated HMS	Fe-6.90Ti-3.00B	9.63%	0.28%	Fe-6.22Ti-2.64B	0.41%	8.48%
Ribbon-treated HMS	Fe-6.71Ti-2.85B	9.15%	0.43%	Fe-6.28Ti-2.57B	0.66%	8.25%

4.3. **Results**

4.3.1. SEM and EBSD characterization

The microstructural comparison between as-cast RHMS sample and nano-treated HMS sample (NT HMS) is shown in Figure 4.2 (a) and (b), in which a significant microstructural refinement effect can be observed at low magnification. The general microstructure of nano-treated HMS (NT HMS) in as cast state and after hot working is shown in Figure 4.2 (c) and (d). EBSD was used to identify the phases present in the two samples. The as cast NT HMS consists of three distinctive microstructural components: branch-like TiB_2 eutectic colonies, Fe_2B lamella between the TiB_2 colonies (Figure 4.2 (c) and (e)), and Fe matrix. Upon hot working, the sample retained the same three phases (Figure 4.2 (f)), however, the Fe_2B lamella was broken down to fine Fe_2B particles around 200nm in size (Figure 4.2 (d) and inset). The primary TiB_2 phase had also altered from a branch-like morphology to a more equiaxed morphology (Figure 4.2 (f)).

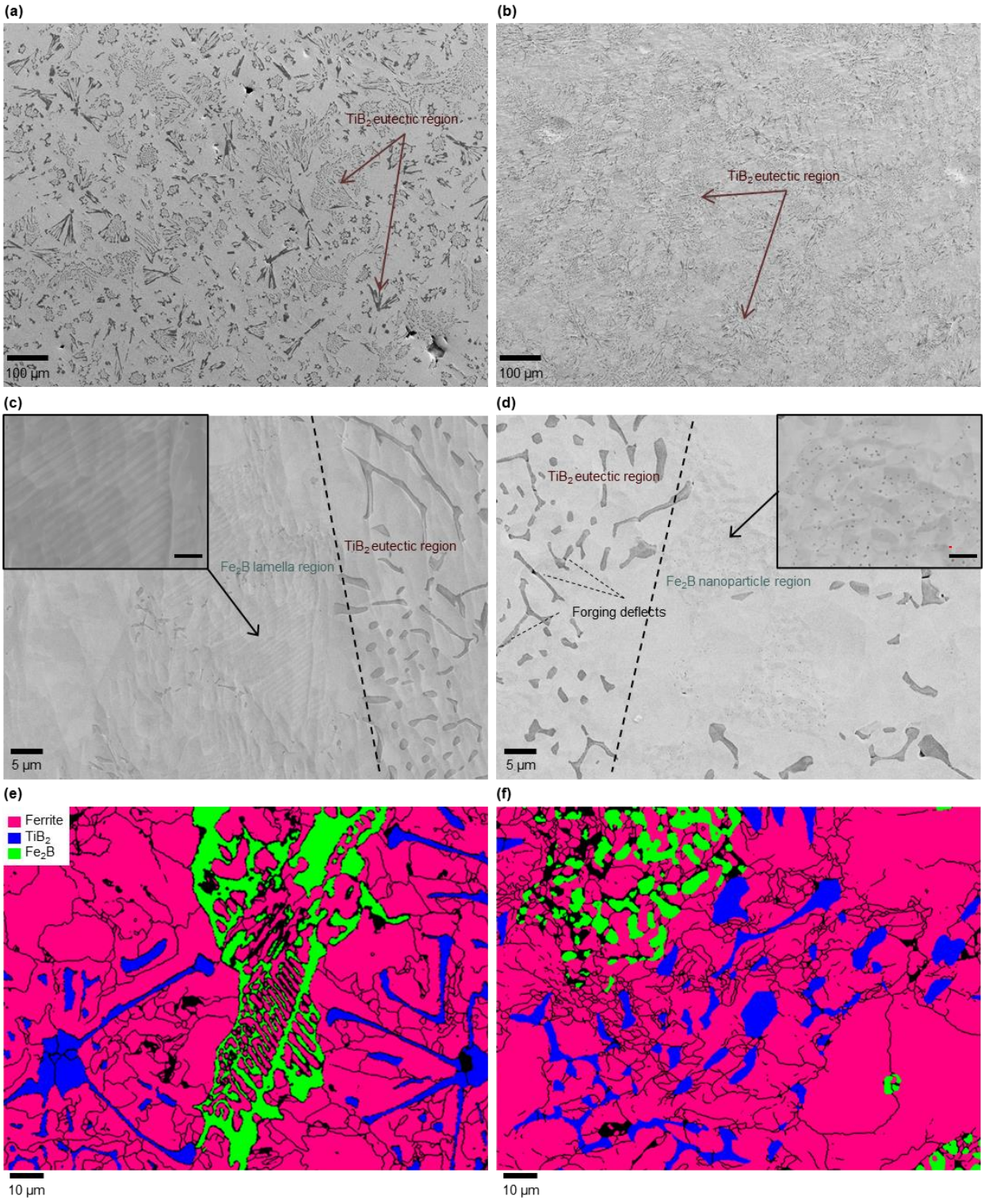

Figure 4.2: (a) Low magnification SEM micrograph of RHMS sample. (b) Low magnification SEM micrograph of NT HMS sample. (c) SEM micrograph of NT HMS sample; inset: zoomed-

in view of the Fe_2B lamella, scale bar is 2 μm. (d) SEM micrograph of hot worked NT HMS sample; inset: zoomed-in view of the precipitated Fe_2B due to hot working, scale bar is 2 μm, red dot represents 200 nm. (e) EBSD phase mapping of NT HMS displaying the position of TiB_2 eutectic colonies and Fe_2B lamellas. (f) EBSD phase mapping of hot worked NT HMS displaying the changed TiB_2 and Fe_2B morphology after hot working, where the black lines denote high-angle boundaries.

To verify the effect of TiB_2 nanoparticles, two control experiments were conducted. In the first control experiment, same procedure was used to incorporate 325 mesh TiB_2 micro-powders (APS~40μm) into reference HMS (RHMS). The resulting "micro-treated" HMS sample had almost identical microstructure with RHMS, as shown in Figure 4.3 (b). As such, the effect of molten salt and higher overall TiB_2 concentration can be excluded.

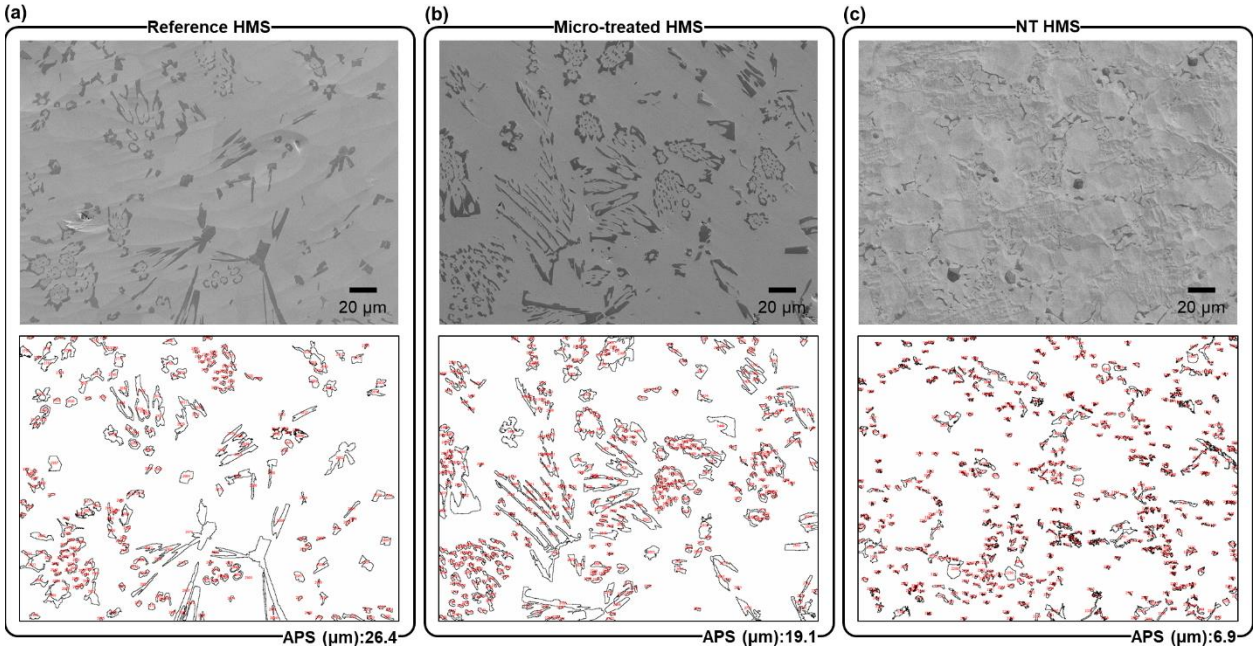

Figure 4.3: Representative SEM micrograph and its skeletonized TiB_2 particle image of (a)RHMS, (b)Micro-treated HMS, and (c)NT HMS. The APS are 26.4, 19.1, and 6.9 μm, respectively.

To confirm the nanoparticle induced change, melt spun ribbons containing fine TiB_2 nanoparticles (APS~50 nm) were added into RHMS melt without molten salt assistance. Similar Fe_2B lamella was observed in the ribbon-treated sample, referred to as ribbon-treated HMS herein, as shown in Figure 4.4 (a) and (c), hence confirming that the formation of Fe_2B lamella was induced by TiB_2 nanoparticles.

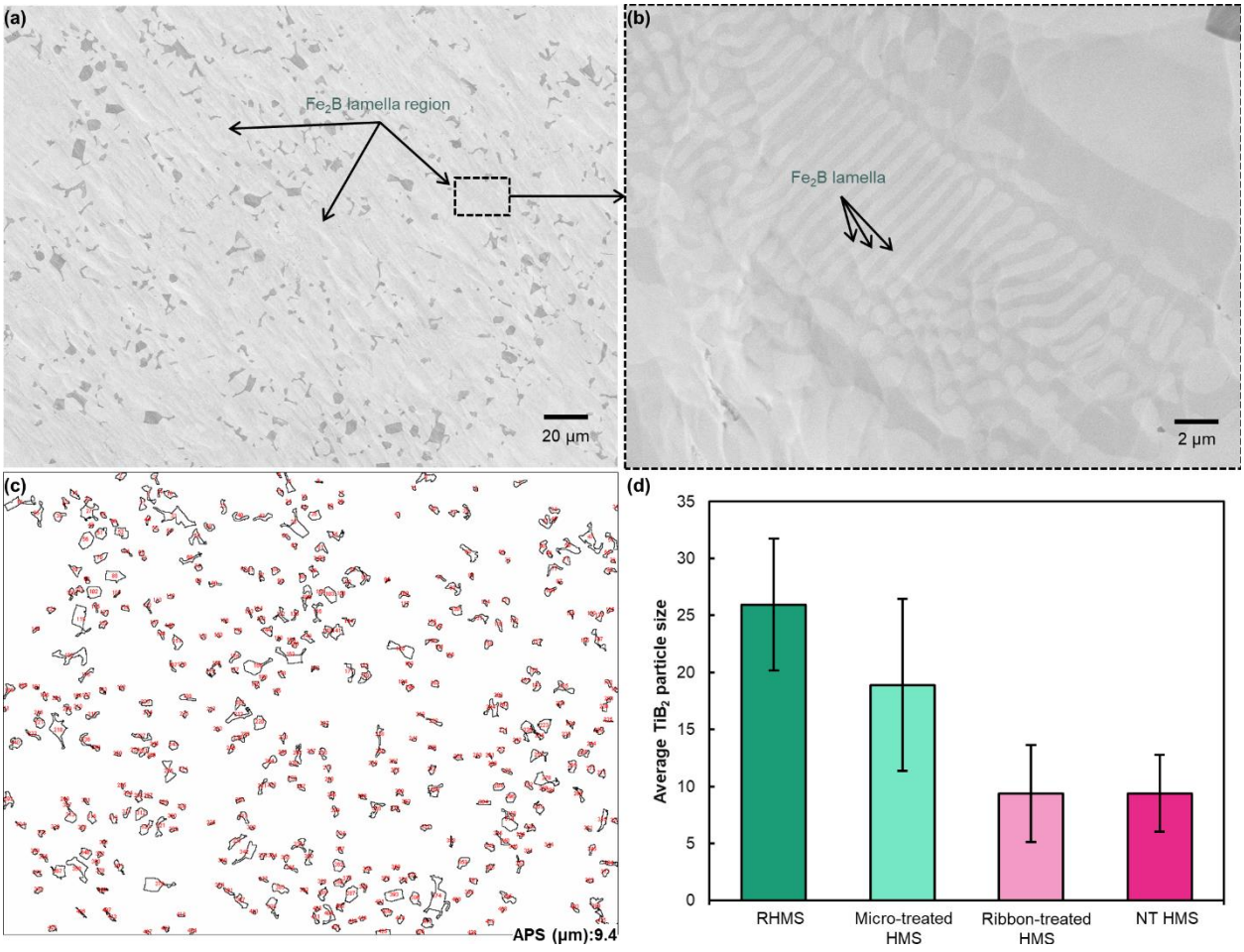

Figure 4.4: (a)SEM micrograph of ribbon-treated HMS. (b)Zoomed-in view of the selected area in (a). (c)Skeletonized image of (a) for TiB_2 particle size analysis, the APS is 9.4 μm. (d)Histogram of TiB_2 particle size in various samples. The ribbon-treating and nano-treating process resulted in roughly the same particle size.

4.3.2. Chemical analysis

The chemical analysis of the control samples, namely micro-treated HMS and ribbon-treated HMS are shown in Table 4. Comparing to the TiB_2 nanoparticle incorporation by molten salt, the TiB_2 microparticles were incorporated at a higher efficiency, roughly 70% of the designed 1.5 wt.%. The resulting composition of micro-treated HMS is hypereutectic (8.48 wt.% TiB_2) with 0.41 wt.% Ti in excess. The TiB_2 nanoparticle incorporation by the addition of 25 wt.% melt-spun ribbons had the highest efficiency, at 90% of the designed value. The resulting composition of ribbon-treated HMS is hyper-eutectic (8.25 wt.% TiB_2) with 0.66 wt.% Ti in excess. In all three samples (NT, micro-treated, and ribbon-treated HMS), the overall compositions are Ti-rich by 0.31, 0.41, and 0.66 wt.%, respectively. Therefore, the formation of Fe_2B phase was not predicted since TiB_2 is thermodynamically more favored than Fe_2B when Ti is sufficient[62], [88], [97]. It is thus surprising to observe the persistent formation of Fe_2B when TiB_2 nanoparticles were involved (NT and ribbon-treated HMS), suggesting a new mechanism of Fe_2B formation.

4.3.3. Thermal analysis

The thermal analysis by differential scanning calorimetry (DSC) analysis reveals that the Fe_2B phase dissolves at around 1155 ˚C in both NT HMS and hot worked NT HMS sample, as shown in Figure 4.5. This temperature is close to the dissolution temperature of Fe_2B phase in Fe-B binary system [98]. Therefore, the morphology evolution of Fe_2B lamella during hot working was a combined result of mechanical shearing and dissolution-precipitation. However, this observation is unable to account for why Fe_2B persisted to exist after hot working and the subsequent thermal annealing by furnace cooling in an overall composition that was Ti-rich.

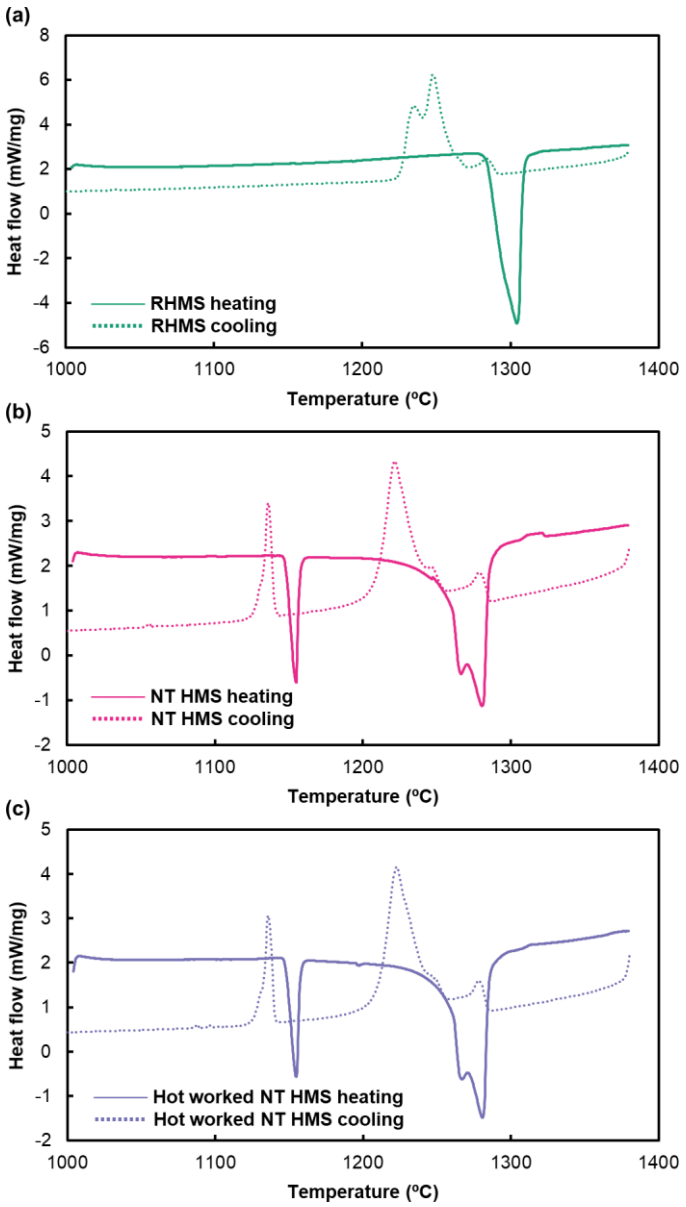

Figure 4.5: DSC analyses of (a) RHMS, (b) NT HMS, and (c) hot worked NT HMS.

4.3.4. STEM characterization

To understand the Ti distribution and its relationship with the non-equilibrium Fe_2B phase, samples of roughly 15 × 5 × 0.2 μm (L × W × T) in size were prepared using focused ion beam (FIB) and observed by scanning transmission electron microscope (STEM). These samples contained at least one TiB_2 particle, the surrounding Fe matrix, and, in the case of NT HMS sample,

Fe_2B lamella in close proximity, as shown in Figure 4.6 (a) and (e). Energy-dispersive x-ray spectroscopy (EDS) was performed in high-angle annular dark-field (HAADF) mode to map the Ti distribution. In RHMS sample, roughly 2 wt.% Ti can be detected in the Fe matrix (Figure 4.6 (e)), which is consistent with the literature[9]. In contrast, no Ti was detected in solid solution with Fe matrix in the NT HMS sample, therefore, the Fe matrix was Ti-poor, allowing the extra B to form Fe_2B (Figure 4.6 (a)). High magnification examination revealed that numerous Fe-rich needle-like precipitates were embedded in the TiB_2 particle (Figure 4.6 (b)). These needle-like precipitates were later identified as Fe_2Ti based on their diffraction pattern (Figure 4.6 (c)). The (101) plane of TiB_2 (d=2.12 Å) and (112) plane of Fe_2Ti (d=2.10 Å) formed a coherent interface with mismatch, δ, less than 1% (Figure 4.6 (d)). In comparison, the TiB_2 particle found in RHMS sample appeared to be a single-phased TiB_2 that contains no Fe_2Ti precipitates (Figure 4.6 (f)and (g)).

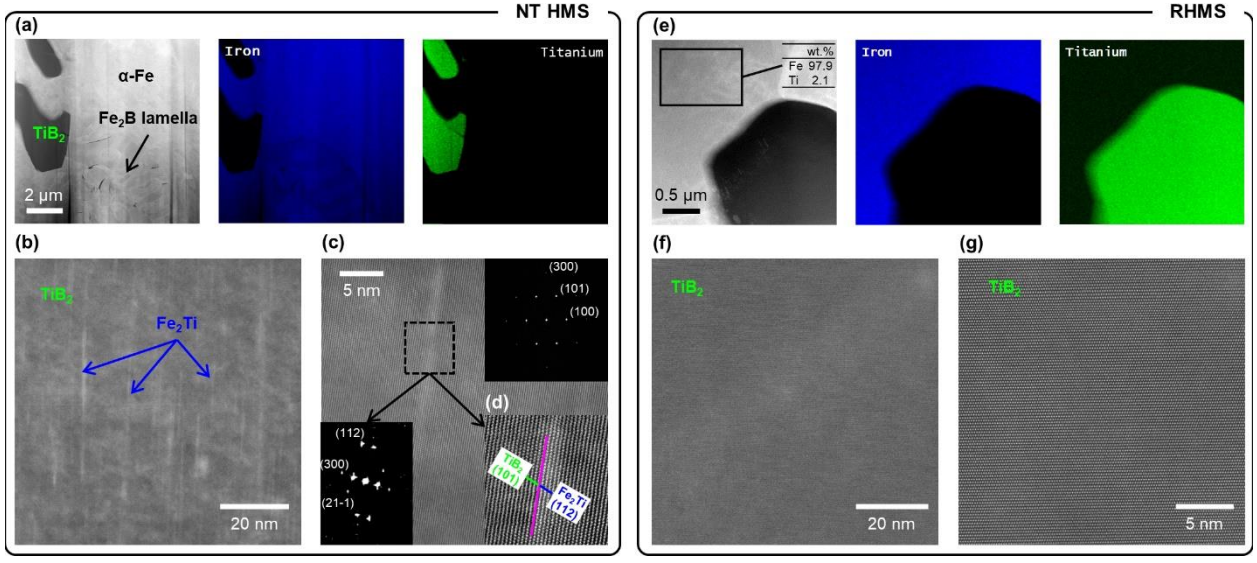

Figure 4.6: High-angle annular dark-field (HAADF) scanning transmission electron microscope (STEM) micrographs of NT HMS: (a) Dark-field (DF) STEM micrograph with corresponding EDS elemental maps for Fe and Ti; (b) DF STEM micrograph taken inside the TiB_2 particle;

bright needles highlighted by blue arrows are Fe_2Ti intermetallic. (c) DF STEM micrograph showing one Fe_2Ti needle in TiB_2 matrix, and insets showing the diffraction pattern of the corresponding TiB_2 and Fe_2Ti phase; (d) Close-up view of highlighted area in (c) showing the interface between $(101)_{TiB2}$ and $(112)_{Fe2Ti}$. HAADF-STEM micrographs of RHMS: (e) DF STEM micrograph with corresponding elemental maps for Fe and Ti. Quantitative analysis of the elemental composition in highlighted area reveals 2.1 wt.% Ti in Fe solid solution. (f) and (g)DF STEM micrograph taken inside the TiB_2 particle in (a), no Fe_2Ti is found. All of the Miller indices (hkl) are transformed from Miller-Bravais indices (hkil) for hexagonal lattice for simplicity.

4.4. Discussion

4.4.1. Mechanism of Fe_2B formation

Fe-Ti isopleth sections at different B concentration are calculated using Thermo-Calc software. The solidification path of RHMS sample is similar to that of a classic binary system, as shown in Figure 4.7 (d), where the green path leads to the formation of the α-Fe matrix and the blue path leads to the formation of TiB_2 and Fe eutectic structure. In DSC analysis, as shown in Figure 4.5 (a), the RHMS sample has a double peak during solidification, which is consistent which the calculated Fe-Ti isopleth section (Figure 4.7 (d)) where a narrow liquid+α-Fe region is predicted to exist.

In the case of NT HMS sample, surprisingly, we observed two additional phases, namely Fe_2Ti that are embedded within the primary TiB_2 particles (Figure 4.6 (b)), and Fe_2B that formed between the TiB_2 clusters. To understand such a phenomenon, we first examine the calculated Fe-Ti isopleth section at 2.54 wt.% B, as shown in Figure 4.7 (e), which indicates that the Fe_2Ti phase will only form at above 10 wt.% Ti, far exceeding the measured 5.91 wt.% Ti in the NTHMS

sample. Therefore, in order for the Fe_2Ti phase to form, the solidification must take an unusual path that result in significant enrichment of Ti, as shown by the dashed blue line in Figure 4.7 (f), and depletion of Ti, as shown by the dashed green line, to compensate the overall Ti concentration. However, such an unusual solidification path needs to transverse through several inner phase boundaries, which would be in violation of established phase diagram rules [99]. For reference in a regular hypereutectic HMS that is compositionally similar to NT HMS, the solidification behavior is well explained by the literature.[93] The growth of TiB_2 phase has three stages: *(i)* the formation of primary TiB_2 particles with their surrounding Fe phase, called "halo Fe" (Figure 4.7.(a)-2); *(ii)* the formation of eutectic TiB_2 on either primary TiB_2 or on halo Fe and trapping liquid during the process (Figure 4.7 (a)-3,4); and *(iii)* final eutectic TiB_2 forms in the entrapped liquid zones (Figure 4.7 (a)-5)[93].

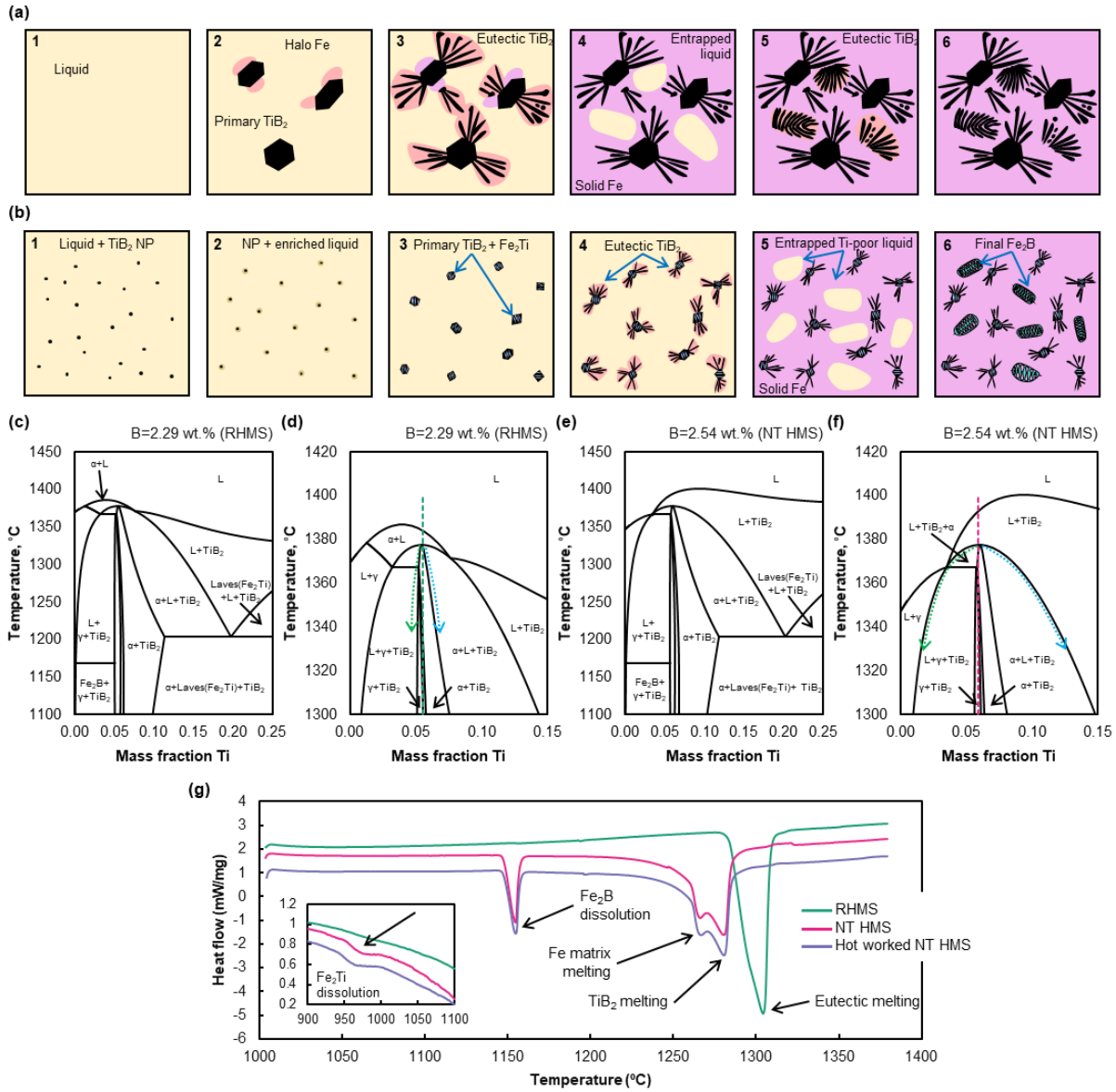

Figure 4.7: Schematic illustrations of (a) phase evolution during solidification of a regular hypereutectic HMS sample, reproduced based on literature [93], and (b) NT HMS sample. (c) Calculated Fe-Ti isopleth section at 2.29 wt.% B, and (d) close-up view of (c) near the melting point, the dashed green line indicates the measured Ti concentration in RHMS sample. (e) Calculated Fe-Ti isopleth section at 2.54 wt.% B, and (d) close-up view of (f) near the melting point, the dashed magenta line indicates the measured Ti concentration in NT HMS sample. (g)

DSC heating curves for RHMS, NT HMS, and hot worked NT HMS sample from 1000 to 1380 ˚C, inset: heating curves from 900 to 1050 ˚C.

To this end, these results suggest a new mechanism that allows a novel phase formation through an unconventional solidification path, while not violating established phase diagram rules for near-equilibrium solidification. When the TiB_2 nanoparticles are introduced to the melt with eutectic composition, a portion of them will be dissolved, pushing the liquid composition towards oversaturation, resulting in a dynamic balance of the mass exchange between the solid TiB_2 nanoparticles and their surrounding liquid environment. As such, the liquid composition near the nanoparticles will be more enriched than the liquid melt, as shown in Figure 4.7 (b)-2. As solidification proceeds, the enriched liquid and the nanoparticles will form Fe_2Ti and TiB_2 precipitates (Figure 4.7 (b)-3), which serve as nucleation sites for eutectic TiB_2 colonies (Figure 4.7 (b)-4). Due to the enrichment of solutes near the nanoparticles, the matrix melt is expected to have slightly depleted Ti content, which results in the formation of Fe_2B in the last solidifying liquid zones (Figure 4.7 (b)-5, 6). This is consistent with the DSC analysis result shown in Figure 4.7 (g), in which the peak around 960 ˚C is attributed to the dissolution of Fe_2Ti, while the peak around 1150 ˚C is attributed to the dissolution of Fe_2B. This solidification mechanism allows the coexistence of the blue and green paths in Figure 4.7 (f) without violating phase diagram rules, due to the presence of two distinct liquid compositions, one near the nanoparticles and the other being the matrix liquid melt.

In our previous research, a similar solidification phenomenon was observed, but not fully understood at the time, in a Mg-6 wt.% Zn alloy with the addition of 3 wt.% SiC nanoparticles [100]. In that work, the solidification path will result in the formation of Mg_7Zn_3 phase, which then decomposes to form Mg_2Zn_3 or MgZn in a Mg matrix. However, with addition of SiC

nanoparticles induced the formation of $MgZn_2$, a phase that lies far away from the equilibrium composition. The formation of $MgZn_2$ requires a large enrichment of Zn, far beyond 6%, as shown by the orange dashed line in the phase diagram (Figure 4.8). We speculate that a high concentration of Zn was segregated at the SiC-liquid interface, which enabled the formation of the $MgZn_2$ around the SiC nanoparticles. This hypothesis points to the presence of an enriched liquid layer surrounding the nanoparticles prior to solidification, effectively creating two distinct liquid compositions, that solidify in separate pathways, which is consistent to the mechanism we discovered in our current work. Essentially, we have two different solidification paths by two liquid zones occurring simultaneously.

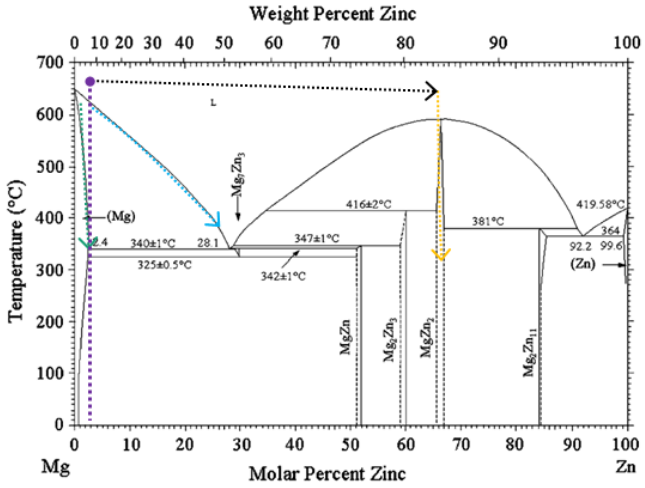

Figure 4.8: Mg-Zn phase diagram. Purple dashed line represents the equilibrium composition of Mg-6Zn. Green and blue dashed lines represent the regular solidification pathway to form (Mg)+Mg_7Zn_3. Orange dashed line represents the hypothetical pathway to form $MgZn_2$ [100]

4.4.2. Effect of nano-treating on particle size and mechanical properties

The effect of nano-treating on particle size was analyzed by comparing the primary TiB_2 particle size in RHMS, and NT HMS (Figure 4.9 (a)). The particle size histogram was generated by using image processing software, ImageJ, in which a grey scale threshold was determined based

on the TiB_2 grey scale, below which the features were filtered out. The Fe matrix and Fe_2B phase were hence removed. The remaining TiB_2 particles were analyzed for their quantity and cross-sectional area, subsequently the average particle size was calculated. For each sample, three SEM micrographs at the same magnification were used to produce statistics, and particle area below 1 μm^2 were filtered out as noise.

Representative images for particle size analysis are shown in Figure 4.3. The treatment by micro-TiB_2 particles did not produce a significant refinement effect despite the slight reduction in particle size, since the micro-treated HMS sample contains higher volume percentage of TiB_2 than RHMS, therefore, it is expected that the micro-treated HMS will have slightly smaller particle size. Nano-treating significantly refined the primary TiB_2 size from 25 to 5 μm, due to the nucleation effect of the nanoparticles on the formation of primary TiB_2 during solidification. This refinement effect was further confirmed by the ribbon-treated HMS sample, as shown in Figure 4.4 (d), in which the TiB_2 nanoparticles were incorporated into the RHMS melt via melt spun ribbon without molten salt assistance. The refinement effect achieved by this method was similar to the regular NT process.

Vickers hardness measurement and tensile test were used to evaluate the effect of NT on the mechanical property of RHMS, as shown in Figure 4.9 (b) and (d). The hardness of as cast RHMS sample increased from 180±6 $HV_{0.5}$ to 386±9 $HV_{0.5}$ after nano-treating, mainly due to the formation of Fe_2B lamella. The refinement of TiB_2 particles also had a contribution to hardness enhancement; however, this contribution was not significant as the TiB_2 particles are several microns in size, The hot working process reduced the hardness of NT HMS sample from 386.1 $HV_{0.5}$to 314.6 $HV_{0.5}$, due to the morphology evolution of the Fe_2B, from a rigid lamella structure to an equiaxed particle morphology. The Young's modulus of the hot worked NT HMS sample of

246 GPa was unaffected by the Fe_2B phase, which is considered undesirable due to its low Young's modulus, and agrees with the previously reported value at similar TiB_2 volume fraction[8]. The tensile strain of the hot worked RHMS sample was 15.5%, lower than previousy reported value[8], likely due to the defects generated during the hot working process. The tensile strain of the hot worked NT HMS sample was 14%, comparable to that of hot worked RHMS sample, indicating that the nano-sized Fe_2B had almost no negative effect on the ductility.

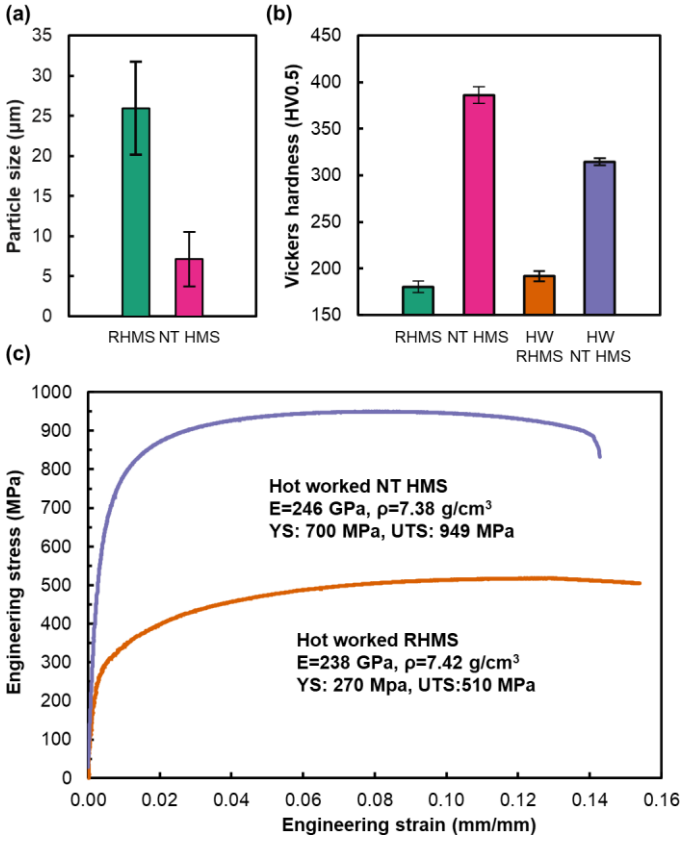

Figure 4.9: Histogram of (a)TiB_2 particle size in RHMS and NT HMS, and (b)Vicker's hardness of as cast and hot worked HMS sample. (c)Tensile testing results and mechanical properties of hot worked NT HMS and RHMS samples.

4.5. **Conclusions**

In this chapter, a nanoparticle-induced novel microstructure of Fe-Ti-B based HMS that utilizes a small amount of TiB_2 nanoparticles as nucleation agents during near equilibrium solidification is presented. The nano-treating of HMS resulted in a new phase composition and morphology. First, the primary TiB_2 particles became a combination of TiB_2 and Fe_2Ti with a coherent interface. Second, the Fe matrix became Ti-poor, promoting the formation of the Fe_2B lamellae. To explain this novel microstructure, we propose a solidification mechanism featuring two distinct liquid compositions, due to the presence of reactive nanoparticles. The proposed solidification mechanism is in good agreement with the calculated phase diagrams, DSC analysis results, as well as the observed microstructure; it is also consistent with our previous work on the Mg-Zn system with SiC nanoparticles. The new mechanism opens the possibility of altering the solidification path by the addition of nanoparticles in other alloy systems to achieve phase composition and morphology that cannot be achieved via conventional solidification.

The Fe_2B phase transformed into nanoparticles (APS 200 nm) upon hot working. The resulting hot worked NT HMS retained a high Young's modulus (251 GPa) and specific stiffness (34 $GPa \cdot cm^3 \cdot g^{-1}$), owing to the high volume fraction of TiB_2 micro-particles (15 vol.%), while achieving high specific YS (104 $MPa \cdot cm^3 \cdot g^{-1}$) and specific UTS (129.5 $MPa \cdot cm^3 \cdot g^{-1}$), owing to the strengthening effect of nano-sized Fe_2B particles. Our processing concept successfully turned a previously unwanted and actively suppressed Fe_2B phase into a beneficial strengthening phase of HMS. This method provides an innovative pathway to produce HMS, and has the potential to be used in other alloy systems.

In Chapter 3 and Chapter 4, experiments to suppress the reactivity between nanoparticles and a reactive melt are presented.

Chapter 5. Theoretical and experimental study of minor alloying element effects on dispersion of oxide nanoparticle in steel

In Chapter 3 and Chapter 4, experiments to suppress the reactivity between nanoparticles and a reactive melt are presented. The suppression of reactivity by reducing the temperature in Invar/WC system only showed promising results when the temperature is reduced to well below melting point, combined with a short solid state processing duration, the WC nanoparticles are able to retain their size. Therefore, this method is not effective in enabling Fe-based MMNCs to be produced via liquid metallurgy. The suppression of reactivity by a chemical method is presented in the Fe-Ti-B system nano-treated by TiB_2 nanoparticles. While individual TiB_2 nanoparticle is unable to survive the process, the addition of TiB_2 nanoparticles into the melt causes highly unusual and scientifically intriguing solidification phenomenon. The solidified microstructure contains nano-features that are not previously shown nor predicted. The properties of the nano-treated HMS are also outstanding. However, the method, while being a successful demonstration of producing Fe-based MMNC by liquid metallurgy, is difficult to be generalized into other Fe-based systems, because very few Fe-based system share similar phase diagram features (such as being pseudo-eutectic) with Fe-Ti-B system. To this end, a more universal method is needed.

Ionocovalent oxides have higher thermodynamic stability than the metal-like ceramics. Molten steels have very limited reactivity with ionocovalent oxides. If oxide nanoparticles can be incorporated into liquid steel, the reaction issue encountered in previous chapters will be largely bypassed. However, ionocovalent oxides, due to having partial ionic and partial covalent bond, do not tend to form strong bonds with molten steel, resulting in poor interfacial adhesion. The poor interfacial adhesion manifests in the measurable engineering parameters such as work of adhesion and contact angle. In addition, oxides and metals have large difference in their Hamaker constants,

which are in the range of 100-150 zJ for oxides and 300-400 zJ for metals [101]–[103]. Such difference in Hamaker constants resulted in high vdW attraction potential (Eqn. 17) between the oxide nanoparticles in molten steel, which can cause the nanoparticles to be trapped in pseudo-clusters or be sintered if the interfacial energy barrier is overcome.

To this end, the oxide nanoparticle incorporation and dispersion in molten steel can only be achieved when two conditions are satisfied:

1. The oxide nanoparticles have a good wettability, due to a strong interfacial adhesion, with molten steel. This gives rise to large interfacial energy barrier against particle sintering.
2. The vdW attraction between the oxide nanoparticles is low. The thermal energy would allow the nanoparticles to break free from pseudo-clusters caused by vdW potential well, and disperse uniformly in the melt.

The wetting behavior between oxides and molten steels is well studied in conventional steel metallurgy. Oxides, such as MgO, Al_2O_3, CaO, and SiO_2, are the main components of slag, which is considered detrimental to the steel product. Therefore, in a conventional steelmaking process, to separate the slag from the molten steel, a poor wetting (high contact angle) between the two is often favored [104]. In this work, the reverse is favored. This chapter examines the effect of several alloying elements on the interfacial adhesion and wettability between the oxide and the molten steel using theoretical modeling approach, then validate their effect using experiments. The vdW attraction is also studied under the same theoretical framework.

5.1. **Theoretical study of the work of adhesion and wetting angle in Fe-x (x=Cr, Si, Mn, or Nb)/oxide systems**

Pure liquid iron has poor wettability and low work of adhesion with most of metal oxides, as shown in Table 5. Oxides such as Cr_2O_3, TiO_2, and NiO exhibit better wettability with pure liquid iron (θ~60-90˚), but these oxides have low thermodynamic stability and are generally not selected as reinforcing phase in ODS steels.

Table 5: Contact angle and work of adhesion between oxides and pure liquid iron at 1823 K

	Contact angle, θ (deg)	Work of adhesion, W (J/m^2)
Al_2O_3	115-135 [105], [106]	0.65-1.20 [11], [106]
Y_2O_3	105 [107]	~1.35 [107]
ZrO_2	115 [106]	1.01 [106]
MgO	125 [105], [106]	0.90 [106]

Some literature works suggest that the contact angle between liquid can be tuned when certain alloying elements are added. Verhiest et al. demonstrated the effect of Cr and Si addition on the contact angle between liquid iron and oxides (Y_2O_3 and Al_2O_3), and found that 20 wt.% Cr reduces the contact angle by 20˚ in pure iron while 0.5 wt.% Si reduces the contact angle by 10˚ in Fe-9Cr melt [107]. Yu et al. studied the effect of Nb (0-1.48%) addition on the contact angle between liquid medium Mn steel (8% Mn, 1%C) and Al_2O_3. It was found that 1.15% Nb reduces the contact angle to below 50˚ [108]. Due to the different chemical composition in the liquid steels and the experimental setup including temperature, holding duration, atmosphere, etc., it is difficult to determine the relative potency of each alloying element in improving the wettability. Therefore, a theoretical modeling of the contact angle and work of adhesion between an ideal binary Fe-x

(x=Cr, Si, Mn, or Nb) and Al_2O_3 (or Y_2O_3) is performed. Element Cr is selected because it is the main alloying element for stainless steel, while Mn and Si are the most common alloying element in plain carbon steels. Element Nb is selected due to its reported potency for improving wettability at as low as ~1 wt.%.

5.1.1. Theoretical framework

The theoretical framework to predict the change in work of adhesion and contact angle between a liquid binary alloy A-B and an oxide was established by Li et al., as reviewed in section 2.3. [64]. This framework is based on three basic assumptions: 1) the binary alloy A-B has a very low concentration of metal B, that is, element B is infinitely diluted in metal A; 2) the binary alloy A-B is considered as a regular solution, that is, the enthalpy of mixing is non-zero; 3) the liquid A-B alloy does not react with the oxide. The parameters and their definitions used in this model are shown in Table 6. The molar exchange energy of the liquid AB, λ, as given by Eqn. 11, is difficult to calculate due to the lack of literature data on the bond energy, ε_{AB}, for some of the systems, such as Fe-Mn, Fe-Nb. Instead, this parameter is evaluated from the tabulated values of partial mixing enthalpies of binary alloys AB at infinite dilution[64], [109].

Table 6: Parameter symbols and their definitions

Parameter symbol	Definition
σ_{LV}^{A}	surface energy of liquid pure metal A
σ_{LV}^{B}	surface energy of liquid pure metal B
W^A	work of adhesion between pure metal A and oxide
W^B	work of adhesion between pure metal B and oxide

θ^A	contact angle between liquid pure metal A and oxide
θ^B	contact angle between liquid pure metal B and oxide
x_B	molar fraction of B in bulk liquid
y_B	molar fraction of B in interfacial liquid layer
σ_{SL}	interfacial energy between liquid AB and oxide
σ_{SV}	surface energy of solid oxide
λ	molar exchange energy of the liquid AB
Ω_M	molar surface area of the liquid AB
$E_{SL}(B)_A$	energy of adsorption of metal B at the metal A-oxide interface in liquid AB
$E_{LV}(B)_A$	energy of adsorption of metal B at the surface of metal A in liquid AB

The same theoretical framework is also used to calculate the potential enrichment of metal B on the surface of oxide in liquid AB by using Eqn. 13. Under this framework, it is proposed that a monoatomic interfacial layer with composition y_B will exist on the surface of the oxide. The presence of the interfacial layer can serve as a "dynamic coating" for the oxides that effectively reduces its difference in Hamaker constant with the melt. The schematic of the vdW attraction between two nanoparticles without interfacial layers in a melt is shown in Figure 2.22 c, and can be calculated using Eqn. 17. The vdW attractions between two nanoparticles with interfacial layers is illustrated in Figure 5.1.

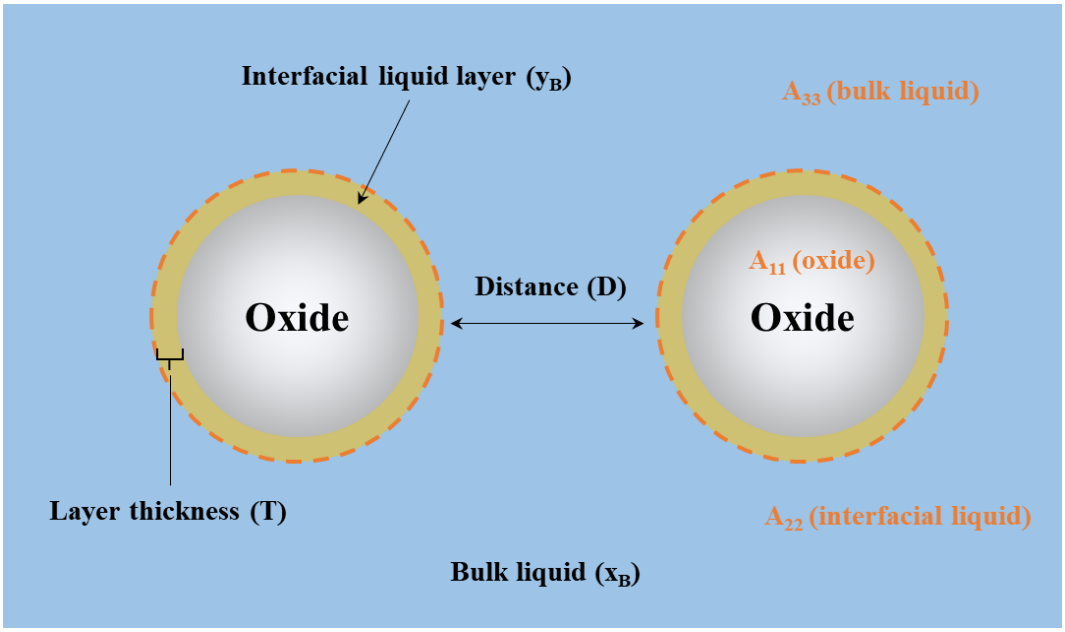

Figure 5.1: Schematic of the vdW attraction between two oxide nanoparticles with interfacial liquid layer (y_B) in a melt with composition of x_B.

In this scenario, the interfacial liquid layer has a variable thickness T. The Hamaker constants for the solid phase (oxide nanoparticle), interfacial liquid layer, and bulk liquid are A_{11}, A_{22}, and A_{33}, respectively. The vdW attraction potential between the two oxide nanoparticles is given by Eqn. 20, and the associated Hamaker constants are calculated by Eqn. 21, Eqn. 22, and Eqn. 23 [110]. When the interfacial liquid layer thickness is 0, Eqn. 20 reduces to Eqn. 17.

$$W_{vdW}(D) = \frac{R}{12}\left(-\frac{A_{232}}{D} + \frac{2A_{123}}{D+T} - \frac{A_{121}}{D+2T}\right) \quad \text{Eqn. 20}$$

$$A_{232} \approx \left(\sqrt{A_{22}} - \sqrt{A_{33}}\right)^2 \quad \text{Eqn. 21}$$

$$A_{123} \approx \left(\sqrt{A_{11}} - \sqrt{A_{22}}\right)\left(\sqrt{A_{33}} - \sqrt{A_{22}}\right) \quad \text{Eqn. 22}$$

$$A_{121} \approx \left(\sqrt{A_{11}} - \sqrt{A_{22}}\right)^2 \quad \text{Eqn. 23}$$

5.1.2. Evaluation of parameters

The AB alloy/oxide system in this work includes Fe-Si/Al_2O_3, Fe-Cr/Al_2O_3, Fe-Mn/Al_2O_3, Fe-Nb/Al_2O_3 and Fe-Nb/Y_2O_3. The numerical values of the parameters required for the theoretical modeling are shown in Table 7. Using Eqn. 10 and Eqn. 12, the $E_{SL}(B)_A$ and $E_{LV}(B)_A$ values are calculated for each system, as shown in Table 8. Based on the inequalities between E_{SL} and E_{LV}, σ_{LV}^{B} and σ_{LV}^{A}, W^B and W^A, the type of change in work of adhesion and contact angle can be assigned to each system as shown in Figure 2.21.

Table 7: Numerical values of different parameters in alloy A-B/oxide systems at 1823K.

Alloy A-B	Oxide	σ_{LV}^{A} (J/m^2) [111]	σ_{LV}^{B} [111]*	σ_{SL}[11]	W^A [11]	W^B [11]	σ_{SV} [11]	λ (kJ/mol) [109]	Ω_M (10^4 m^2/mol)
Fe-Si	Al_2O_3	1.85	0.78	2.50	0.65	0.88	0.77	-75	3.4
Si-Fe		0.78	1.85	1.71	0.88	0.65		-67	4.8
Fe-Cr		1.85	1.70	2.50	0.65	2.30**		-6	3.4
Cr-Fe		1.70	1.85	0.20	2.30**	0.65		-6	3.4
Fe-Nb		1.85	1.93	2.50	0.65	2.60 [112], [113]		-70	3.4
Nb-Fe		1.93	1.85	0.10***	2.60[112], [113]	0.65		-57	4.5
Fe-Mn		1.85	1.11	2.50	0.65	0.86 [106]		1	3.4
Mn-Fe		1.11	1.85	1.02 [106]	0.86 [106]	0.65		1	3.5
Fe-Nb	Y_2O_3	1.85	1.93	1.07	1.5**	2.6	0.75 [114]	-70	3.4
Nb-Fe		1.93	1.85	0.1	2.6	1.5**		-57	4.5

*Evaluated at melting point of B if it is higher than 1823 K. **Calculated using contact angle and σ_{LV} with equation: $\cos(\theta)=W/\sigma_{LV}-1$[64]. ***Approximation using equation: $\cos(\theta)=(\sigma_{SV}-\sigma_{SL})/\sigma_{LV}$

Table 8: Evaluation of $E_{SL}(B)_A$ and $E_{LV}(B)_A$ adsorption energy values in alloy A-B/oxide systems and their corresponding type of change [64].

Alloy A-B	Oxide	$E_{SL}(B)_A$ (kJ/mol)	$E_{LV}(B)_A$ (kJ/mol)	Inequalities	Type[64]
Fe-Si	Al_2O_3	-25.450	-17.630	$E_{SL}<E_{LV}<0$, $\sigma_{LV}^B<\sigma_{LV}^A$, $W^B>W^A$	1
Si-Fe		79.150	68.110		
Fe-Cr		-59.700	-3.600	$E_{SL}<E_{LV}<0$, $\sigma_{LV}^B<\sigma_{LV}^A$, $W^B>W^A$	1
Cr-Fe		62.700	6.600		
Fe-Nb		-46.080	20.220	$E_{SL}<0<E_{LV}$, $\sigma_{LV}^B>\sigma_{LV}^A$, $W^B>W^A$, $(\sigma_{LV}^B-\sigma_{LV}^A)<(W^B-W^A)$	3b
Nb-Fe		98.400	10.650		
Fe-Mn		-32.550	-25.410	$E_{SL}<E_{LV}<0$, $\sigma_{LV}^B<\sigma_{LV}^A$, $W^B>W^A$	1
Mn-Fe		33.000	25.650		
Fe-Nb	Y_2O_3	-17.180	20.220	$E_{SL}<0<E_{LV}$, $\sigma_{LV}^B>\sigma_{LV}^A$, $W^B>W^A$, $(\sigma_{LV}^B-\sigma_{LV}^A)<(W^B-W^A)$	3b
Nb-Fe		60.150	10.650		

5.1.3. Evaluation of the effect of different alloying elements on wettability

Using the $E_{SL}(B)_A$ and $E_{LV}(B)_A$ adsorption energy values inTable 8, the slopes for the change of the work of adhesion and the contact angle in alloy A-B/oxide systems are calculated using Eqn. 15 and Eqn. 16. The values for the slope for each alloy AB system are summarized in Table 9. The slope values are used to generate W vs. x_B plot and θ vs. x_B plot for each alloy A-B/oxide system, as shown in Figure 5.2. The linear regions near $x_B \rightarrow 0$ and $x_B \rightarrow 1$ are limited within 2 at.% of solute in order to satisfy the assumption of high dilution of solute. The transition region beyond the linear region is connected by a smooth curve based on the type of change described in Figure 2.21.

Table 9: Values of $(\frac{dW}{dx_B})_{x_B \to 0}$ and $(\frac{d\cos\theta}{dx_B})_{x_B \to 0}$ for each alloy A-B/oxide system.

Alloy A-B	Oxide	$(\frac{dW}{dx_B})_{x_B \to 0}$ (J/m^2)	$(\frac{d\cos\theta}{dx_B})_{x_B \to 0}$
Fe-Si	Al_2O_3	0.963	0.710
Si-Fe		-0.002	-0.472
Fe-Cr		22.331	12.094
Cr-Fe		-0.281	-0.290
Fe-Nb		9.204	4.912
Nb-Fe		-0.166	0.204
Fe-Mn		1.434	1.145
Mn-Fe		-0.031	-0.274
Fe-Nb	Y_2O_3	1.267	0.523
Nb-Fe		-0.166	0.200

The Fe-Si/Al_2O_3 and Fe-Mn/Al_2O_3 systems share the most similarity, in which Si and Mn have slightly higher W value than Fe and the slightly lower θ value than Fe, resulting in the type 1 energy inequalities of $E_{SL}<E_{LV}<0$, $\sigma_{LV}^B<\sigma_{LV}^A$, and $W^B>W^A$. In either case, the work of adhesion and contact angle transitioned slowly between $x_B=0$ to 1, indicating that Si and Mn will slightly increase the wettability between the liquid and the oxide, but not significant at low concentration. For Fe-Cr/Al_2O_3 system, although the energy inequalities are still type 1, Cr has much higher W value and lower θ value than Fe, resulting in a steeper drop in θ. At 20 at.% Cr, which is the normal Cr concentration in stainless steel, the model predicts the contact angle to be around 90˚.

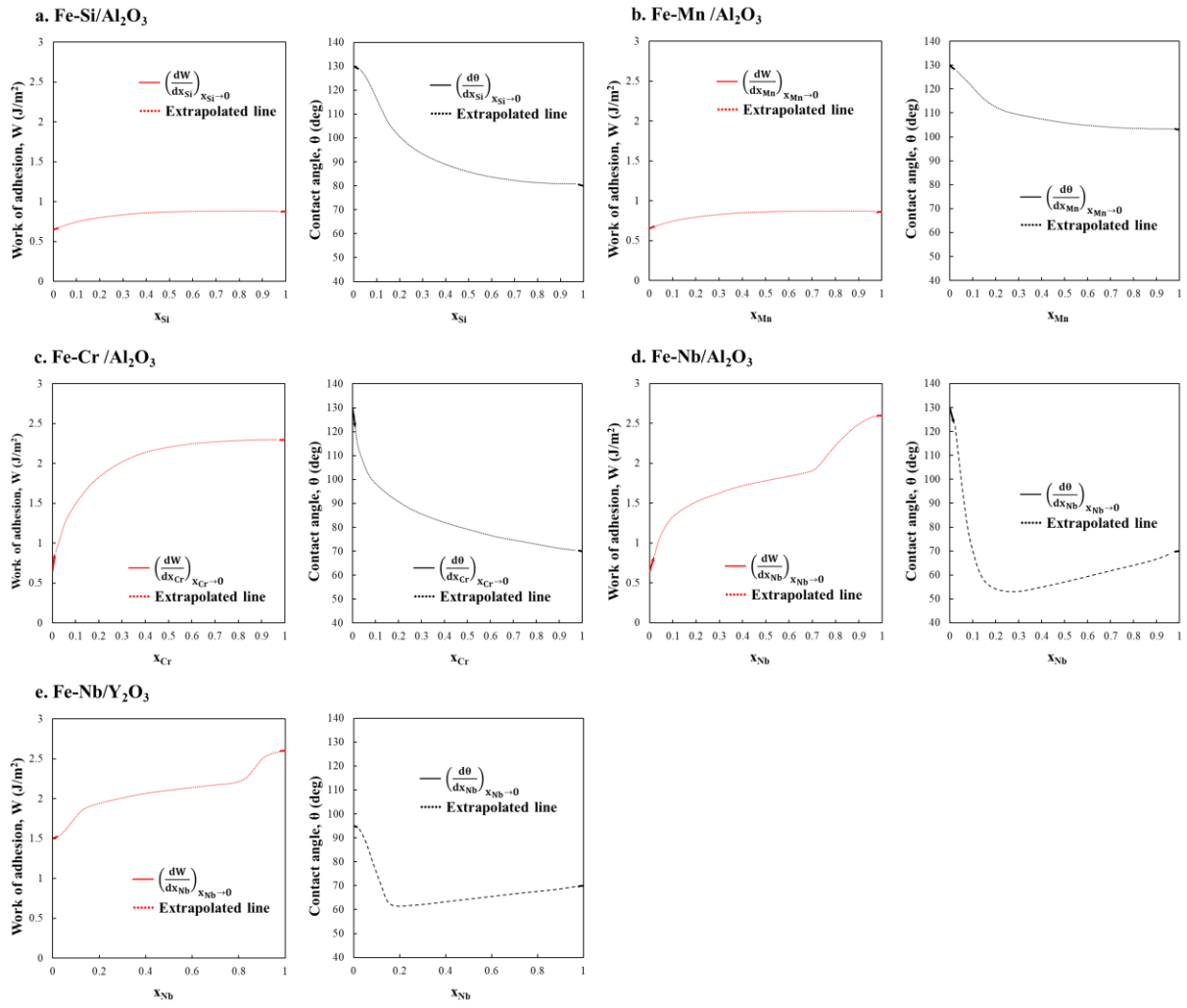

Figure 5.2: W(x_B) and θ (x_B) isotherms for (a) Fe-Si/Al_2O_3, (b) Fe-Mn/Al_2O_3, (c) Fe-Cr/Al_2O_3, (d) Fe-Nb/Al_2O_3, and (e) Fe-Nb/Y_2O_3.

The Fe-Nb/Al_2O_3 and Fe-Nb/Y_2O_3 systems are the only systems with the energy inequalities of type 3b due to Nb having higher liquid surface energy than Fe, resulting in adsorption energy E_{LV}>0. The type 3b system is unique because the model predicts a specific composition in which a minimum contact angle exist that is lower than the contact angle with either pure A or pure B. Yu et al.'s experimental work seems to confirm this prediction, in which 1.15 wt.% of Nb achieved a lower contact angle (50˚@1823K) than 0.83 wt.% of Nb (60˚@1823K)

or 1.48 wt.% Nb (70˚@1823K), in the Fe-Mn-C-xNb(x=0-1.48%)/Al_2O_3 system [108]. The model here deviates from Yu's work in predicting the exact concentration of Nb needed to reach minimum contact angle and the value of the minimum contact angle. Yu's work suggests that an interfacial reaction between Nb and Al_2O_3 takes place and further reduces the contact angle. This theory cannot be accounted for in a model for non-reactive system.

In summary, among the 5 binary alloy systems examined, element Si and Mn showed limited effect in reducing the contact angle. Element Cr is more potent than Si and Mn, but requires high concentration (~20 at.%) to reach a favourable contact angle (<90˚). The Fe-Nb/Al_2O_3 and Fe-Nb/Y_2O_3 are the only type 3b systems indicating that element Nb potentially has the strongest effect in improving the wettability and requires experiment to confirm its effect.

5.1.4. Evaluation of the effect of different alloying elements on vdW attraction between oxide particles

Based on the results from previous section, three A-B/oxide systems, Fe-Nb/Al_2O_3, Fe-Cr/Al_2O_3, and Fe-Nb/Y_2O_3, are evaluated for the effect on vdW attraction. The vdW attraction potential between two oxide nanoparticles are calculated using Eqn. 20-Eqn. 23. The Hamaker constants, A_{11}, of Al_2O_3 and Y_2O_3 are 150 zJ and 130 zJ [102]. The Hamaker constant, A_{33}, of the bulk liquid is assumed to equal to that of Fe, 392 zJ , due to the high dilution of Nb or Cr [101]. The Hamaker constant, A_{22}, of the interfacial liquid layer is approximated using a simple rule of mixture based on the interfacial composition, y_B: $A_{22}=y_B*A_B+(1-y_B)*A_{33}$, in which A_B is the Hamaker constant of the metal B. The nanoparticle distance, D, of 0.4 nm (two atomic layers) is used. The vdW attraction potentials between two oxide nanoparticles are shown in Figure 5.3.

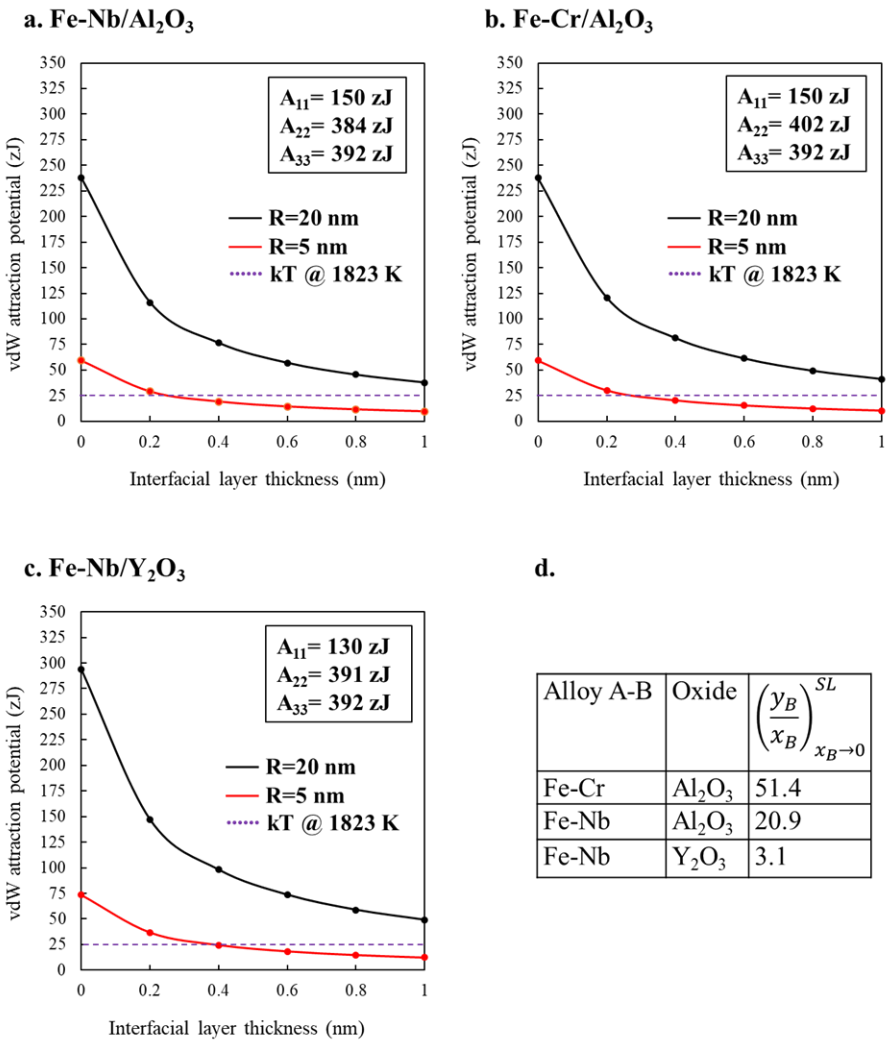

Alloy A-B	Oxide	$\left(\frac{y_B}{x_B}\right)^{SL}_{x_B \to 0}$
Fe-Cr	Al_2O_3	51.4
Fe-Nb	Al_2O_3	20.9
Fe-Nb	Y_2O_3	3.1

Figure 5.3: vdW attraction potential vs. interfacial layer thickness plot at nanoparticle radius of 20 nm or 5 nm for (a) Fe-Nb/Al_2O_3, (b)Fe-Cr/Al_2O_3, (c)Fe-Nb/Y_2O_3, and (d) table for the y_B/x_B values. The x_B value is set at 0.01 for each system.

The interfacial layers are highly effective in reducing the vdW attraction between oxide nanoparticles in steel melt. When the interfacial layer is one atomic layer (0.2 nm), the vdW attraction potential is almost reduced by half in all three systems. When the interfacial layer is three atomic layers (0.6 nm), the vdW attraction potential is reduced by about 75%. Despite having very different y_B/x_B values in the three systems (Figure 5.3 d), the Hamaker constant of the

interfacial layer, A_{22}, is relatively unaffected, due to the similar Hamaker constants for Cr (371 zJ), Nb (464 zJ) and Fe (392 zJ) [101]. For a nanoparticle with a larger radius (R=20 nm), the thermal energy, kT, is lower than the vdW attraction potential. However, the reduction of vdW attraction potential allows for a significantly higher probability for the nanoparticles to break free from the pseudo-clusters. The probability for a particle to overcome an energy well is proportional to $e^{-\Delta E/kT}$. Therefore, at a fixed kT of 25 zJ, a particle is 400 times more likely to overcome a 150 zJ well than a 300 zJ well ($e^{-150/25}/e^{-300/25}=400$), or 8100 times more likely to overcome a 75 zJ well ($e^{-75/25}/e^{-300/25}=8100$).

In summary, among the 3 systems examined, Cr and Nb are highly effective in reducing the vdW attraction potential between two Al_2O_3 or Y_2O_3 nanoparticles. The presence of the metallic interfacial liquid layer (y_B) has a strong screening effect to the large Hamaker constant difference between A_{11} (oxide) and A_{33} (bulk liquid). The vdW attraction potential is reduced for up to 50% even with only one atomic layer thick of the interfacial liquid layer.

5.2. Experimental study on the effect of Nb on the wettability between molten steels and oxide nanoparticles

5.2.1. Experimental design and procedure

To verify the effect of Nb on the wettability between different steel compositions and oxide nanoparticles, liquid metallurgy experiments were conducted. In molten metal/nanoparticle system, high wettability between the melt and nanoparticles provides a strong interfacial energy barrier that makes nanoparticle contacting and sintering with each other heavily energetically unfavorable. However, for two nanoparticles that are already sintered together, the high wettability offers little

help, because the thin liquid film separating them no longer exists. To this end, it is crucial to prevent the sintering of nanoparticles by physically separate them during the incorporation stage, because they have yet to be wetted by the molten metal. For nanoparticles like carbides and borides, molten salt assisted incorporation works well because carbides and borides can form stable colloids in molten salt through the formation of a layer of surface-bound solvent ions which prevents aggregation and sintering [115], but the minimization of interfacial energy allows carbides and borides to migrate to molten metals [54]. However, for oxide nanoparticles, molten salt assisted incorporation does not work due to the strong chemical reaction between the two [54].

In this study, metal micro-powders were used as "spacers" to provide separation between oxide nanoparticles. First, steel micro-powders of different composition were mixed with 2 vol.% oxide nanoparticles. Organic solvents (ethanol or acetone) were added to the mixture creating a slurry. The slurry was treated in an ultrasonic bath for 10 min. The ultrasonic bath helps breaking up the oxide nanoparticle clusters and improves the uniformity of mixing, while the organic solvent absorbs the moisture. The slurry mixture was then dried at 60 ˚C to evaporate the solvent. The dried powder mixture was rigorously ground in a mortar and pestle set for 0.5 – 1 hr for uniform mixing. The ground powders were transferred to a stainless steel mold for cold compaction. The cold compaction pressure is ~400 MPa in uniaxial compression. The compacted powder pellet is referred to as the "powder master" herein.

A steel with desired composition was melted at 1560 ˚C under argon protective atmosphere. To verify the effect of Nb on the wettability of the molten steel, 1 to 1.2 wt.% Nb was added to the melt. Stirring is applied to promote the dissolution and uniform mixing of the Nb in the melt. The melt is referred to as the "base" herein.

The powder master pellets were added to the molten steel base at a weight ratio of 1:10. Stirring was applied to promote the dissolution of the master, and the uniform mixing of the oxide nanoparticles. The furnace was then turned off, allowing the molten steel to solidify slowly (cooling rate < 5 K/s). A schematic of the overall process is shown in Figure 5.4, in which, after the addition of the powder master, the dispersion of oxide nanoparticles can only occur in a melt with high wettability.

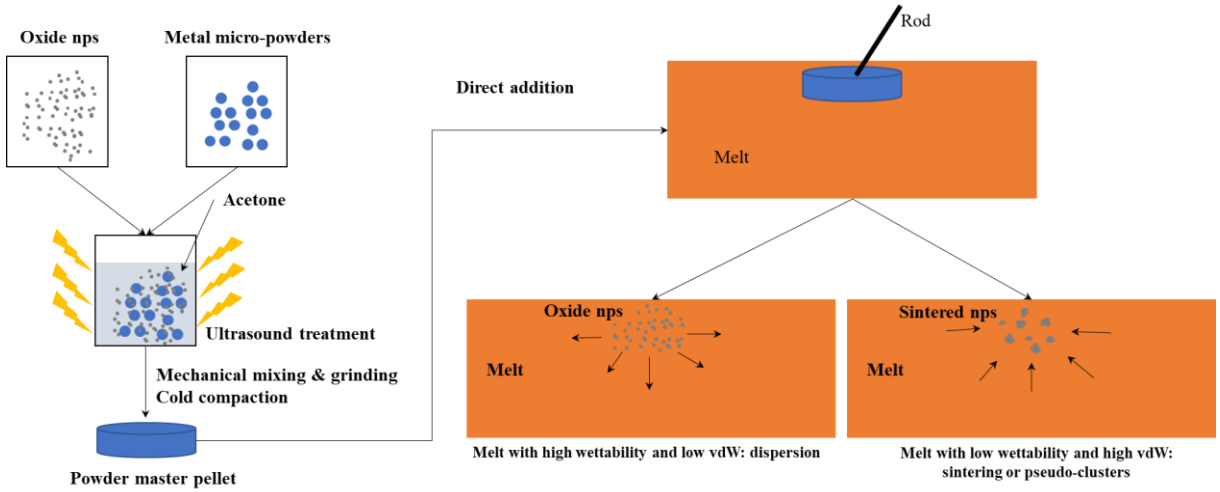

Figure 5.4: Schematic of oxide nanoparticle incorporation in molten steel using powder master pellet.

The different compositions of steel micro-powder, steel base, and oxide nanoparticles tested in this study are summarized in Table 10. The experiments can be divided into 3 categories. In category 1, the micro-powder was pure Fe (APS 100 μm) and the steel base was a binary Fe-1.2Nb alloy. The oxide selected for this category was Al_2O_3 (APS 300 nm). Category 1 was designed to be a simple system that verifies whether Nb improves the wettability and dispersion capability. In category 2, the micro-powder was stainless steel 316L (APS 40 μm) and the steel base was also 316L but with 1% Nb added. Category 2 represents the scenario in which both Cr

and Nb are present in the melt. In category 3, the micro-powder was medium Mn steel (MMS) and the steel base was a lean low carbon steel with 1.2% Nb, resulting in a final composition of Fe1.2Nb0.62Mn0.15C0.06Si, closely resembling that of a commercial low carbon steel. Category 3 was designed to test the effect of Nb in the most commonly used and versatile type of steel---low carbon steel. For each category, a steel base that contained no Nb was used as a blank reference. After the melt was solidified, the ingot was cut, polished, and examined under SEM.

Table 10: Compositions of steel micro-powder and steel base, and the oxide nanoparticle type selected.

Category	Steel micro-powder composition in wt.%	Steel base composition	Oxide
1. Binary Fe-Nb	Pure Fe	Fe1.2Nb	Al_2O_3 (300 nm)
2. Stainless steel	316L (Fe17Cr13Ni2.2Mo0.8Si0.2Mn0.03C)	316L-1Nb	Al_2O_3 (50 nm) Y_2O_3 (50 nm)
3. Low carbon steel	Medium Mn steel (Fe7Mn1Nb1C1Si)	Fe1.2Nb0.2Mn0.1C	Al_2O_3 (50 nm) Y_2O_3 (50 nm)

5.2.2. Results

5.2.2.1. Binary Fe-Nb/Al_2O_3 system

The microstructures of Fe-1.2Nb-0.12Al_2O_3, equivalent to 0.2 vol.%, are shown in Figure 5.5 (a) and (c). At low magnification (Figure 5.5 (a)), two phases with light contrast can be observed; the one with irregular shape and higher aspect ratio is Fe-Nb intermetallic, formed after solidification due to the poor solubility of Nb in Fe matrix. The phase with equiaxed and circular morphology is Al_2O_3, retaining their size and shape prior to incorporation. High magnification (Figure 5.5 (c)) shows that the Al_2O_3 nanoparticles are individually dispersed with no observable sintering issue. Figure 5.5 (d) shows the EDS spot analysis results for two areas selected in (c). Area 1 is selected on one Al_2O_3 nanoparticles, showing elevated Al concentration, while Area 2 is

selected in the matrix showing no Al signal. In comparison, the reference sample, where the powder master was added directly into pure Fe melt, contains sintered Al_2O_3 phase, as shown in Figure 5.5 (d), due to the poor wettability between pure Fe and Al_2O_3. The comparison between Figure 5.5 (a) and (b) is a clear indication that the addition of Nb drastically improves the wettability between Fe and Al_2O_3.

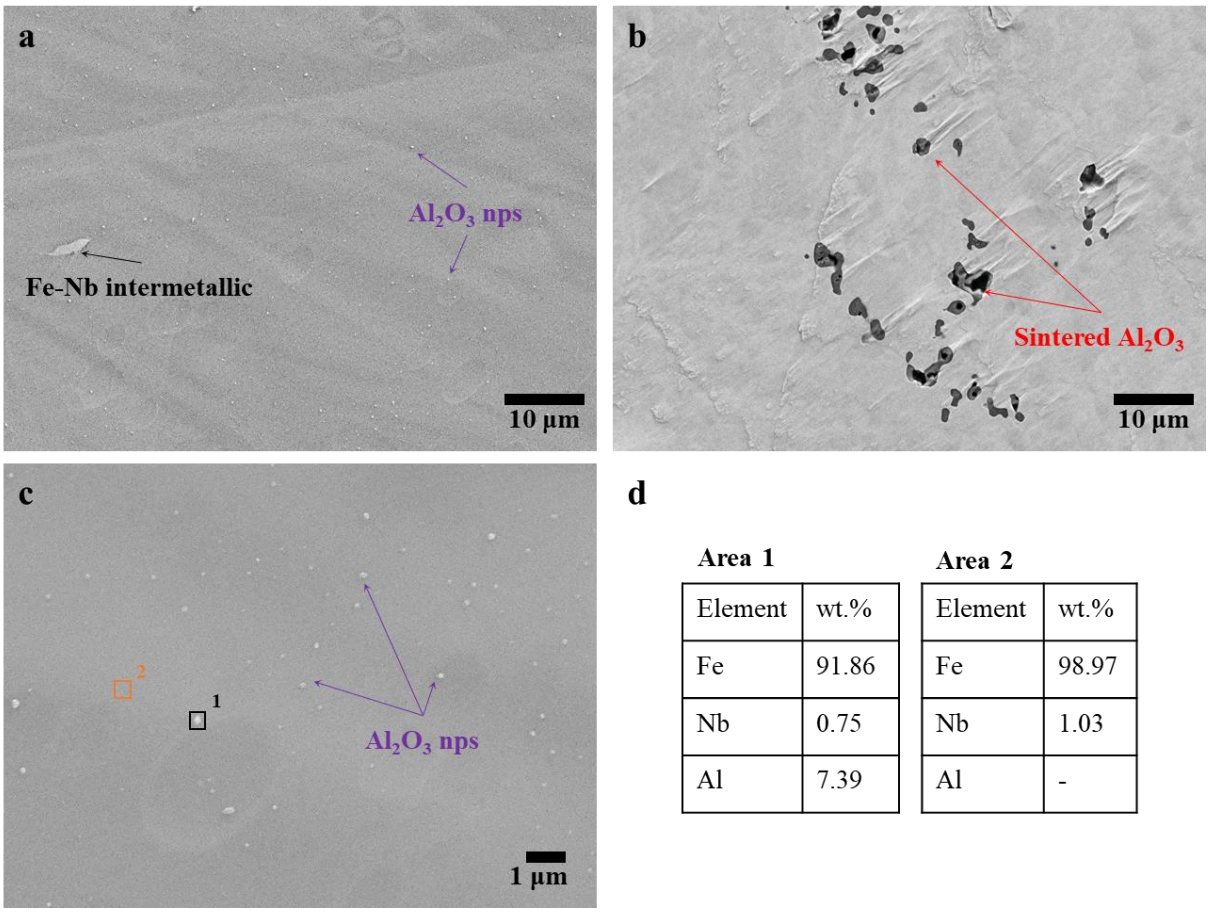

Area 1

Element	wt.%
Fe	91.86
Nb	0.75
Al	7.39

Area 2

Element	wt.%
Fe	98.97
Nb	1.03
Al	-

Figure 5.5: SEM micrographs of (a) and (c) as cast Fe-1.2Nb-0.12Al_2O_3 (in wt.%) at different magnification, (b) as cast Fe-0.12Al_2O_3, and (d) EDS analysis for selected areas in (c).

5.2.2.2. Stainless steel 316L-1Nb/Y_2O_3 and Al_2O_3 systems

316L is one of the most frequently used stainless steel. Its ODS variant is of great scientific interest. In the literature reviewed in section 2.1.2. , mainly Y_2O_3 are used as the strengthening phase in ODS stainless, due to its excellent high temperature properties. Liquid metallurgy experiments were nonetheless conducted for Al_2O_3 as well as Y_2O_3 to examine the effect of Nb. The as cast microstructures of the samples are shown in Figure 5.6. In the samples containing Nb, both Al_2O_3 and Y_2O_3 are well dispersed (Figure 5.6 (b) and (d)). In the reference sample containing no Nb, some well dispersed Al_2O_3 nanoparticles are observed, but at a much lower concentration (Figure 5.6 (f)). Micron-sized sintered Al_2O_3 are also observed, as shown in Figure 5.6 (e), similar to the case in pure Fe with Al_2O_3. At lower magnification, intermetallics are observed in all samples. In the reference 316L sample, the intermetallics are due to Mo, while in 316L-1Nb samples, the intermetallics contain both Mo and Nb, as they have low solubility at low temperature.

In comparison, the addition of Nb provides clear improvement to the wettability between the 316L matrix and the oxide nanoparticles (Y_2O_3 and Al_2O_3)and nanoparticle dispersion The oxide nanoparticles retained their small size (~50 nm) and equiaxed morphology. Without Nb, the 316L matrix still has limited wettability with the oxides due to the presence of 17% Cr, resulting in a small portion of the oxides being dispersed while the rest being sintered.

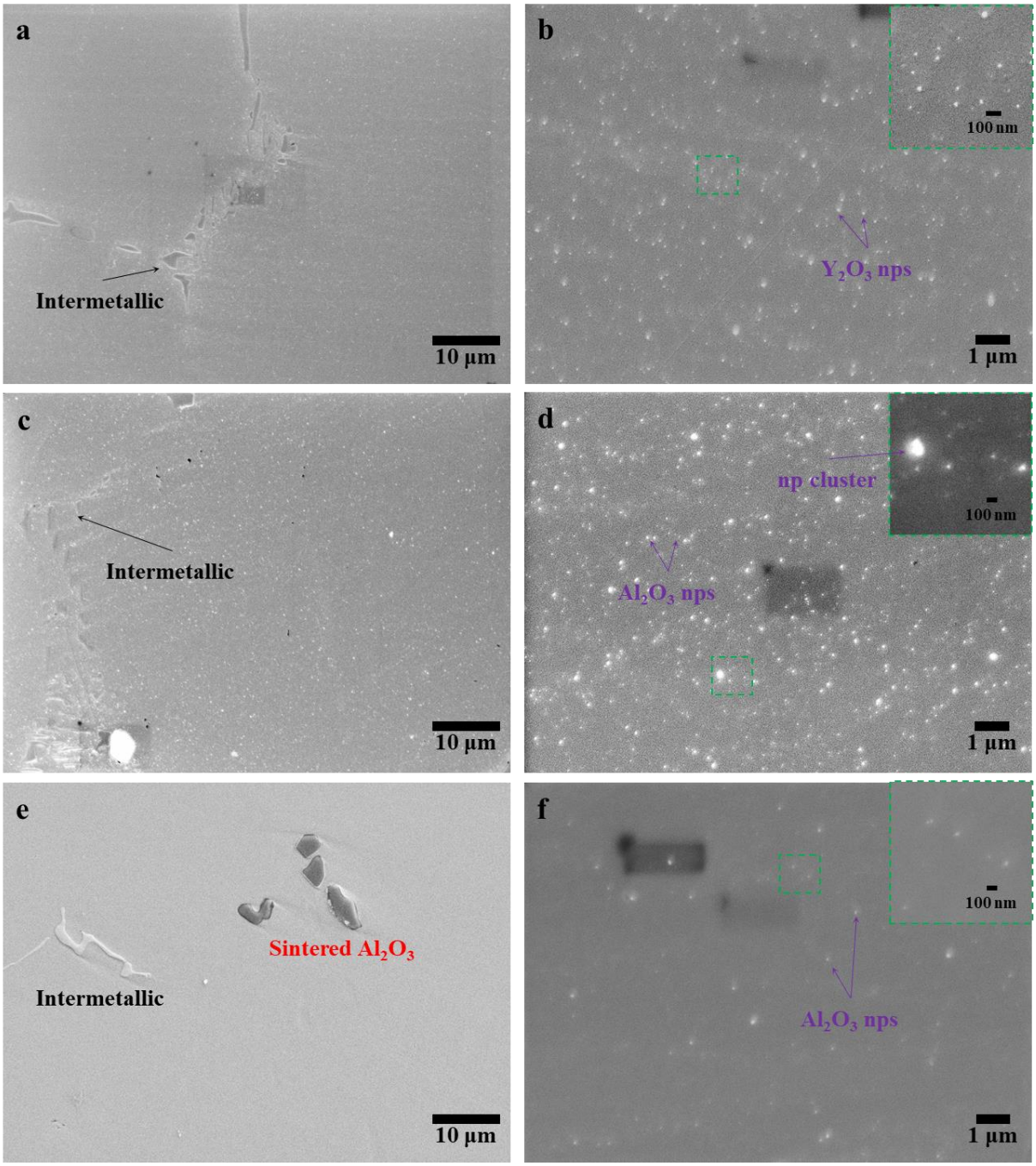

Figure 5.6: SEM micrographs of (a) and (b) as cast 316L-1Nb-0.13Y_2O_3 (in wt.%); (c) and (d) as cast 316L-1Nb-0.11Al_2O_3 ; (e) and (f) as cast 316L-0Nb-0.11Al_2O_3 (reference sample).

5.2.2.3. Low carbon steel/Y_2O_3 and Al_2O_3 systems

The microstructures of the ODS low carbon steel share similarity with that of ODS stainless steel from previous section, in which, the samples containing Nb have good dispersion of oxide nanoparticles (Y_2O_3 and Al_2O_3), as shown in Figure 5.7 (b) and (d), with no sintering observed. However, for the same volume percentage of designed oxide (0.2 vol.%), the ODS low carbon steel contained less oxides based on the comparison between the images at the same magnification. This is likely caused by the different wettability between the melt and the oxide nanoparticles, since the stainless steel melt contains high concentrations of Ni and Cr, while the low carbon steel melt contains very little amount of alloying element other than Nb. Therefore, the stainless steel melt is likely to have better wettability with the oxide or better surface solution enrichment, allowing most of the oxides to be incorporated and dispersed, while the low carbon steel melt, still having good wettability, is not as good. In the reference sample (Figure 5.7 (e) and (f)), no dispersed Al_2O_3 nanoparticle is observed, indicating that the wettability is poor between the Nb-free melt and the Al_2O_3 nanoparticles and the vdW potential is high between the Al_2O_3 nanoparticles in the steel melt.

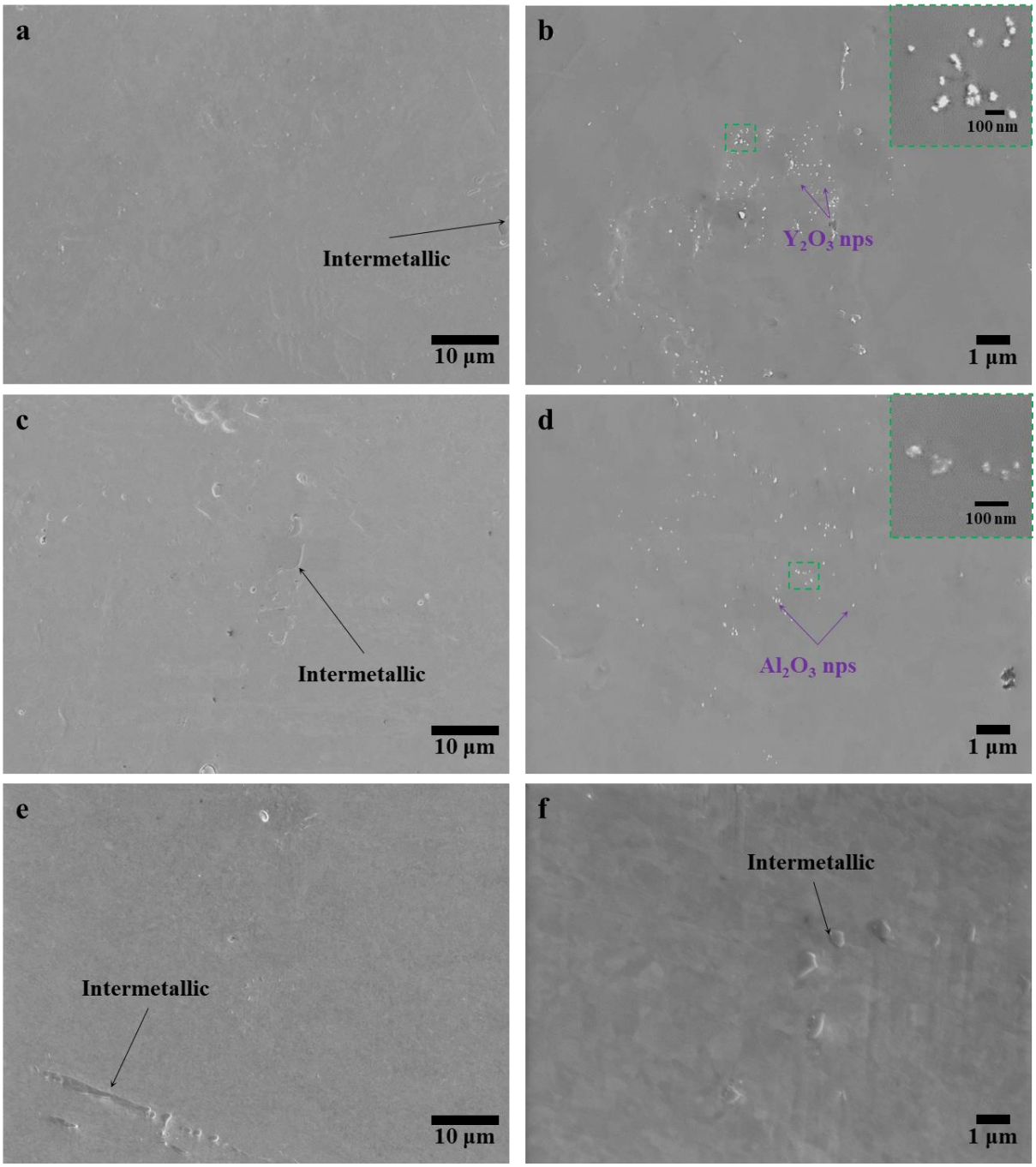

Figure 5.7: SEM micrographs of ODS low carbon steel (a) and (b) as cast Fe1.2Nb0.62Mn0.15C0.06Si-0.13Y_2O_3 (in wt.%); (c) and (d) as cast Fe1.2Nb0.62Mn0.15C0.06Si-0.11Al_2O_3; (e) and (f) as cast Fe0.62Mn0.15C0.06Si-0.11Al_2O_3 (reference sample).

Same sample from Figure 5.7 (c) and (d) was examined using STEM, as shown in Figure 5.8. The HAADF STEM image shows a Al_2O_3 nanoparticle in the Fe matrix. The EDS line scan conducted on the red dashed line detected no Nb in the Fe matrix region, but found a small Nb peak near the Al_2O_3 nanoparticle (Figure 5.8 (b)), indicating an enrichment of Nb near the interface. High magnification TEM image (Figure 5.8 (c)) on the interface. Using fast Fourier transform (FFT), the selected area electron diffraction (SAED) images of different regions on the imaging plane were acquired (Figure 5.8 (c) side panel). Based on the diffraction pattern, the interfacial layer between the Fe matrix and Al_2O_3 nanoparticle is identified to be Fe_2Nb (space group: P63/mmc), while the diffraction pattern of the Al_2O_3 nanoparticle is identified to be γ-Al_2O_3. The Fe_2Nb interfacial layer is approximately 2 nm thick.

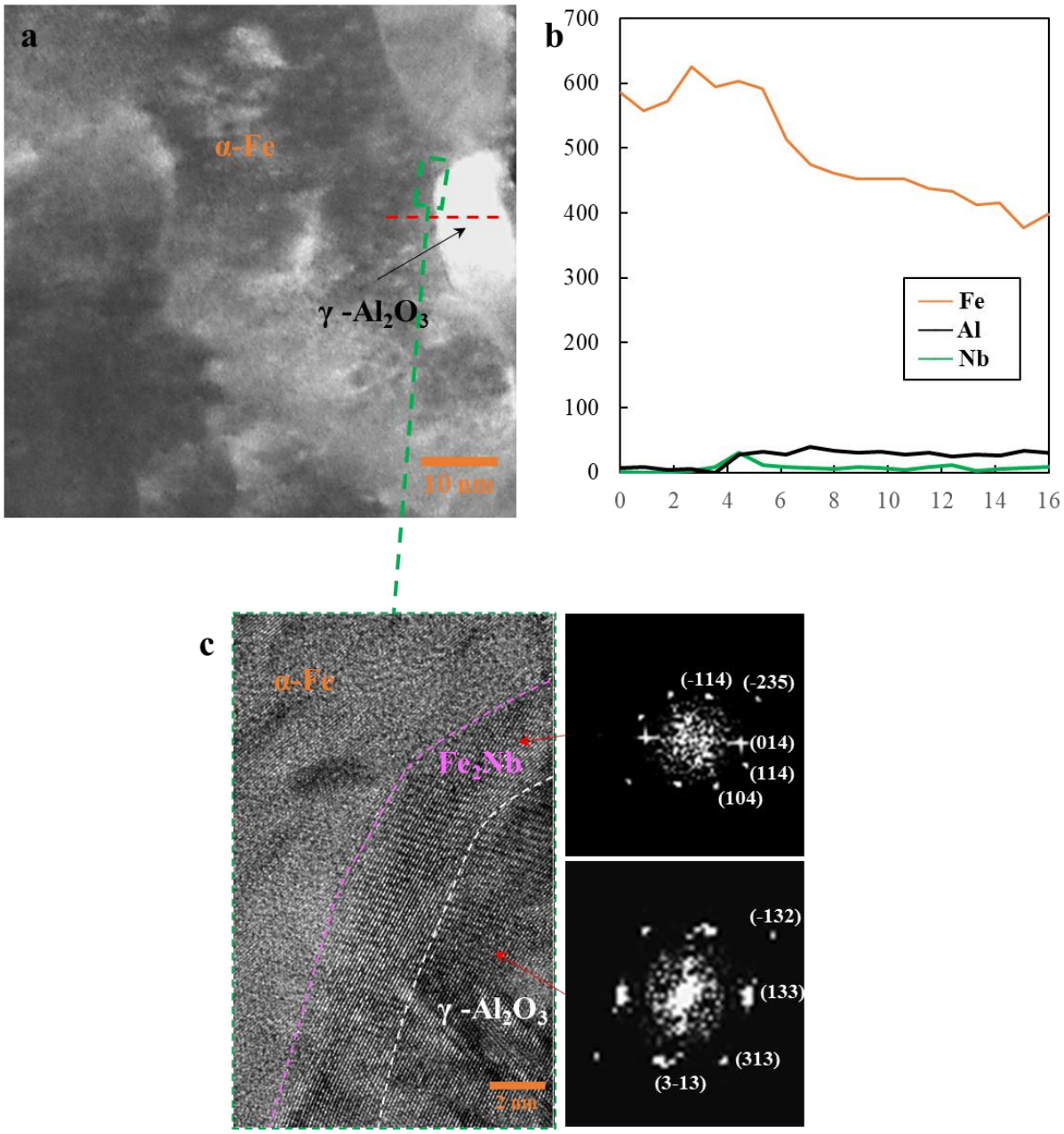

Figure 5.8: (a) HAADF STEM image displaying one Al_2O_3 nanoparticle in the Fe matrix. The red dashed line indicates a 16 nm segment of line in which the EDS line scan data was taken. (b) The elemental distribution (Fe, Al, and Nb) along the red dashed line in (a). (c)HRTEM image of the interface between Fe matrix and Al_2O_3 nanoparticle in the highlighted region in (a), and the corresponding SAED images.

5.2.3. Discussion

In the theoretical modeling portion of this study, the effect of Nb, Cr, Mn, and Si on the work of adhesion and contact angle between Fe and Al_2O_3 is predicted. It is found that Mn and Si have a limited effect, Cr has a moderate effect, and Nb has the strongest effect. In the experimental portion, this prediction is verified. The Nb concentration is 1.2% for the Fe-Nb and the low carbon steel systems, and 1% for the stainless steel. The Nb concentration is maintained at this level since Yu's results indicate that the optimal Nb concentration is in the vicinity of 1-1.2% [108]. In the Fe-Nb and the low carbon steel systems, the addition of Nb fundamentally changes the wettability from non-wetting to wetting. Without Nb, the oxides sintered in the melt, leaving no individually dispersed nanoparticle. With 1.2% Nb, the dispersion took place, and no sintered phase is observed. In the stainless steel system, the addition of Nb improves the wettability. Without Nb, the stainless steel melt still offers limited wettability and likely little reduction in vdW potential, which result in a portion being dispersed but a portion of the oxide being sintered. With 1% Nb, the sintering no longer takes place, resulting in individually dispersed nanoparticles. Furthermore, we found that Nb not only improves the wettability for Al_2O_3, but also for Y_2O_3, a more favorable oxide choice for application. In summary, we found that Nb addition improves the dispersion of both Al_2O_3 and Y_2O_3 nanoparticles in various steel compositions, including the simple binary Fe-Nb, the low-alloyed low carbon steel system, and the high-alloyed stainless steel system.

The modeling on vdW attraction potential (Figure 5.3 a-c) suggests that the presence of an interfacial liquid layer will strongly reduce the vdW attraction between two nanoparticles in the steel melt. While smaller nanoparticles (R=5 nm) yield much lower vdW attraction, which can be easily overcome by thermal energy, larger nanoparticles (R=20 nm) still have a good probability breaking free from the vdW potential well. This modeling was experimentally validated in various

systems, in which nanoparticle pseudo-clusters were not observed. The STEM image and the EDS line scan (Figure 5.8 (a) and (b)) indicates the presence of Nb enriched regions around the Al_2O_3 nanoparticles. At room temperature, Nb has a very low solubility in Fe, primarily forming Fe_2Nb (Laves) intermetallics. This is supported by the HRTEM image as shown in Figure 5.8 (c), in which the interfacial layer between Al_2O_3 and Fe matrix is identified to be Fe_2Nb. Therefore, the formation of Fe_2Nb interfacial layer around the Al_2O_3 nanoparticle can be attribute to the Nb enrichment around the nanoparticle in liquid state due to strong interfacial adhesion, and subsequent solidification allows the Nb beyond solubility limit to precipitate out as Fe_2Nb around the nanoparticle. The S/TEM observation also suggests the thickness of the interfacial layer in liquid state could be larger than previous estimate (1-5 atomic layer), because the solidified interfacial layer is around 10 atomic layers. At 10 atomic layers, the vdW attraction potential in the Fe-Nb/Al_2O_3 is reduced by 91%, from 237 zJ to 20 zJ (R=20 nm).

Chapter 6. Scalable manufacturing of oxide-dispersion strengthened (ODS) steels by liquid metallurgy

In Chapter Chapter 5, non-reactive ionocovalent oxide nanoparticles such as Al_2O_3 and Y_2O_3 are incorporated into various molten steels containing 1-1.2% Nb, since the addition of Nb greatly improved the wettability between the oxide nanoparticles and the molten steels while reducing the vdW attraction between the nanoparticles. This chapter proposes methods to fabricate ODS master alloy to enable possible scalable manufacturing of ODS steels by liquid metallurgy.

6.1. Introduction to ODS master alloy

While a melt with a good wettability to oxide prevents the oxide nanoparticles sintering by a high interfacial energy barrier, it is unable to pull apart nanoparticles that are already sintered. For metal-like nanoparticles such as WC and TiB_2 (Chapter 3 and Chapter 4), molten salts are effective vehicles to carry nanoparticles into the melt, since nanoparticles can form stable colloids without sintering in molten salts. For ionocovalent oxides, similar method is ineffective due to the reaction between oxides and molten salts. Therefore, the oxide nanoparticles are first mixed with metal micro-powders to create physical separation in order to prevent sintering before they are wetted by the melt. However, the metal micro-powder has a very low limit as to how many volume percentages of oxide nanoparticles it can carry. It was found during experiment that metal micro-powder becomes less effective when the volume percentage of oxide rises beyond 2%, in which the oxide nanoparticles start to form thick shells around the metal micro-powders that can no longer be infiltrated by the molten metal, which eventually leads to severe sintering issue during

incorporation. To this end, a more effective method to separate the oxide nanoparticles prior to incorporation are necessary.

Xu et al. proposed the concept of metal-nanoparticle superstructure, in which the microstructure changes with the volume percentage of nanoparticle [116]. At low volume percentage, the superstructure takes the form of nanoparticle-coated metal powder. At high volume percentage, the superstructure becomes networks of nanoparticles separated by metals in-between. These metal-nanoparticle superstructures can be used as masters and diluted into molten metals to manufacture MMNCs at desired nanoparticle volume percentage [116]. This method of MMNC manufacturing transforms the nanoparticle incorporation, which is normally a high-cost process, into a process that is akin to alloy-making in conventional liquid metallurgy. In conventional liquid metallurgy, necessary elements that are difficult to dissolve, dangerous to handle, or have other reasons making them not suitable for direct addition are often made into master alloy at high concentration and then diluted into the alloy melt to achieve desired composition. Elements such as B, Nb, Li, Ti, V, W, etc. all fit into this category.

For ODS steels, the ideal master alloy should contain high volume percentage of non-sintered oxide nanoparticles, in a form, such as small ingot or thin sheet, that can be easily diluted into molten steel. Currently, there is no mature technology that allows the manufacturing of bulk steel containing high volume percentage of nanoparticles. Kimura et al. demonstrated the production of Fe-24Cr-15Y_2O_3 (in wt.%), equivalent to 22 vol.% Y_2O_3, composite powders by ball milling [55]. The prolonged ball milling process induced super-heavy deformation that caused Y_2O_3 to mechanically decompose in the ferritic matrix. However, the size of Y_2O_3 nanoparticles after re-precipitation hinges upon the heat treatment temperature. An average Y_2O_3 size of 25 nm was reported if the powder is heat treated at 1000 K, but around 150 nm if the heat treated at 1600

K. As such, steel composite powders containing mechanically decomposed oxide phase is unlikely a suitable candidate to be used as master alloy for ODS steel, despite having very high concentration of oxide, because the molten steels will have temperature around 1823 K and significantly higher diffusion kinetics than solid state heat treatment. The decomposed oxide will not be able to retain a small size distribution in this condition. In addition, solid state processing route involving ball milling and hot consolidation have very high cost and requires long processing time, hence not conducive for scalable manufacturing. Majority of the ODS steel produced via this method is limited to below 0.5 vol.% of oxide nanoparticles [41], [117], [118]. Conventional liquid state processing route which needs temperature above the melting point of steel is also unable to manufacture master alloy with high oxide nanoparticle loading, due to the lack of proper incorporation method.

In this work, a novel method of manufacturing ODS master alloy with high oxide nanoparticle loading is discovered. The key to bypass the sintering issue when nanoparticle loading is high (6-10 vol.%) by the combination of three processing parameters: 1) rapid heating rate (>2000 K/s), 2) extreme melt pool temperature (>2273 K), and 3) short melting duration, for the following reasons:

1. Rapid heating allows the process to reach desired temperature in an extremely short time window (within 1 s). This means that the sintering that could have occurred during a prolonged heating stage in which the nanoparticles are not wetted can be mitigated.
2. Extreme melt pool temperature significantly enhances the wettability between the oxide and the molten steel, due to the significant reduction in solid-liquid surface tension (σ_{SL}) and liquid surface tension (σ_{LV}) [11], [111]. It also significantly increases the thermal energy (kT) available for the oxide nanoparticles to move around in the liquid.

3. Short melting duration allows the system to solidify before any sintering can happen. Nanoparticle sintering in high temperature melt is a statistical event, in which longer duration increases likelihood of sintering to occur. Therefore, a shorter melt duration is favored when manufacturing ODS master alloy with high nanoparticle loading.

The combination of these processing conditions can only be provided by extreme heat sources, such as an electrical arc or a laser beam, which are known to provide rapid heating rate and melt pool temperature as high as 4000 K [119], [120]. Therefore, ODS master alloys with high nanoparticle load are manufactured using arc melting or laser melting, in which they are referred to "arc master" or "laser master" herein.

6.2. Experimental procedure

6.2.1. ODS master alloy manufacturing

To manufacture the arc master and laser master, metal micro-powders were first mixed with oxide nanoparticles. The mixing method is consistent with that of shown in Chapter 5. For arc master, the mixed powders were cold compacted into pellets about 1 g each. The arc melting was conducted using a tungsten inert gas (TIG) welding equipment. The compacted pellet was placed in an electrically grounded pure Cu bowl for quick heat dissipation after melting. The experimental setup is shown in Figure 6.1. For arc master samples, the melting was conducted at 150 A and 16-17 V and last for 3-4 s. The solidified arc master samples were cut into metallographic samples and examined under SEM.

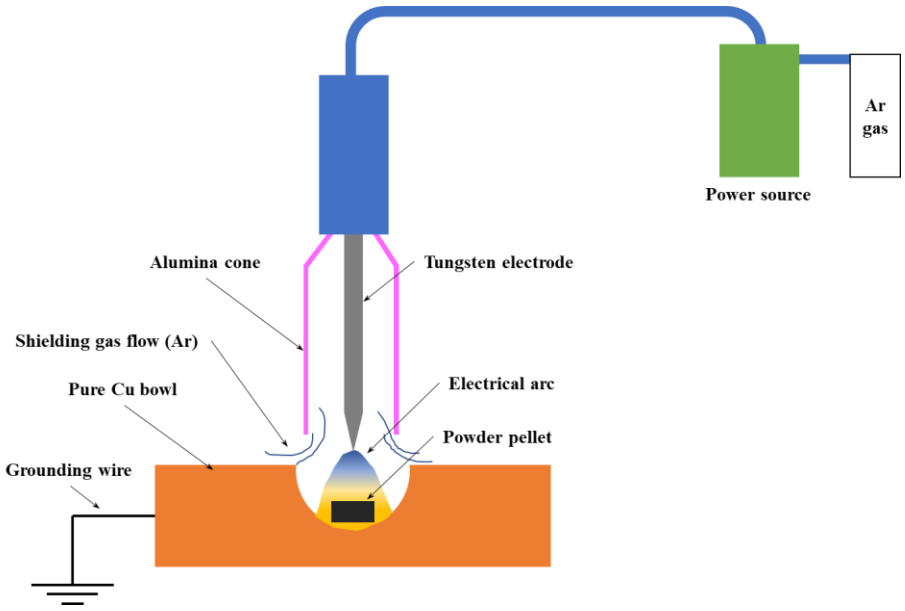

Figure 6.1: Schematic of ODS master alloy manufacturing by arc melting using a TIG welding torch.

For laser masters, the mixed powders were cold compacted into thin pellets with thickness around 1 mm. The pellet was placed in an alumina crucible. The surface of the pellet was melted with a selective laser melting (SLM) equipment, as shown in Figure 6.2. The printing chamber was purged by Ar gas. The SLM was conducted at laser power of 150 W, scanning speed of 120 mm/s and hatch space of 0.1 mm. After SLM, the pellet was submerged in ethanol and treated in an ultrasonic bath to shake loose the un-melted powders. The laser master in the form of a thin sheet was retrieved. Metallographic samples were prepared and examined under SEM.

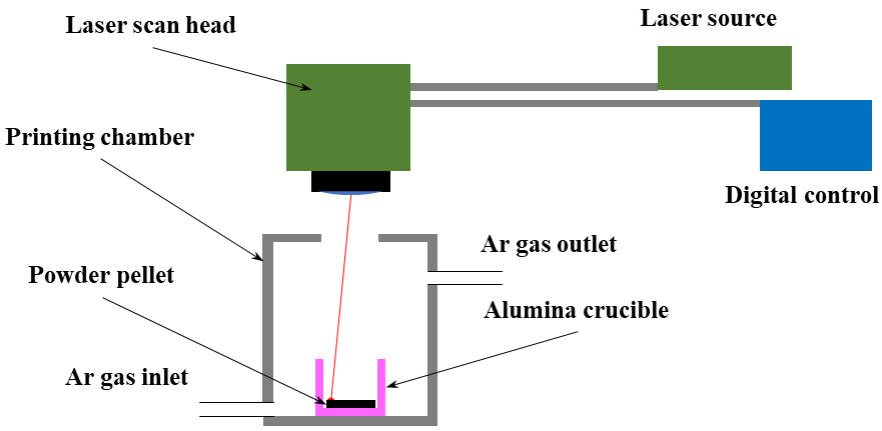

Figure 6.2: Schematic of ODS master alloy manufacturing by selective laser melting.

6.2.2. Dilution experiment using ODS master alloy

To verify the effect of the ODS master alloys, they were diluted into various molten steels. A steel with desired composition was melted at 1560 ˚C under Ar atmosphere. The melt contained 1 wt.% of Nb to improve its wettability with the oxide nanoparticles. Stirring was applied to promote the uniform mixing of the Nb in the melt. The ODS master alloy, either in the form small ingot (arc master) or thin sheet (laser master) was added to the molten steel at calculated ratio; this ratio is referred to as “dilution ratio” (DR) herein. Stirring was applied to promote the dissolution of the ODS master, and the uniform mixing of the oxide nanoparticles. The furnace was then turned off, allowing the molten steel to solidify slowly (cooling rate < 5 K/s). The parameters used the control the dilution experiment are summarized in Table 11. The percentage of oxide nanoparticle in the master alloy (W_M or V_M) is related to the final oxide percentage in the ODS steel after dilution by a simple factor of DR+1. The as cast ODS steel samples were prepared into metallographic samples for SEM examination. The Vickers hardness of each sample was measured.

Series of control experiments were conducted using the same procedure, however the master alloy used in the control experiments were blanks, which contained no oxide nanoparticles.

Table 11: Weight-based and volume-based parameters used in the dilution experiments of ODS master alloys.

Parameter	Weight-based	Volume-based
Oxide nanoparticle percentage in the master (W_M or V_M)	$W_M\% = \frac{wt_{oxide}}{wt_{oxide} + wt_{metal}}$ $wt_{oxide} + wt_{metal} = wt_{master}$	$V_M\% = \frac{V_{oxide}}{V_{oxide} + V_{metal}}$ $V_{oxide} + V_{metal} = V_{master}$
Final oxide percentage (W_F or V_F)	$W_F\% = \frac{wt_{oxide}}{wt_{master} + wt_{base\ metal}}$	$V_F\% = \frac{V_{oxide}}{V_{master} + V_{base\ metal}}$
Dilution ratio (DR)	$DR = \frac{wt_{base\ metal}}{wt_{master}}$	
Relation	$W_F\% = \frac{W_M\%}{DR + 1}$	$V_F\% = \frac{V_M\%}{DR + 1}$

6.3. **Results**

6.3.1. Microstructure of the arc masters

Two different matrix compositions were used to manufacture the arc master samples, Fe7Mn1Nb1C1Si and Fe1Nb (in wt.%). Fe7Mn1Nb1C1Si is a medium Mn steel (MMS) that is suitable for dilution to achieve the desired composition of other carbon steels due to its relative high concentration of C (1%) and Mn (7%). Fe1Nb is a simple binary alloy that can be diluted in other low-alloyed steels and stainless steel, since it does not impact the overall composition significantly if a high DR value is used. Y_2O_3 nanoparticle (APS 10 nm) was selected due to its prevalence in literature work. For each matrix composition, arc master samples with two different

Y_2O_3 nanoparticle loading were made, 4 and 6.8 wt.%, equivalent to 6 and 10 vol.%, respectively. The microstructures of as-solidified Fe7Mn1Nb1C1Si-4Y_2O_3 ODS and -6.8Y_2O_3 ODS master alloy are shown in Figure 6.3. For both oxide loading levels (4 and 6.8%), the Y_2O_3 nanoparticles are uniformly dispersed in the matrix. Particle size data is acquired after image processing for the high magnification micrographs (Figure 6.3 (b) and (e)). The APS is 11.6 and 9.7 nm for the 4 and 6.8% Y_2O_3 sample, respectively.

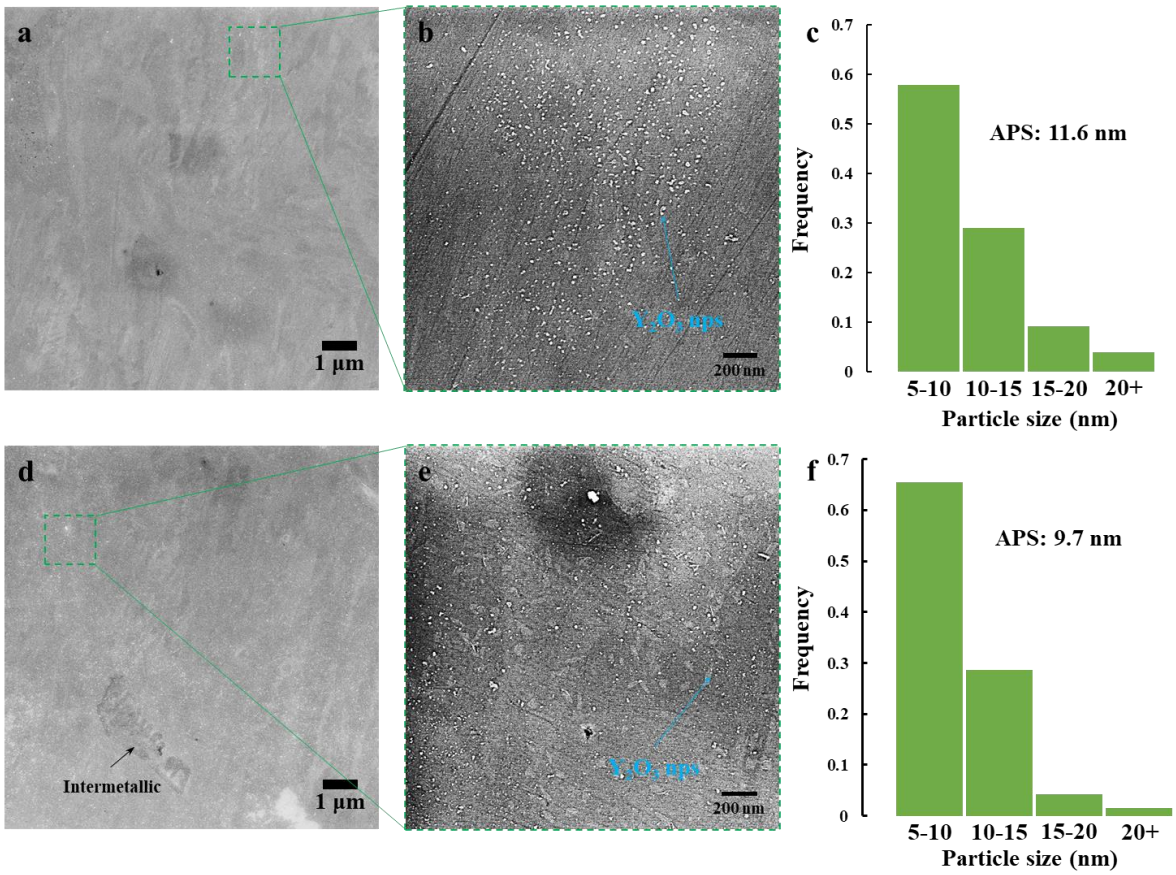

Figure 6.3: (a) SEM micrograph of as-solidified Fe7Mn1Nb1C1Si-4Y_2O_3 ODS master alloy and (b) zoomed-in view of selected area, (c) size distribution of the Y_2O_3 nanoparticles in (b). (d) SEM micrograph of as-solidified Fe7Mn1Nb1C1Si-6.8Y_2O_3 ODS master alloy and (e) zoomed-in view of selected area, (f) size distribution of the Y_2O_3 nanoparticles in (e).

The microstructures of as-solidified Fe1Nb-4Y_2O_3 and -6.8Y_2O_3 ODS master alloy are shown in Figure 6.4. For both samples, sub-micron Fe_2O_3 inclusions are observed in the matrix (Figure 6.4 (a) and (d)). In the Fe7Mn1Nb1C1Si samples, these inclusions are not observed. Comparatively, Fe7Mn1Nb1C1Si sample contains high concentration of C, that can sacrificially burn before other element is oxidized in the arc melting process, while Fe1Nb sample does not contain sacrificial element that can prevent Fe from oxidizing. Therefore, the oxygen contamination during the short melting window resulted in the formation of these sub-micro Fe_2O_3 inclusions. However, the presence of these inclusions does not affect the uniform dispersion of Y_2O_3 nanoparticles (Figure 6.4 (b) and (e)). The APS is 11.5 and 12.3 nm for the 4 and 6.8% Y_2O_3 sample, respectively.

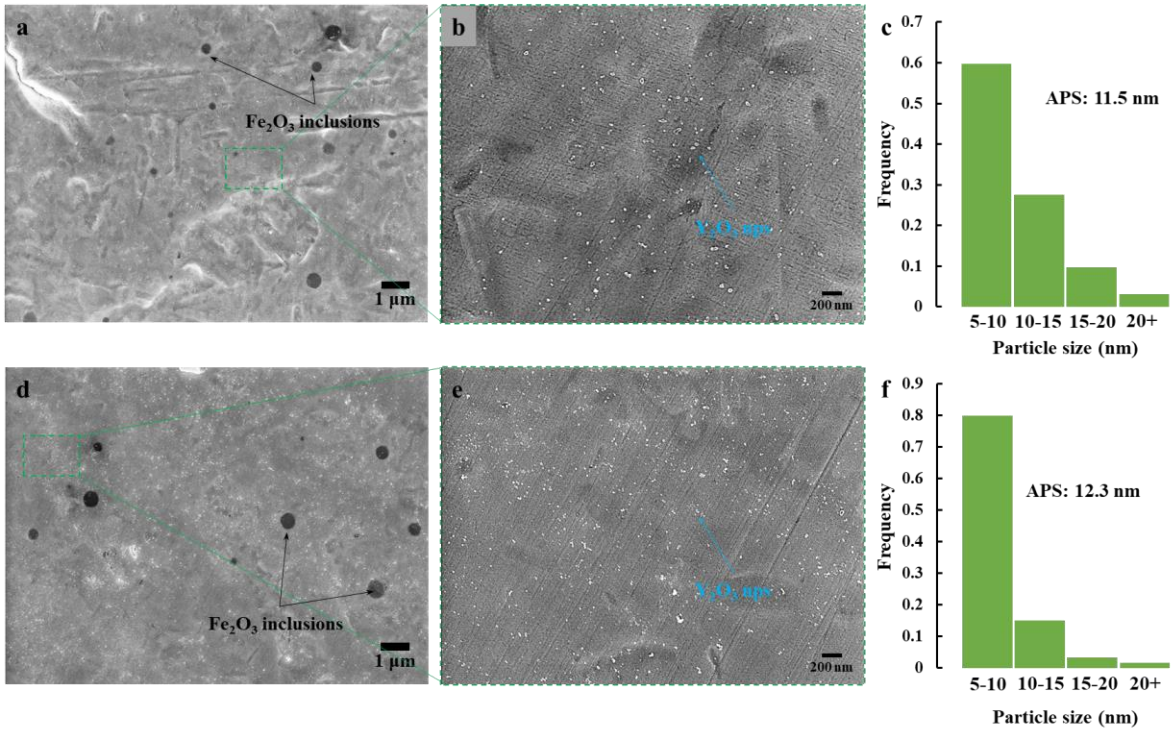

Figure 6.4: (a) SEM micrograph of as-solidified Fe1Nb-4Y_2O_3 ODS master alloy and (b) zoomed-in view of selected area, (c) size distribution of the Y_2O_3 nanoparticles in (b). (d) SEM

micrograph of as-solidified Fe1Nb-6.8Y_2O_3 ODS ODS master alloy and (e) zoomed-in view of selected area, (f) size distribution of the Y_2O_3 nanoparticles in (e).

6.3.2. Microstructure of the laser masters

For laser masters, the matrix composition is Fe7Mn1Nb1C1Si. Y_2O_3 nanoparticle (APS 40-50 nm) was used. Samples with two different Y_2O_3 nanoparticle loadings were prepared, 4 and 6.8 wt.%, equivalent to 6 and 10 vol.%. The microstructures of the as-printed Fe7Mn1Nb1C1Si-4Y_2O_3 and -6.8Y_2O_3 ODS master alloy are shown in Figure 6.5. At low magnification, the laser masters have a distinct two-phase feature, with the matrix having dark contrast and the Y_2O_3 having light contrast. The Y_2O_3 phase distribution strongly resembles that of the laser raster pattern during SLM process. The Y_2O_3 nanoparticles are found in highly concentrated pseudo-clusters (Figure 6.5 (b), (d)). High magnification view (Figure 6.5 insets) suggests that the Y_2O_3 nanoparticles are well-dispersed inside the pseudo-clusters and no sintering is observed. However, the high density of nanoparticles in these regions resulted in the image processing tool being unable to distinguish one nanoparticle from its neighbors. Therefore, particle size statistics cannot be generated. Instead, twenty nanoparticles from the insets of Figure 6.5 (b) and (d) are randomly selected and measured. The APS is 41.3±4.7 nm and 40.7±10.7 nm for the 4 and 6.8% Y_2O_3 sample, respectively.

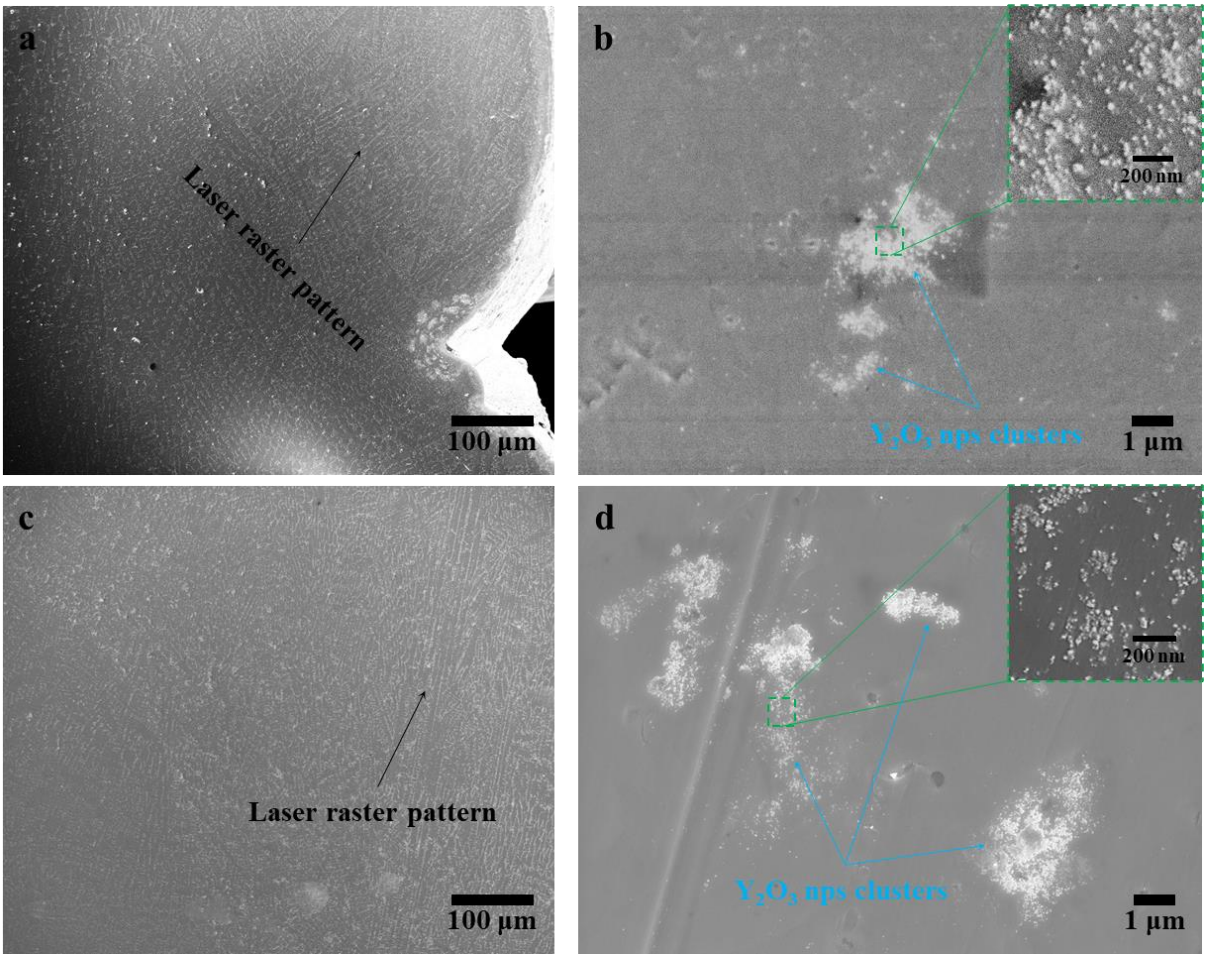

Figure 6.5: (a) and (b) SEM micrograph of as-printed Fe7Mn1Nb1C1Si-4Y_2O_3 ODS master alloy; (c) and (d) SEM micrograph of as-printed Fe7Mn1Nb1C1Si-6.8Y_2O_3 ODS master alloy.

6.3.3. Microstructure ODS low carbon steel

ODS low carbon steels were produced by diluting the ODS master alloy in a melt with fixed chemical composition. Different DR values were used to control the Y_2O_3 nanoparticle percentage as well as the chemical composition in the final steel. The combination of these parameters is summarized in Table 12. The microstructures of the as-cast ODS low carbon steels are shown in Figure 6.6.

Table 12: Parameters used to produce ODS low carbon steels shown in Figure 6.6.

	Steel base composition (wt.%)	ODS master alloy type	ODS master alloy composition (wt.%)	DR	Designed final composition (wt.%)
Figure 6.6 (a)	Fe1.2Nb0.2Mn0.1C	Arc master	Fe7Mn1Nb1C1Si-6.8Y_2O_3 (Y_2O_3 APS 9.7 nm)	**21**	Fe1.2Nb0.5Mn0.14C0.04Si-0.32Y_2O_3
Figure 6.6 (b)	Fe1.2Nb0.2Mn0.1C	Laser master	Fe7Mn1Nb1C1Si-6.8Y_2O_3 (Y_2O_3 APS 40.7 nm)	**21**	Fe1.2Nb0.5Mn0.14C0.04Si-0.32Y_2O_3
Figure 6.6 (c)	Fe1.2Nb0.2Mn0.1C		Fe7Mn1Nb1C1Si-4Y_2O_3 (Y_2O_3 APS 41.3 nm)	**9**	Fe1.2Nb0.88Mn0.19C0.1Si-0.41Y_2O_3

The primary goal of conducting the dilution experiment is to validate that the oxide nanoparticles can retain a stable self-dispersion after being diluted from high concentration, when in ODS master, to low concentration, when in a steel melt with no nanoparticles. This goal is achieved both using arc master and laser master. The arc master contains very fine Y_2O_3 nanoparticles (APS 9.7 nm), after diluting at DR=21, the resulting ODS low carbon steel is shown in Figure 6.6 (a.1) and (a.2). The nanoparticles remained individually dispersed. The APS for this sample was 18.2 nm. However, due to the low volume fraction (0.5 vol.%) and small particle size, the imaging process was challenging. Some very small nanoparticles do not have sufficient contrast to be distinguished from the matrix, which potentially contributed the increase in APS. The laser master contains larger Y_2O_3 nanoparticles (APS ~40 nm) that are significantly easier to observe after dilution. For samples with DR=9 and 21, as shown in Figure 6.6 (a.1-2) and (b.1-2), majority of the nanoparticles are individually dispersed, while a few nanoparticles appear to be sintered (Figure 6.6 (a.2)). The nanoparticles also retained their size comparing to their as

purchased condition (APS 40-50 nm), as printed condition (APS ~40 nm), and finally as cast condition (APS 40-45 nm).

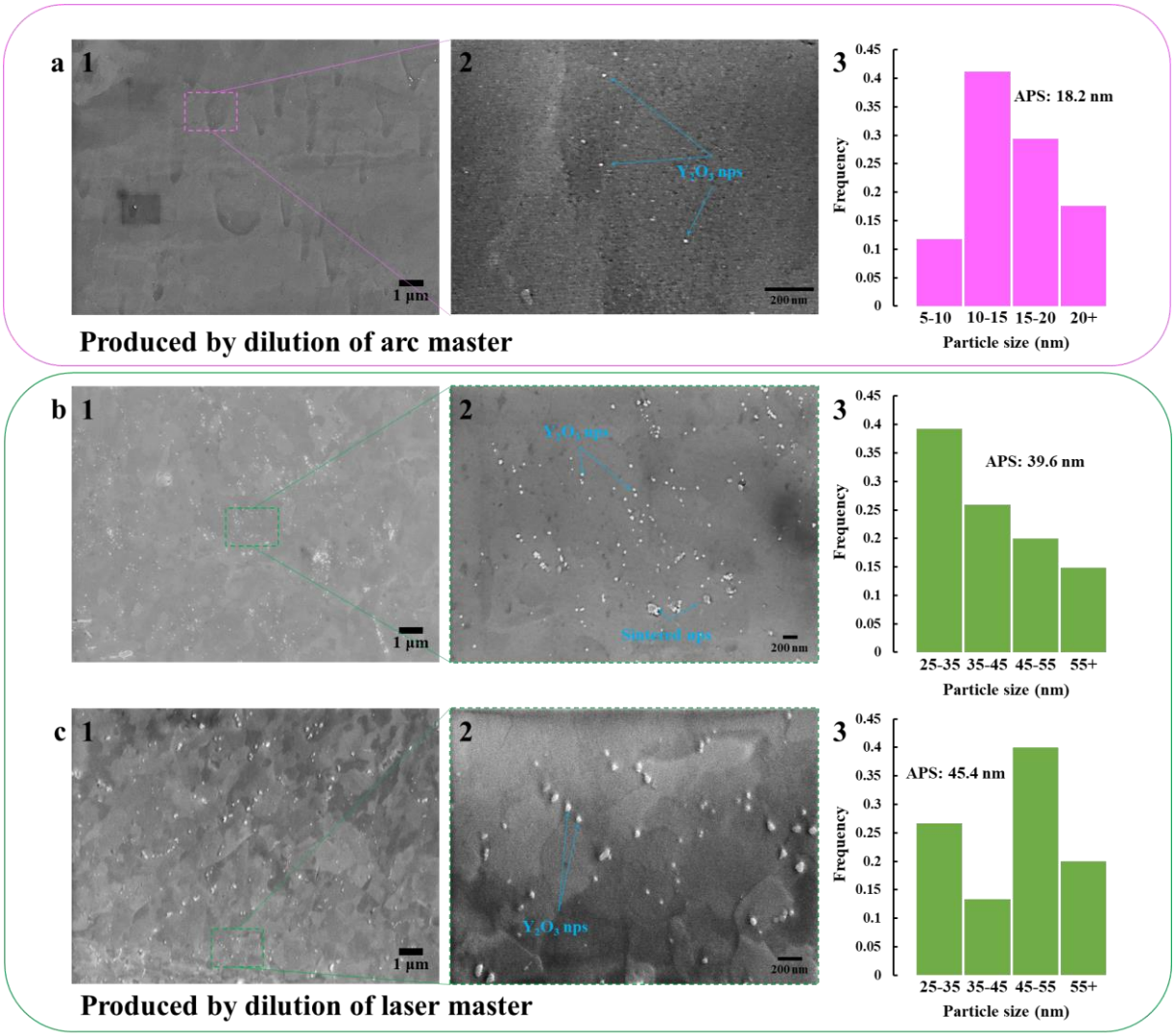

Figure 6.6: SEM micrographs of as-cast ODS low carbon steels: (a.1) Fe1.2Nb0.5Mn0.14C0.04i-0.32Y_2O_3 produced by dilution of arc master containing 6.8% Y_2O_3, (a.2) zoomed-in view of the nanoparticles of selected area in (a.1), and (a.3) particle size distribution of (a.2). (b.1) Fe1.2Nb0.5Mn0.14C0.04i-0.32Y_2O_3 produced by dilution of laser master containing 6.8% Y_2O_3, (b.2) zoomed-in view of the nanoparticles of selected area (b.1), and (b.3) particle size distribution of (b.2). (c.1) Fe1.2Nb0.88Mn0.19C0.1Si-0.41Y_2O_3 produced by dilution of laser

master containing 4% Y_2O_3, (c.2) zoomed-in view of the nanoparticles of selected area (c.1), and (c.3) particle size distribution of (c.2).

6.3.4. Microstructure of ODS stainless steel

ODS stainless steels were produced by diluting the ODS master alloy in a commercial 316L melt modified with 1 wt.%Nb. The ODS master alloy used in this experiment were Fe1Nb-6.8Y_2O_3 with smaller Y_2O_3 nanoparticles for arc master (APS 12.3 nm) and larger Y_2O_3 nanoparticles for laser master (APS 50.0 nm). The combination of these parameters is summarized in Table 13. The microstructures of the as-cast ODS stainless steels are shown in Figure 6.7.

Table 13: Parameters used to produce ODS low carbon steels shown in Figure 6.7.

	Steel base composition (wt.%)	ODS master alloy type	ODS master alloy composition (wt.%)	DR	Designed final composition (wt.%)
Figure 6.7 (a)	316L-1Nb	Arc master	Fe1Nb-6.8Y_2O_3 (Y_2O_3 APS 12.3 nm)	**47**	316L-1Nb-0.14Y_2O_3
Figure 6.7 (b)	316L-1Nb	Laser master	Fe1Nb-6.8Y_2O_3 (Y_2O_3 APS 50.0 nm)	**47**	316L-1Nb-0.14Y_2O_3

Stainless steel 316L is a highly alloyed steel that contains over 33 wt.% of alloying elements. Therefore, when diluting the Fe1Nb-6.8Y_2O_3 master alloy, the DR was deliberately set to a high value of 47, for the purpose of preventing the excess dilution of the remaining alloying elements such as Cr and Ni. Similar to the nanoparticle dispersion observed in the ODS low carbon steels (Figure 6.6), the Y_2O_3 nanoparticles are also individually dispersed in the ODS stainless steel, as shown in Figure 6.7 (a.1-2) and (b.1-2). The arc master contains smaller Y_2O_3 nanoparticles, while the laser master contains larger ones. After dilution, the different sizes of

Y_2O_3 nanoparticles are able to disperse equally well. Based on the particle size analysis, the nanoparticles retained their size from as purchased condition throughout the process.

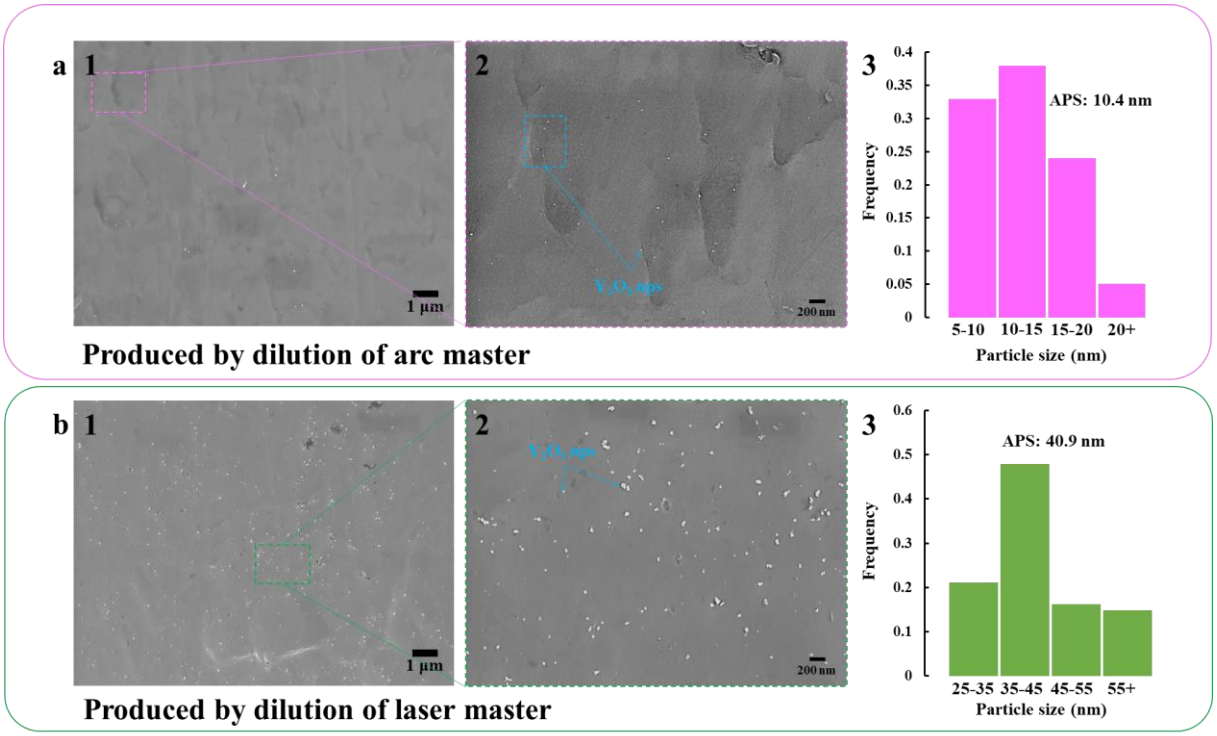

Figure 6.7: SEM micrographs of as-cast ODS stainless steels: (a.1) 316L-1Nb-0.14Y_2O_3 produced by dilution of arc master containing 6.8% Y_2O_3, (a.2) zoomed-in view of the nanoparticles of selected area (a.1), and (a.3) particle size distribution of (a.2). (b.1) 316L-1Nb-0.14Y_2O_3 produced by dilution of laser master containing 6.8% Y_2O_3, (b.2) zoomed-in view of the nanoparticles of selected area (b.1), and (b.3) particle size distribution of (b.2).

6.3.5. Hardness of ODS low carbon steel and stainless steel

The Vickers hardness of as-cast ODS low carbon steel (LCS) and ODS stainless steel 316L are shown in Figure 6.8. For each ODS sample, the hardness of a reference sample that contains no nanoparticles, while manufactured in otherwise identical method, is also shown for comparison.

The LCS 1 reference sample has a hardness of 152 HV. The two ODS variants of LCS 1, one produced by diluting the arc master and the other by laser master, have hardness of 149 and 172 HV, respectively. Despite being designed at the same 0.32% of Y_2O_3 nanoparticles, the ODS LCS 1 produced by laser master has noticeably higher hardness. This is primarily due to the carbon loss during the manufacturing of the master alloys. The matrix of the master alloys contains 1% carbon. The arc master was produced by the electrical arc from a TIG welding torch, as shown in Figure 6.1. The Ar shielding gas was blew onto the melting pool from an alumina cone. The lack of enclosure in this experimental setup led to higher level of oxygen contamination and carbon burning. Comparatively, the laser master was produced in a semi-enclosed printing chamber, as shown Figure 6.2. In this setup, the Ar shielding gas flew through the chamber from one end and exiting from the other, creating a more stable atmosphere to reduce carbon burning. The LCS 1 reference sample has a hardness of 225 HV. The ODS LCS 2 sample has a hardness of 255 HV. The hardness increment is roughly equal to 7 HV gain per 0.1 wt.% Y_2O_3 for both ODS LCS 1 and LCS 2 produced by laser master.

For the stainless steel samples (Figure 6.8 (b)), the addition of 1% Nb by itself provides no tangible hardness increase: 155 HV for 316L-0Nb vs. 158 HV for 316L-1Nb. Drastic hardness increase is found in both ODS samples with 0.14%Y_2O_3. The ODS sample produced by laser master sees a hardness gain of 60 HV (43 HV gain per 0.1% Y_2O_3) with larger Y_2O_3 nanoparticles, while the ODS sample produced by arc master sees a hardness gain of 82 HV (58HV gain per 0.1% Y_2O_3) with smaller Y_2O_3 nanoparticles. In this case, the master alloy is Fe1Nb-6.8Y_2O_3, containing no combustible alloying elements. Despite Fe_2O_3 inclusions were formed in the arc master (Figure 6.4 (d)), they did not affect the dispersion of the Y_2O_3 nanoparticles.

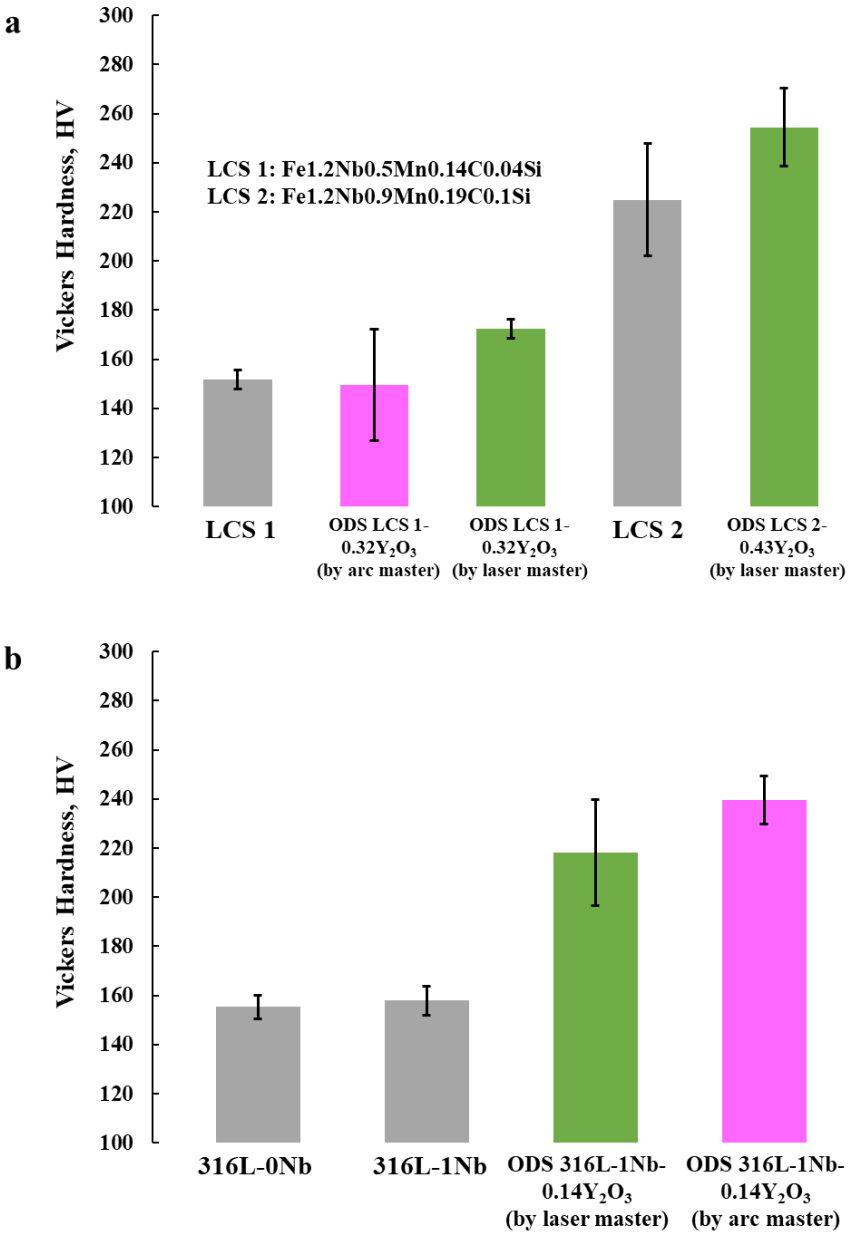

Figure 6.8: Vickers hardness of as-cast (a) low carbon steel (LCS) blank references (LCS 1 and LCS 2) and ODS LCSs, (b) stainless steel 316L blank references and ODS 316L.

6.4. **Discussion**

An electrical arc and a laser beam are two comparable heat sources. Both of them are capable of delivering rapid heating rate and extreme temperature. However, despite the similarity, the microstructure of the ODS master alloy produced using these two methods have very different microstructures. On one hand, the arc masters (Figure 6.3 and Figure 6.4) have no observable segregation issue between the oxide nanoparticles and the matrix. The oxide nanoparticles are uniformly dispersed throughout the matrix. On the other hand, the laser masters (Figure 6.5) have very obvious segregation between the oxide phase and the matrix, in which the oxide phase shows alignment matching the laser raster pattern. The oxide nanoparticles are dispersed in highly particle-dense pseudo-clusters. The difference between the microstructure is due the presence (or the lack thereof) of "global" melting. During the manufacturing of the arc masters, the powder pellet was entirely melted, hence "global", by the arc and was held at liquid state for 2-3 s before solidification. The global melting significantly improves the dispersion of the nanoparticles, because of the strong Brownian motions. For laser masters, the powder pellet was never entirely melted, hence lacking "global" melting, due to the limitation of the laser spot size. Therefore, the melt pool size was much smaller, limiting the volume in which nanoparticle can travel. In addition, due to the constant scanning motion of the laser, the melt pool was held at liquid state for only a short duration at each location before moving on to the next location, whereas the entire pellet was held in liquid state for 2-3 s for the arc masters. As such, the oxide nanoparticles in the laser masters are confined in pseudo-clusters, as they were unable to disperse beyond the small volume of the melt pool created by the laser. Despite having different quality of nanoparticle dispersion, the dilution experiments found little difference in the final microstructures. Both arc and laser masters are capable of being used to produce ODS steels with uniform nanoparticle dispersion. The

nanoparticle size remains largely unchanged in the as-cast ODS steels comparing to in the as-purchased condition.

Due to the difference in experimental setup between the arc melting and SLM process, the master alloys were affected by oxygen contamination differently. The arc masters, despite showing the better nanoparticle dispersion, suffered from carbon burning, which resulted in the lower hardness value after dilution, comparing to the sample with the same designed composition but produced using laser master. If combustible alloying elements are not present in the master, such as the case of Fe1Nb-6.8Y_2O_3, then oxygen does not affect the quality of the arc master. To this end, if the gas protection can be further improved in the arc melting setup, then the arc master would be able to retain its combustible alloying elements while providing better nanoparticle dispersion.

Manufacturing ODS steel by liquid metallurgy technique discovered in this work has significant potential in reducing the manufacturing cost. In the conventional P/M-based manufacturing technique, as shown in Figure 6.9 (top), the requirement of hot consolidation limits the geometry of the semi-finished ODS steel product to mostly rods, slabs, and tubes. Hot consolidation is also a highly costly process (up to 80 $/lb). The semi-finished ODS steel products can cost 200-400 $/lb [121]. In the novel liquid metallurgy-based technique, as shown in Figure 6.9 (bottom), the requirement of hot consolidation is removed. The oxide nanoparticles can added and dispersed in liquid steel. The subsequent casting process allows for the liquid steel to be cast into regular billet or other designed shapes. As such, the manufacturing duration is shortened, and the cost is significantly reduced.

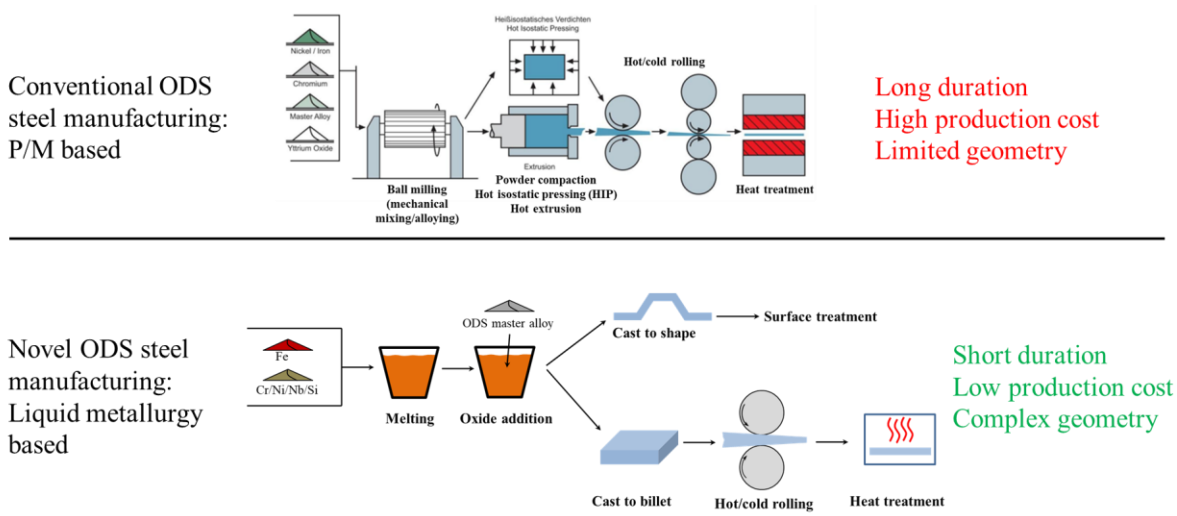

Figure 6.9: Schematics of (top) conventional ODS steel manufacturing with P/M-based technique, and (bottom) novel ODS steel manufacturing with liquid metallurgy-based technique in this work.

6.5. **Conclusions**

This chapter presents a potential scalable manufacturing process for ODS steels by liquid metallurgy. High concentration of oxide nanoparticles is first incorporated and dispersed into a steel matrix by arc melting or SLM, producing the ODS master alloys. The ODS master alloys are then diluted into a steel melt at a high dilution ratio, releasing the oxide nanoparticles. Due to the presence of Nb in the steel melt, the oxide nanoparticles are able to wet with the melt and disperse uniformly. This work validates the theoretical and experimental study presented in Chapter 81Chapter 5: 1. the wettability between the oxide nanoparticle and the melt can be improved to prevent sintering, and 2. the vdW attraction between the nanoparticles can be reduced to promote uniform dispersion. Despite having an initial high cost of producing the ODS master alloys using arc melting or SLM, the final cost is offset by the dilution ratio. When DR is 10, the master alloy

only contributes to less than 10% of the final ODS cost. When DR is 50, the master alloy is only less than 2% of the final ODS cost.

Chapter 7. Conclusions

This PhD research is motivated by the fundamental challenge for the manufacturing of Fe-based MMNCs by liquid metallurgy: the trade-off between the wettability and the thermodynamic stability of the nanoparticle in Fe matrix. The conventional methods of tackling this trade-off either eliminate the presence of liquid phase by using solid state processes or significantly reduce the time factor in the process by using rapid solidification techniques. These conventional methods face strong obstacles in their scalability due to high cost and low production volume. It was therefore motivating to explore a new method of tackling the trade-off between wettability and stability.

The first system explored in this research was Fe-36Ni Invar alloy and WC. WC is a metal-like ceramic that has many metallic features such as high thermal and electrical conductivity. WC also has very high wettability with Fe, hence making it a suitable candidate for tackling the trade-off by reducing its reactivity with Fe. It was found that purely relying on the reduction of temperature was ineffective in suppressing the reactivity. Only when the processing temperature dropped to 130 ˚C below the melting point, the reactivity can be reasonable managed. However, despite being unable to produce Invar/WC MMNC using liquid metallurgy, the solid state processing route yielded strong mechanical properties and unique thermal expansion property.

The second system explored in this research was Fe-Ti-B high modulus steel. TiB_2 is a light and stiff material. Akin to WC, TiB_2 is also a metal-like ceramic that has good wettability with Fe. Therefore, incorporating TiB_2 into Fe matrix can reduce the density of the steel while increase its stiffness. However, the large solubility of TiB_2 in Fe matrix means directly adding TiB_2 nanoparticle into molten Fe would be ineffective because of the dissolution. Therefore, we attempted to suppress the reactivity by first saturate the melt with Ti and B until the eutectic

composition, and then add a small amount of TiB_2, which pushed the overall composition to hypereutectic. This process resulted in a unique solidification behaviour and a microstructure that has not been reported in literature. The resulting Fe-Ti-B high modulus steel had high mechanical strength and stiffness, while maintaining the ductility. This is a successful demonstration of the suppression of reactivity by chemically altering the dissolution kinetics. However, this method to overcome the trade-off between the wettability and the thermodynamic stability is complicated and non-universal.

Since improving the stability of a nanoparticle with high wettability was very difficult to achieve in liquid metallurgy, the research went on to address the other side of this trade-off: improving the wettability of a nanoparticle with low wettability but high stability. Ionocovalent oxides represent some of the most thermodynamically stable ceramics. Their incorporation into molten steel is a longstanding challenge for decades, due to the lack of wettability. First, theoretical modeling was used to study the effect of alloying element such as Si, Mn, Cr, and Nb on the wettability between molten Fe and oxides. It was found that Cr is effective in improving the wettability at high concentrations (such as in stainless steel), while Nb is effective even in low concentration. In addition to the effect on wettability, Cr and Nb were also examined on their effect to reduce the vdW attraction between nanoparticles. It was found solute (Cr or Nb) enriched interfacial liquid layer around oxide nanoparticles can significantly reduce the vdW attraction by screening effect. Simple experiments were conducted, and the theoretical prediction on the wettability was validated. Regions with enriched Nb content was also found to form around oxide nanoparticles, indicating the presence of enriched interfacial liquid layer prior to solidification.

Finally, scalable manufacturing processes for ODS steels by liquid metallurgy was experimented. The key to this process was the manufacturing of an ODS master alloy with high

concentration and uniformly dispersed of oxide nanoparticles. The ODS master alloys were successfully produced using rapid heating method such as arc melting and SLM. The ODS master alloys were then diluted into a steel melt containing Nb. The highly concentrated oxide nanoparticles in the master alloys were able to disperse in the steel melt, producing the final ODS steel. This process is highly robust and versatile because it was experimentally proven in both stainless steels and low carbon steels, two of the most heavily used steel categories.

In summary, this work has successfully addressed the fundamental challenge for the manufacturing of Fe-based MMNCs by liquid metallurgy. For the first time, oxide nanoparticles can be incorporated and uniformly dispersed in molten steels, which enables the ODS steels to be produced via slow-cooling liquid metallurgy. This study, therefore, paves the way for the scalable manufacturing of various types of cast ODS steels with complex geometries, allowing ODS steels to be used in wide ranging applications.

Chapter 8. Recommendations for future work

1. The effect of oxide nanoparticles on the solidification, grain growth and grain size of molten steel

Uniformly dispersed nanoparticles in molten metal are known to have significant effect on the solidification behaviour and solidified microstructure. Previously, oxide nanoparticles cannot be incorporated and dispersed in molten steel. With the new methods demonstrated in this work, the effect of oxide nanoparticles on the solidification behaviour can be studied, as grain growth and secondary phase formation can be affected, both of which are very important for the property of the steel.

2. Effect of oxide nanoparticles on thermomechanical treatments of steels

Thermomechanical treatments are vital for the manufacturing of steels. Through the process such as hot forging, hot rolling, cold rolling, and heat treatment, steels can be shaped into desired geometries, and their mechanical properties can be adjusted to fit the application requirement. The presence well-dispersed oxide nanoparticles can change the steels' response to hot/cold plastic deformation, the dissolution and precipitation of secondary phase during heat treatment, and the refinement, growth, or recrystallization of the grains.

3. Effect of oxide nanoparticles on mechanical properties

Conventional ODS steels, which are produced by powder metallurgy, have high mechanical strength, creep resistance, and irradiation resistance comparing to their un-reinforced counterpart. With the proposed methods in this work, ODS steels can be manufactured by liquid metallurgy. The mechanical properties of the ODS steels produced by liquid metallurgy should be studied at

both room and elevated temperatures. Comparison can be made between the conventional ODS steels and the novel ODS steels.

Reference

[1] R. E. Hummel, *Understanding Materials Science*. Springer-Verlag New York, 2004.

[2] D. Embury and O. Bouaziz, *Steel-Based Composites: Driving Forces and Classifications*, vol. 40, no. 1. 2010.

[3] O. D. Sherby and J. Wadsworth, "Ancient blacksmiths, the Iron Age, Damascus steels, and modern metallurgy," *J. Mater. Process. Technol.*, vol. 117, no. 3, pp. 347–353, 2001, doi: 10.1016/S0924-0136(01)00794-4.

[4] J. Wadsworth and O. D. Sherby, "On the Bulat-Damascus steels revisited," *Prog. Mater. Sci.*, vol. 25, no. 1, pp. 35–68, 1980, doi: 10.1016/0079-6425(80)90014-6.

[5] F. Akhtar, "Ceramic reinforced high modulus steel composites: Processing, microstructure and properties," *Can. Metall. Q.*, vol. 53, no. 3, pp. 253–263, 2014, doi: 10.1179/1879139514Y.0000000135.

[6] L. Ceschini *et al.*, *Aluminum and Magnesium Metal Matrix Nanocomposites*. Springer, 2017.

[7] R. Casati and M. Vedani, "Metal matrix composites reinforced by Nano-Particles—A review," *Metals (Basel).*, vol. 4, no. 1, pp. 65–83, 2014, doi: 10.3390/met4010065.

[8] H. Springer, C. Baron, A. Szczepaniak, V. Uhlenwinkel, and D. Raabe, "Stiff, light, strong and ductile: nano-structured High Modulus Steel," *Sci. Rep.*, vol. 7, no. 1, pp. 17–22, 2017, doi: 10.1038/s41598-017-02861-3.

[9] H. Zhang, H. Springer, R. Aparicio-Fernandez, and D. Raabe, "Improving the mechanical properties of Fe-TiB2 high modulus steels through controlled solidifi cation processes," *Acta Mater.*, vol. 118, pp. 187–195, 2016.

[10] L. Y. Chen *et al.*, "Processing and properties of magnesium containing a dense uniform dispersion of nanoparticles," *Nature*, vol. 528, no. 7583, pp. 539–543, 2015, doi: 10.1038/nature16445.

[11] N. Eustathopoulos & M.G. Nicholas & B., *Wettability at High Temperatures, 1st Edition*. 1999.

[12] B. AlMangour, D. Grzesiak, and J. M. Yang, “In-situ formation of novel TiC-particle-reinforced 316L stainless steel bulk-form composites by selective laser melting,” *J. Alloys Compd.*, vol. 706, pp. 409–418, 2017, doi: 10.1016/j.jallcom.2017.01.149.

[13] B. AlMangour, D. Grzesiak, and J. M. Yang, “Selective laser melting of TiB2/316L stainless steel composites: The roles of powder preparation and hot isostatic pressing post-treatment,” *Powder Technol.*, vol. 309, pp. 37–48, 2017, doi: 10.1016/j.powtec.2016.12.073.

[14] S. K. Karak, J. Dutta Majumdar, Z. Witczak, W. Lojkowski, and I. Manna, “Microstructure and mechanical properties of nano-Y2O3 dispersed ferritic alloys synthesized by mechanical alloying and consolidated by hydrostatic extrusion,” *Mater. Sci. Eng. A*, vol. 580, pp. 231–241, 2013, doi: 10.1016/j.msea.2013.04.085.

[15] S. Ukai, S. Ohtsuka, T. Kaito, Y. de Carlan, J. Ribis, and J. Malaplate, “Oxide dispersion-strengthened/ferrite-martensite steels as core materials for Generation IV nuclear reactors,” in *Structural Materials for Generation IV Nuclear Reactors*, Elsevier Ltd, 2017, pp. 357–414.

[16] D. Hull and D. J. Bacon, *Introduction to dislocations*, 5th ed. Butterworth-Heinemann, 2011.

[17] Z. Zhang and D. L. Chen, “Contribution of Orowan strengthening effect in particulate-reinforced metal matrix nanocomposites,” *Mater. Sci. Eng. A*, vol. 483–484, no. 1-2 C, pp. 148–152, 2008, doi: 10.1016/j.msea.2006.10.184.

[18] A. Sanaty-Zadeh, “Comparison between current models for the strength of particulate-reinforced metal matrix nanocomposites with emphasis on consideration of Hall-Petch effect,” *Mater. Sci. Eng. A*, vol. 531, pp. 112–118, 2012, doi: 10.1016/j.msea.2011.10.043.

[19] Z. Li, K. G. Pradeep, Y. Deng, D. Raabe, and C. C. Tasan, “Metastable high-entropy dual-phase alloys overcome the strength-ductility trade-off,” *Nature*, vol. 534, no. 7606, pp. 227–230, 2016, doi: 10.1038/nature17981.

[20] R. O. Ritchie, “The conflicts between strength and toughness,” *Nat. Mater.*, vol. 10, no. 11, pp. 817–822, 2011, doi: 10.1038/nmat3115.

[21] S. F. Corbin and D. S. Wilkinson, “The influence of particle distribution on the mechanical response of a particulate metal matrix composite,” *Acta Metall. Mater.*, vol. 42, no. 4, pp.

1311–1318, 1994, doi: 10.1016/0956-7151(94)90147-3.

[22] B. Gao *et al.*, "Ultrastrong low-carbon nanosteel produced by heterostructure and interstitial mediated warm rolling," *Sci. Adv.*, vol. 6, no. 39, pp. 1–8, 2020, doi: 10.1126/sciadv.aba8169.

[23] S. F. Corbin and D. S. Wilkinson, "Low strain plasticity in a particulate metal matrix composite," *Acta Metall. Mater.*, vol. 42, no. 4, pp. 1319–1327, 1994, doi: 10.1016/0956-7151(94)90148-1.

[24] L. Ceschini *et al.*, "Metal Matrix Nanocomposites: An Overview," pp. 1–17, 2017, doi: 10.1007/978-981-10-2681-2_1.

[25] G. Liu *et al.*, "Nanostructured high-strength molybdenum alloys with unprecedented tensile ductility," *Nat. Mater.*, vol. 12, no. 4, pp. 344–350, 2013, doi: 10.1038/nmat3544.

[26] E. Pagounis and V. K. Lindroos, "Processing and properties of particulate reinforced steel matrix composites," *Mater. Sci. Eng. A*, vol. 246, no. 1–2, pp. 221–234, 1998, doi: 10.1016/s0921-5093(97)00710-7.

[27] C. S. Goh, J. Wei, L. C. Lee, and M. Gupta, "Ductility improvement and fatigue studies in Mg-CNT nanocomposites," *Compos. Sci. Technol.*, vol. 68, no. 6, pp. 1432–1439, 2008, doi: 10.1016/j.compscitech.2007.10.057.

[28] G. Cao, J. Kobliska, H. Konishi, and X. Li, "Tensile properties and microstructure of SiC nanoparticle-reinforced Mg-4Zn alloy fabricated by ultrasonic cavitation-based solidification processing," *Metall. Mater. Trans. A Phys. Metall. Mater. Sci.*, vol. 39 A, no. 4, pp. 880–886, 2008, doi: 10.1007/s11661-007-9453-6.

[29] E. T. Turkdogan, *Fundamentals of Steelmaking*. Institute of Materials, 1996.

[30] M. Zuo, M. Sokoluk, C. Cao, J. Yuan, S. Zheng, and X. Li, "Microstructure Control and Performance Evolution of Aluminum Alloy 7075 by Nano-Treating," *Sci. Rep.*, vol. 9, no. 1, pp. 1–11, 2019, doi: 10.1038/s41598-019-47182-9.

[31] M. Sokoluk, C. Cao, S. Pan, and X. Li, "Nanoparticle-enabled phase control for arc welding of unweldable aluminum alloy 7075," *Nat. Commun.*, vol. 10, no. 1, pp. 1–8, 2019, doi:

10.1038/s41467-018-07989-y.

[32] J. Yuan, M. Zuo, M. Sokoluk, G. Yao, S. Pan, and X. Li, “Nanotreating High-Zinc Al–Zn–Mg–Cu Alloy by TiC Nanoparticles,” in *Minerals, Metals and Materials Series*, Springer International Publishing, 2020, pp. 318–323.

[33] T. E. Quested, “Understanding mechanisms of grain refinement of aluminium alloys by inoculation,” *Mater. Sci. Technol.*, vol. 20, no. 11, pp. 1357–1369, 2004.

[34] G. Cao, H. Konishi, and X. Li, “Mechanical properties and microstructure of SiC-reinforced Mg-(2,4)Al-1Si nanocomposites fabricated by ultrasonic cavitation based solidification processing,” *Mater. Sci. Eng. A*, vol. 486, no. 1–2, pp. 357–362, 2008, doi: 10.1016/j.msea.2007.09.054.

[35] M. Habibnejad-Korayem, R. Mahmudi, and W. J. Poole, “Enhanced properties of Mg-based nano-composites reinforced with Al2O3 nano-particles,” *Mater. Sci. Eng. A*, vol. 519, no. 1–2, pp. 198–203, 2009, doi: 10.1016/j.msea.2009.05.001.

[36] A. Olguín, M. Ortíz, C. H. Wörner, O. Herrera, B. K. Kad, and P. M. Hazzledine, “Zener pins and needles,” *Philos. Mag. B*, vol. 81, no. 8, pp. 731–744, 2001.

[37] C. Cao *et al.*, “Bulk ultrafine grained/nanocrystalline metals via slow cooling,” *Sci. Adv.*, vol. 5, no. 8, 2019, doi: 10.1126/sciadv.aaw2398.

[38] A. Chauhan *et al.*, “Microstructure characterization and strengthening mechanisms of oxide dispersion strengthened (ODS) Fe-9%Cr and Fe-14%Cr extruded bars,” *J. Nucl. Mater.*, vol. 495, pp. 6–19, 2017, doi: 10.1016/j.jnucmat.2017.07.060.

[39] B. Reppich, “On the attractive particle–dislocation interaction in dispersion-strengthened material,” *Acta Mater.*, vol. 46, no. 1, pp. 61–67, 1998.

[40] L. Raman, K. Gothandapani, and B. S. Murty, “Austenitic oxide dispersion strengthened steels: A review,” *Def. Sci. J.*, vol. 66, no. 4, pp. 316–322, 2016, doi: 10.14429/dsj.66.10205.

[41] G. R. Odette, “Recent Progress in Developing and Qualifying Nanostructured Ferritic Alloys for Advanced Fission and Fusion Applications,” *Jom*, vol. 66, no. 12, pp. 2427–2441, 2014, doi: 10.1007/s11837-014-1207-5.

[42] J. Brodrick, D. J. Hepburn, and G. J. Ackland, “Mechanism for radiation damage resistance in yttrium oxide dispersion strengthened steels,” *J. Nucl. Mater.*, vol. 445, no. 1–3, pp. 291–297, 2014, doi: 10.1016/j.jnucmat.2013.10.045.

[43] Y. Min, M. Akbulut, K. Kristiansen, Y. Golan, and J. Israelachvili, “The role of interparticle and external forces in nanoparticle assembly,” *Nanosci. Technol. A Collect. Rev. from Nat. Journals*, pp. 38–49, 2009, doi: 10.1142/9789814287005_0005.

[44] J. S. Benjamin, “Dispersion strengthened superalloys by mechanical alloying,” *Metall. Trans.*, vol. 1, no. 10, pp. 2943–2951, 1970, doi: 10.1007/BF03037835.

[45] Z. Y. Ma *et al.*, “In-situ Al4C3 dispersoid and SiC particle mixture-reinforced aluminum composite,” *Scr. Metall. Mater.*, vol. 31, no. 2, pp. 131-*135, 1994.

[46] S. C. Tjong and Z. Y. Ma, “Microstructural and mechanical characteristics of in situ metal matrix composites,” *Mater. Sci. Eng.*, vol. 29, pp. 49–113, 2000.

[47] C. J. Hsu, C. Y. Chang, P. W. Kao, N. J. Ho, and C. P. Chang, “Al-Al3Ti nanocomposites produced in situ by friction stir processing,” *Acta Mater.*, vol. 54, no. 19, pp. 5241–5249, 2006, doi: 10.1016/j.actamat.2006.06.054.

[48] S. Lakshmi, L. Lu, and M. Gupta, “In situ preparation of TiB2 reinforced Al based composites,” *J. Mater. Process. Technol.*, vol. 73, no. 1–3, pp. 160–166, 1998, doi: 10.1016/S0924-0136(97)00225-2.

[49] M. Chen *et al.*, “Novel composite powders with uniform TiB2 nano-particle distribution for 3D printing,” *Appl. Sci.*, vol. 7, no. 3, pp. 3–12, 2017, doi: 10.3390/app7030250.

[50] X. P. Li *et al.*, “Selective laser melting of nano-TiB2decorated AlSi10Mg alloy with high fracture strength and ductility,” *Acta Mater.*, vol. 129, no. February, pp. 183–193, 2017, doi: 10.1016/j.actamat.2017.02.062.

[51] S. Pan, G. Yao, J. Yuan, M. Sokoluk, and X. Li, “Manufacturing of bulk Al-12Zn-3.7Mg-1Cu alloy with TiC nanoparticles,” *Procedia Manuf.*, vol. 48, pp. 325–331, 2020, doi: 10.1016/j.promfg.2020.05.054.

[52] F. Tang, M. Hagiwara, and J. M. Schoenung, “Microstructure and tensile properties of bulk

nanostructured Al-5083/SiCp composites prepared by cryomilling," *Mater. Sci. Eng. A*, vol. 407, no. 1–2, pp. 306–314, 2005.

[53] S. C. Tjong, "Novel nanoparticle-reinforced metal matrix composites with enhanced mechanical properties," *Adv. Eng. Mater.*, vol. 9, no. 8, pp. 639–652, 2007, doi: 10.1002/adem.200700106.

[54] W. Liu, C. Cao, J. Xu, X. Wang, and X. Li, "Molten salt assisted solidification nanoprocessing of Al-TiC nanocomposites," *Mater. Lett.*, 2016, doi: 10.1016/j.matlet.2016.09.023.

[55] Y. Kimura, S. Takaki, S. Suejima, R. Uemori, and H. Tamehiro, "Ultra Grain Refining and Decomposition of Oxide during Super-heavy Deformation in Oxide Dispersion Ferritic Stainless Steel Powder," *ISIJ Int.*, vol. 39, no. 1–2, pp. 176–182, 1999, doi: 10.2355/isijinternational.39.176.

[56] S. Ohtsuka *et al.*, "Effect of nano-size oxide particle dispersion and &-ferrite proportion on creep strength of 9Cr-ODS steel," *Mater. Trans.*, vol. 50, no. 7, pp. 1778–1784, 2009, doi: 10.2320/matertrans.M2009096.

[57] M. Ghayoor *et al.*, "Strengthening of 304l stainless steel by addition of yttrium oxide and grain refinement during selective laser melting," *Solid Free. Fabr. 2019 Proc. 30th Annu. Int. Solid Free. Fabr. Symp.*, pp. 967–976, 2019.

[58] M. Ghayoor, K. Lee, Y. He, C. Chang, B. K. Paul, and S. Pasebani, "Microstructural Analysis of Additively Manufactured 304L Stainless Steel Oxide Dispersion Strengthened Alloy," *Microsc. Microanal.*, vol. 25, no. S2, pp. 2594–2595, 2019, doi: 10.1017/s1431927619013709.

[59] B. AlMangour, D. Grzesiak, T. Borkar, and J. M. Yang, "Densification behavior, microstructural evolution, and mechanical properties of TiC/316L stainless steel nanocomposites fabricated by selective laser melting," *Mater. Des.*, vol. 138, pp. 119–128, 2018, doi: 10.1016/j.matdes.2017.10.039.

[60] B. Almangour, D. Grzesiak, and J. M. Yang, "Rapid fabrication of bulk-form TiB2/316L stainless steel nanocomposites with novel reinforcement architecture and improved

performance by selective laser melting," *J. Alloys Compd.*, vol. 680, pp. 480–493, 2016, doi: 10.1016/j.jallcom.2016.04.156.

[61] S. Qin, B. Liao, L. Mao, and F. Xiao, "A novel method for preparing nano-NbC/Fe powder and nano-NbC particle reinforced cast low-carbon steel," *Mater. Lett.*, vol. 121, pp. 162–165, 2014, doi: 10.1016/j.matlet.2014.01.168.

[62] K. Tanaka and T. Saito, "Phase equilibria in TiB2-reinforced high modulus steel," *J. Phase Equilibria*, vol. 20, no. 3, pp. 207–214, 1999, doi: 10.1361/105497199770335730.

[63] M. A. Moghadasi, M. Nili-Ahmadabadi, F. Forghani, and H. S. Kim, "Development of an oxide-dispersion-strengthened steel by introducing oxygen carrier compound into the melt aided by a general thermodynamic model," *Sci. Rep.*, vol. 6, no. August, pp. 1–10, 2016, doi: 10.1038/srep38621.

[64] J. G. Li, L. Coudurier, and N. EustathoPouLos, "Work of adhesion and contact-angle isotherm of binary alloys on ionocovalent oxides," *J. Mater. Sci.*, vol. 24, no. 3, pp. 1109–1116, 1989, doi: 10.1007/BF01148806.

[65] F. Goodwin, S. Guruswamy, K. U. Kainer, C. Kammer, and Wolfram Knabl, "Part 3.1 Metals," in *Springer Handbook of Condensed Matter and Materials Data*, W. Martienssen and H. Warlimont, Eds. Springer, 2005, pp. 161–300.

[66] M. Salvo, V. Casalegno, M. Suess, L. Gozzelino, and C. Wilhelmi, "Laser surface nanostructuring for reliable Si3N4/Si3N4 and Si3N4/Invar joined components," *Ceram. Int.*, vol. 44, no. 11, pp. 12081–12087, 2018, doi: 10.1016/j.ceramint.2018.03.226.

[67] T. Morikawa, T. Moronaga, and K. Higashida, "Fine-grained structures associated with deformation twin and its influence on tensile behaviours in a cold-rolled Fe-Ni alloy," *Mater. Sci. Forum*, vol. 503–504, pp. 895–900, 2006, doi: 10.4028/www.scientific.net/msf.503-504.895.

[68] R. R. Mulyukov, V. A. Kazantsev, K. Y. Mulyukov, A. M. Burkhanov, I. M. Safarov, and I. K. Bitkulov, "Properties of Fe-36%Ni invar with nanocrystalline structure," *Rev. Adv. Mater. Sci.*, vol. 11, no. 2, pp. 116–121, 2006.

[69] C. Chen, B. Ma, S. Miao, and B. Liu, "Effect of Cobalt on Microstructure and Mechanical

Properties of Invar Alloy," in *Advances in Materials Processing*, Y. Han, Ed. Springer Singapore, 2018, pp. 803–810.

[70] K. Nakama, K. Sugita, and Y. Shirai, "Effect of MC Type Carbides on Age Hardness and Thermal Expansion of Fe-36 wt%Ni-0.2 wt%C Alloy," *Metallogr. Microstruct. Anal.*, vol. 2, no. 6, pp. 383–387, 2013, doi: 10.1007/s13632-013-0101-9.

[71] A. Vinogradov, S. Hashimoto, and V. I. Kopylov, "Enhanced strength and fatigue life of ultra-fine grain Fe-36Ni Invar alloy," *Mater. Sci. Eng. A*, vol. 355, no. 1–2, pp. 277–285, 2003, doi: 10.1016/S0921-5093(03)00082-0.

[72] K. Sridharan, F. J. Worzala, and R. A. Dodd, "Heat treatment and microstructure of an FeNiCo Invar alloy strengthened by intermetallic precipitation," *Mater. Charact.*, vol. 29, no. 4, pp. 321–327, 1992, doi: 10.1016/1044-5803(92)90103-O.

[73] Y. Liu, L. Liu, Z. Wu, J. Li, B. Shen, and W. Hu, "Grain growth and grain size effects on the thermal expansion properties of an electrodeposited Fe-Ni invar alloy," *Scr. Mater.*, vol. 63, no. 4, pp. 359–362, 2010, doi: 10.1016/j.scriptamat.2010.04.006.

[74] Y. Liu, L. Liu, B. Shen, and W. Hu, "A study of thermal stability in electrodeposited nanocrystalline Fe-Ni invar alloy," *Mater. Sci. Eng. A*, vol. 528, no. 18, pp. 5701–5705, 2011, doi: 10.1016/j.msea.2011.04.052.

[75] H. Liu *et al.*, "Effect of aging on microstructures and properties of Mo-alloyed Fe-36Ni invar alloy," *Mater. Sci. Eng. A*, vol. 654, pp. 107–112, 2016, doi: 10.1016/j.msea.2015.12.018.

[76] S. Yahagi, K. Kusaka, and T. Kato, "Effect of Ni and Ti on the thermal expansion of Fe–Ni–Co–Ti alloys," *Denki-Seiko*, vol. 51, no. 2, pp. 80–89, 1980.

[77] M. Laurent-Brocq *et al.*, "Influence of ball-milling and annealing conditions on nanocluster characteristics in oxide dispersion strengthened steels," *Acta Mater.*, vol. 60, no. 20, pp. 7150–7159, 2012, doi: 10.1016/j.actamat.2012.09.024.

[78] C. M. Fernandes and A. M. R. Senos, "Cemented carbide phase diagrams: A review," *Int. J. Refract. Met. Hard Mater.*, vol. 29, no. 4, pp. 405–418, 2011, doi: 10.1016/j.ijrmhm.2011.02.004.

[79] R. R. Reeber and K. Wang, “Thermophysical Properties of ⎵ -Tungsten Carbide,” vol. 35, 1999.

[80] S. H. Kim, H. Kim, and N. J. Kim, “Brittle intermetallic compound makes ultrastrong low-density steel with large ductility,” *Nature*, vol. 518, no. 7537, pp. 77–79, 2015, doi: 10.1038/nature14144.

[81] S. Jiang *et al.*, “Ultrastrong steel via minimal lattice misfit and high-density nanoprecipitation,” *Nature*, vol. 544, no. 7651, pp. 460–464, 2017, doi: 10.1038/nature22032.

[82] B. B. He *et al.*, “High dislocation density-induced large ductility in deformed and partitioned steels,” *Science (80-.).*, vol. 357, no. 6355, pp. 1029–1032, 2017, doi: 10.1126/science.aan0177.

[83] T. C. Lin *et al.*, “Aluminum with dispersed nanoparticles by laser additive manufacturing,” *Nat. Commun.*, vol. 10, no. 1, pp. 1–9, 2019, doi: 10.1038/s41467-019-12047-2.

[84] A. Devaraj *et al.*, “A low-cost hierarchical nanostructured beta-titanium alloy with high strength,” *Nat. Commun.*, vol. 7, pp. 1–8, 2016, doi: 10.1038/ncomms11176.

[85] S. Tang *et al.*, “Precipitation strengthening in an ultralight magnesium alloy,” *Nat. Commun.*, vol. 10, no. 1, 2019, doi: 10.1038/s41467-019-08954-z.

[86] S. Chen, R. Rana, A. Haldar, and R. K. Ray, “Current state of Fe-Mn-Al-C low density steels,” *Prog. Mater. Sci.*, vol. 89, pp. 345–391, 2017, doi: 10.1016/j.pmatsci.2017.05.002.

[87] S. Munstermann, Y. Feng, and W. Bleck, “Influencing parameters on elastic modulus of steels,” *Can. Metall. Q.*, vol. 53, no. 3, pp. 264–273, 2014.

[88] A. Antoni-Zdziobek, M. Gospodinova, F. Bonnet, and F. Hodaj, “Solidification paths in the iron-rich part of the Fe-Ti-B ternary system,” *J. Alloys Compd.*, vol. 657, pp. 302–312, 2016, doi: 10.1016/j.jallcom.2015.10.104.

[89] H. Warlimont, “Part 3.2 Ceramics,” in *Springer Handbook of Condensed Matter and Materials Data*, W. Martienssen and H. Warlimont, Eds. Springer, 2005, pp. 451–458.

[90] M. S. Y. Feng, “Strengthening of steels by ceramic phase,” RWTH Aachen University,

2013.

[91] M. Kulka, N. Makuch, and A. Piasecki, “Nanomechanical characterization and fracture toughness of FeB and Fe2B iron borides produced by gas boriding of Armco iron,” *Surf. Coatings Technol.*, vol. 325, pp. 515–532, 2017.

[92] C. Baron, H. Springer, and D. Raabe, “Efficient liquid metallurgy synthesis of Fe-TiB2 high modulus steels via in-situ reduction of titanium oxides,” *Mater. Des.*, vol. 97, no. February, pp. 357–363, 2016, doi: 10.1016/j.matdes.2016.02.076.

[93] Z. C. Luo, B. B. He, Y. Z. Li, and M. X. Huang, “Growth Mechanism of Primary and Eutectic TiB2 Particles in a Hypereutectic Steel Matrix Composite,” *Metall. Mater. Trans. A Phys. Metall. Mater. Sci.*, vol. 48, no. 4, pp. 1981–1989, 2017, doi: 10.1007/s11661-017-4001-5.

[94] H. Springer, R. Aparicio Fernandez, M. J. Duarte, A. Kostka, and D. Raabe, “Microstructure refinement for high modulus in-situ metal matrix composite steels via controlled solidification of the system Fe-TiB2,” *Acta Mater.*, vol. 96, pp. 47–56, 2015, doi: 10.1016/j.actamat.2015.06.017.

[95] A. Javadi, S. Pan, C. Cao, G. Yao, and X. Li, “Facile synthesis of 10 nm surface clean TiB2 nanoparticles,” *Mater. Lett.*, vol. 229, pp. 107–110, 2018, doi: 10.1016/j.matlet.2018.06.054.

[96] K. Bao, Y. Wen, M. Khangkhamano, and S. Zhang, “Low-temperature preparation of titanium diboride fine powder via magnesiothermic reduction in molten salt,” *J. Am. Ceram. Soc.*, vol. 100, no. 5, pp. 2266–2272, 2017, doi: 10.1111/jace.14649.

[97] L. Ottavi, C. Saint-Jours, N. Valignant, and C. H. Allibert, “Phase equilibria and solidification of Fe-Ti-B alloys in the region close to Fe-TiB2,” *Zeitschrift für Met.*, vol. 83, no. 2, pp. 80–83, 1992.

[98] O. K. von Goldbeck, “Iron—Boron Fe—B,” in *IRON—Binary Phase Diagrams*, Springer, Berlin, Heidelberg, 1982, pp. 15–18.

[99] H. Okamoto and T. B. Massalski, “Correct and Incorrect Phase Diagram Features,” in *Methods for Phase Diagram Determination*, J. C. Zhao, Ed. Elsevier Science, 2007.

[100] M. De Cicco *et al.*, “Strong, ductile magnesium-zinc nanocomposites,” *Metall. Mater. Trans. A Phys. Metall. Mater. Sci.*, vol. 40, no. 12, pp. 3038–3045, 2009, doi: 10.1007/s11661-009-0013-0.

[101] P. Tolias, “Non-retarded room temperature Hamaker constants between elemental metals,” *Surf. Sci.*, vol. 700, no. May, p. 121652, 2020, doi: 10.1016/j.susc.2020.121652.

[102] L. Bergström, A. Meurk, H. Arwin, and D. J. Rowcliffe, “Estimation of Hamaker constants of ceramic materials from optical data using Lifshitz theory,” *Journal of the American Ceramic Society*, vol. 79, no. 2. pp. 339–348, 1996, doi: 10.1111/j.1151-2916.1996.tb08126.x.

[103] J. Q. Xu, L. Y. Chen, H. Choi, and X. C. Li, “Theoretical study and pathways for nanoparticle capture during solidification of metal melt,” *J. Phys. Condens. Matter*, vol. 24, no. 25, 2012, doi: 10.1088/0953-8984/24/25/255304.

[104] L. Holappa, “Iron and Steel Technology,” in *Treatise on Process Metallurgy Volume 3: Industrial Processes*, S. Seetharaman, Ed. Elsevier, 2014, pp. 2–88.

[105] F. Bonnet, V. Daeschler, and G. Petitgand, “High modulus steels: a new requirement of automotive market. How to take up the challenge?,” *Can. Metall. Q.*, vol. 53, no. 3, pp. 243–252, 2014.

[106] J. -G Li, “Wetting and Interfacial Bonding of Metals with Ionocovalent Oxides,” *J. Am. Ceram. Soc.*, vol. 75, no. 11, pp. 3118–3126, 1992, doi: 10.1111/j.1151-2916.1992.tb04396.x.

[107] K. Verhiest *et al.*, “Experimental study on the contact angle formation of solidified iron-chromium droplets onto yttria ceramic substrates for the yttria/ferrous alloy system with variable chromium content,” *Ceram. Int.*, vol. 40, no. 1 PART B, pp. 2187–2200, 2014, doi: 10.1016/j.ceramint.2013.07.137.

[108] S. Yu, Y. Liu, and Z. He, “Effect of Nb on the interfacial wettability in Al2O3/medium Mn steel,” *Journal of Materials Science and Technology*, vol. 19, no. 6. pp. 625–627, 2003.

[109] A. K. Niessen, F. R. de Boer, R. Boom, P. F. de Châtel, W. C. M. Mattens, and A. R. Miedema, “Model predictions for the enthalpy of formation of transition metal alloys II,”

Calphad, vol. 7, no. 1, pp. 51–70, 1983, doi: 10.1016/0364-5916(83)90030-5.

[110] V. A. Parsegian, "Tables of formulae in spherical geometry," in *Van der waals forces*, Cambridge University Press, 2006, pp. 149–169.

[111] K. C. Mills and Y. C. Su, "Review of surface tension data for metallic elements and alloys: Part 1 - Pure metals," *Int. Mater. Rev.*, vol. 51, no. 6, pp. 329–351, 2006, doi: 10.1179/174328006X102510.

[112] H. T. Li, L. F. Chen, X. Yuan, W. Q. Zhang, J. R. Smith, and A. G. Evans, "Interfacial stoichiometry and adhesion at metal/α-Al 2O3 interfaces," *J. Am. Ceram. Soc.*, vol. 94, no. SUPPL. 1, pp. s154–s159, 2011, doi: 10.1111/j.1551-2916.2011.04405.x.

[113] W. Zhang and J. Smith, "Stoichiometry and adhesion of Nb/Al2O3," *Phys. Rev. B - Condens. Matter Mater. Phys.*, vol. 61, no. 24, pp. 16883–16889, 2000, doi: 10.1103/PhysRevB.61.16883.

[114] T. Cheng, D. Fang, and Y. Yang, "The temperature-dependent surface energy of ceramic single crystals," *Journal of the American Ceramic Society*, vol. 100, no. 4. pp. 1598–1605, 2017, doi: 10.1111/jace.14689.

[115] H. Zhang *et al.*, "Stable colloids in molten inorganic salts," *Nature*, vol. 542, no. 7641, pp. 328–331, 2017, doi: 10.1038/nature21041.

[116] J. Xu, L. Chen, H. Choi, H. Konish, and X. Li, "Assembly of metals and nanoparticles into novel nanocomposite superstructures," *Sci. Rep.*, vol. 3, pp. 1–5, 2013, doi: 10.1038/srep01730.

[117] G. R. Odette, M. J. Alinger, and B. D. Wirth, "Recent developments in irradiation-resistant steels," *Annu. Rev. Mater. Res.*, vol. 38, pp. 471–503, 2008, doi: 10.1146/annurev.matsci.38.060407.130315.

[118] T. K. Kim *et al.*, "Current Status and Future Prospective of Advanced Radiation Resistant Oxide Dispersion Strengthened Steel (ARROS) Development for Nuclear Reactor System Applications," *Nucl. Eng. Technol.*, vol. 48, no. 2, pp. 572–594, 2016, doi: 10.1016/j.net.2015.12.005.

[119] R. Kozakov, H. Schöpp, G. Gött, A. Sperl, G. Wilhelm, and D. Uhrlandt, “Weld pool temperatures of steel S235 while applying a controlled short-circuit gas metal arc welding process and various shielding gases,” *J. Phys. D. Appl. Phys.*, vol. 46, no. 47, 2013, doi: 10.1088/0022-3727/46/47/475501.

[120] P. A. Hooper, “Melt pool temperature and cooling rates in laser powder bed fusion,” *Addit. Manuf.*, vol. 22, no. May, pp. 548–559, 2018, doi: 10.1016/j.addma.2018.05.032.

[121] G. Grant, J. Darsell, and D. Catalini, “Low Cost Fabrication of ODS Alloys,” Pittsburgh, PA, 2013.